AFRL-AFOSR-UK-TR-2024-0009

Thin films with 2D behavior and linear galvanomagnetic response

Speliotis, Athanassios
NATIONAL CENTER FOR SCIENTIFIC RESEARCH 'DEMOKRITOS'
Patr. Grigoriou E' & 1 Neapoleos
Paraskevi, , 15310
GR

12/12/2023
Final Technical Report

Air Force Research Laboratory
Air Force Office of Scientific Research
European Office of Aerospace Research and Development
Unit 4515 Box 14, APO AE 09421

REPORT DOCUMENTATION PAGE

PLEASE DO NOT RETURN YOUR FORM TO THE ABOVE ORGANIZATION.

1. REPORT DATE	2. REPORT TYPE	3. DATES COVERED	
20231212	Final	START DATE 20170515	END DATE 20210514

4. TITLE AND SUBTITLE
Thin films with 2D behavior and linear galvanomagnetic response

5a. CONTRACT NUMBER	5b. GRANT NUMBER	5c. PROGRAM ELEMENT NUMBER
	FA9550-17-1-0178	
5d. PROJECT NUMBER	**5e. TASK NUMBER**	**5f. WORK UNIT NUMBER**

6. AUTHOR(S)
Athanassios Speliotis

7. PERFORMING ORGANIZATION NAME(S) AND ADDRESS(ES)
NATIONAL CENTER FOR SCIENTIFIC RESEARCH 'DEMOKRITOS'
Patr. Grigoriou E' & 1 Neapoleos
Paraskevi 15310
GR

8. PERFORMING ORGANIZATION REPORT NUMBER

9. SPONSORING/MONITORING AGENCY NAME(S) AND ADDRESS(ES)	10. SPONSOR/MONITOR'S ACRONYM(S)	11. SPONSOR/MONITOR'S REPORT NUMBER(S)
EOARD UNIT 4515 APO AE 09421-4515	AFRL/AFOSR IOE	AFRL-AFOSR-UK-TR-2024-0009

12. DISTRIBUTION/AVAILABILITY STATEMENT
A Distribution Unlimited: PB Public Release

13. SUPPLEMENTARY NOTES

14. ABSTRACT
The grant yielded six publication and eleven conference presenations studying bismuth thin films which are potential material systems for topological insulators, a new class of materials which may enable novel electronic and quantum devices.

ABSTRACT:
This was a very successful project that culminated in important discoveries, supported one Ph.D. student, four Master's Students and resulted in six publications. The main focus of the study was the magnetotransport behavior of magnetron sputtered thin films of Bi semimetal systems and topological insulators such as Bi2Te3. More specifically, Bi thin films were deposited at temperatures ranging from room temperature to 300 oC. The magnetotransport properties were mainly studied for sample deposited at 80 oC. The formation of equilibrium crystals at depositions at 271 oC (melting point of Bi) was also of outmost interest and the crystals were examined in terms of their shape and size. The study of Bi2Te3 topological insulator thin films was based on the breaking of time-reversal symmetry. For this reason the systems examined were either doped with magnetic moments (Co, Cr, Mn, V, Sm) or interfaced with magnetic layers such as Co to induce magnetic proximity effects. Another system that was considered interesting to study was the interfaced topological insulator Bi2Te3 with superconducting Nb for the examination of topological superconductivity.

15. SUBJECT TERMS

16. SECURITY CLASSIFICATION OF:			17. LIMITATION OF ABSTRACT	18. NUMBER OF PAGES
a. REPORT U	b. ABSTRACT U	c. THIS PAGE U	SAR	78

19a. NAME OF RESPONSIBLE PERSON	19b. PHONE NUMBER *(Include area code)*
SCOTT DUDLEY	314 235 6031

Standard Form 298 (Rev.5/2020)
Prescribed by ANSI Std. Z39.18

Report Type
Final Report
Primary Contact Email
Contact email if there is a problem with the report.
t.speliotis@inn.demokritos.gr
Primary Contact Phone Number
Contact phone number if there is a problem with the report
+302106503383 - +306947040711
Organization / Institution name
NCSR Demokritos
Grant/Contract Title
The full title of the funded effort.
Thin Films With 2D Behavior and Linear Galvanomagnetic Response
Grant/Contract Number
AFOSR assigned control number.
FA9550-17-1-0178
Principal Investigator Name
The full name of the principal investigator on the grant or contract.
Athanassios Speliotis
Program Officer
The AFOSR/EOARD Program Officer currently assigned to the award
Dr. Jason Foley, AFOSR/IOE, (314) 235-6010, jason.foley.1@us.af.mil
Reporting Period Start Date
May 15, 2017
Reporting Period End Date
May 14, 2021

Abstract

This was a very successful project that culminated in important discoveries, supported one Ph.D. student, four Master Students and resulted in six publications. The main focus of the study was the magnetotransport behavior of magnetron sputtered thin films of Bi semimetal systems and topological insulators such as Bi_2Te_3. More specifically, Bi thin films were deposited at temperatures ranging from room temperature to 300 ^oC. The magnetotransport properties were mainly studied for sample deposited at 80 ^oC. The formation of equilibrium crystals at depositions at 271 ^oC (melting point of Bi) was also of outmost interest and the crystals were examined in terms of their shape and size. The study of Bi_2Te_3 topological insulator thin films was based on the breaking of time reversal symmetry. For this reasons the systems examined were either doped with magnetic moments (Co, Cr, Mn, V, Sm) or interfaced with magnetic layers such as Co to induce magnetic proximity effects. Another system that was considered interesting to study was the interfaced topological insulator Bi_2Te_3 with superconducting Nb for the examination of topological superconductivity. In addition to these the systems $Bi_{1-x}Sb_x$ and $Bi_{1-x}Mn_x$ were also studied although in preliminary level. Finally, along with these systems, the behavior of magnetic materials (Co and Sm-Co) deposited on kapton substrates was also examined and lead to valuable results for possible applications in spintronics. The approach of these studies offers an avenue of miniaturizing electro-optical components, reducing power consumption and lowering cost in multiple defense applications.

Publications acknowledged this grant

1. A. Pilidi and Th. Speliotis, "Anomalous Hall Effect in a Magnetic Topological Insulator $(BiMn)_2Te_3$", *IEEE Transactions on Magnetics*, **55**, 2400506 (2019)
2. A. Pilidi, Th. Speliotis and G. Litsardakis, "Structural and magnetotransport characterization of magnetron sputtered Co-doped Bi_2Te_3 thin films", *Journal of Magnetism and Magnetic Materials*, **511**, 166971 (2020)
3. A. Pilidi, A. Tzanis, T. Helm, M. Arfanis, P. Falaras, Th. Speliotis, "Nanometer-thick bismuth nanocrystal films for sensoric applications", *ACS Applied Nano Materials*, **3**(10), 9669-9678 (2020)
4. A. Tzanis, M. Zeibekis, A. Pilidi, N. Koutsokostas, C. Kollia and Th. Speliotis, "Villari magnetomechanical coupling at hcp-Cobalt thin films on flexible substrates", *Materials Science and Engineering: B*, **264**, 114945 (2021)
5. A. Pilidi, T. Speliotis and G. Litsardakis, "Magnetotransport Phenomena in Topological Insulator / Superconductor Bi_2Te_3/Nb Bilayer and Trilayer Thin Films," *2021 IEEE International Magnetic Conference (INTERMAG)*, 2100038 (2021)
6. A. Tzanis, N. Koutsokostas, T. Helm, C. Kollia and Th. Speliotis, "Micrometer Thick Sm-Co Films for Applications on Flexible Systems", *Materials Science and Engineering B*, **280**, 115691 (2022)

Conferences

1. "Structural and Magnetotransport Properties of Bismuth and Bismuth/Cobalt Thin Films" A. Pilidi,C. Christides and Th. Speliotis, **62nd Annual Conference on Magnetism and Magnetic Materials**, *Pittsburgh, Pennsylvania, United States, November 6-10, 2017* (Poster Presentation)
2. Anomalous Hall effect in a magntetically doped (BiMn)2Te3topological insulator", A. Pilidi and Th. Speliotis, **Future perspectives on novel magnetic materials**, *Santorini, Greece, May 29 –June 3, 2018* (Poster Presentation)
3. "Magneto-transport properties of Bismuth thin films grown on kapton", N. koutsokostas, A. Pilidi, C. Collia and Th. Speliotis, **9th Joint European Magnetic Symposia (JEMS)**, *Mainz, Germany, September 3-7, 2018*
4. "Magnetotransport properties of Bi-Sb thin films", A. Pilidi, G. Kopnov, A. Gerber and Th. Speliotis, **9th Joint European Magnetic Symposia (JEMS)**, *Mainz, Germany, September 3-7, 2018* (Poster Presentation)
5. "Structural and magnetotransport characterization of Bi2Te3–Co bilayer magnetron sputtered thin films", A. Pilidi, Th. Speliotis and G. Litsardakis, **9th Joint European Magnetic Symposia (JEMS)**, *Mainz, Germany, September 3-7, 2018* (Poster Presentation)
6. "Anomalous Hall Effect in a Magnetic Topological Insulator (BiMn)2Te3", A. Pilidi and Th. Speliotis, **Joint MMM –Intermag Conference**, *Washington DC, United States, January 14-18, 2019* (Poster Presentation)
7. "Magnetotransport Properties of Mn-doped Bismuth Thin Films", A. Pilidi, Th. Speliotis and C. Christides, **10th Joint European Magnetic Symposia (JEMS)**, *Uppsala, Sweden, August 25-30, 2019* (Poster Presentation)
8. "Structural and Magnetotransport Characterization of Sm-Doped Bi2Te3Thin Films", A. Pilidi and Th. Speliotis, **10th Joint European Magnetic Symposia (JEMS)**, *Uppsala, Sweden, August 25-30, 2019* (Poster Presentation)
9. "Structural and Magnetotransport Characterization of Co-Doped Bi2Te3Thin Films", A. Pilidi, Th. Speliotis and G. Litsardakis, **10th Joint European Magnetic Symposia (JEMS)**, *Uppsala, Sweden, August 25-30, 2019* (Poster Presentation)

10. "Bi_2Te_3 - Co topological insulators: Structural characterization and magnetotransport study of magnetron sputtered thin films" , A. Pilidi, Th. Speliotis and G. Litsardakis, **34th Panhellenic Conference on Solid State Physics and Materials Science,** *Patras, Greece, September 11-14, 2019* (Oral Presentation)
11. "Magnetotransport Characterization of Mn-doped Bi_2Te_3Thin Films", A. Pilidi, Th. Speliotis and T. Helm, **1st Magnetofon Summer School on Ultrafast Opto-magneto-electronics**, *Lisbon, Portugal, September 23-27, 2019* (Poster Presentation)

Patent disclosures

No

PhD's granted

Alexandra Pilidi (August 1, 2017 – December 31, 2020)

Awarded dissertations that were supported by the program

- Koutsokostas N. (2018) "Structural and magnetotransport characterization of Bi thin films" *National Technical University of Athens, School of Chemical Engineering* (Master)
- Tzanis A. (2020) "Development and characterization of magnetic thin films deposited on flexible substrates (flexomagnetism) with magnetron sputtering technique." *National Technical University of Athens, School of Chemical Engineering* (Master)
- Pilidi A. (2021) "Structural and Magneto-transport of topological thin films of $Bi_{1-x}Sb_x$", *National Technical University of Athens, School of Applied Mathematics and Physical Sciences.* (Master)
- Pilidi A. (2021) "Magneto-transport phenomena in thin films of topological insulators and semimetal systems", *National Technical University of Athens, School of Applied Mathematics and Physical Sciences.* (Phd)
- Plevri Zoe, (2021) "Composition, structural properties and magnetoresistance phenomena in thin films of $(Bi_{1-x}Sm_x)_2Te_3$", *National Technical University of Athens, School of Applied Mathematics and Physical Sciences.* (Master)

Presentation of Main Experimental Findings

Structural and Magnetotransport properties of Bismuth Thin Films & Examination of Equilibrium Crystals

The particular study is concerned with investigations of the structural, surface morphological, and magnetotransport properties of DC magnetron-sputtered nanometer-thick Bi nanocrystal films on Si(111) substrates. Crystal structure and surface morphology were studied with X-ray diffraction, Raman spectroscopy, field-emission scanning electron microscopy, and atomic force microscopy. For the samples deposited at the melting point of Bi, namely 271 ^{o}C, equilibrium crystals formed, that according to Wulff theorem acquire a specific shape determined by the surface tension. These crystals were investigated for different film thicknesses and deposition temperatures varying from room temperature to 300 ^{o}C. Furthermore, magnetotransport characterization was carried out in steady and pulsed magnetic fields of up to 9 T and 70 T, respectively. At low temperatures, clear weak-antilocalization behavior is observed, attributed to 2D conduction channels. A non-linear Hall resistance is observed attributed to the coexistence of two types of carriers (*p* and *n*). The study of Bi thin films aims to elucidate its transport properties so that it can be exploited in modern applications such as sensorics.

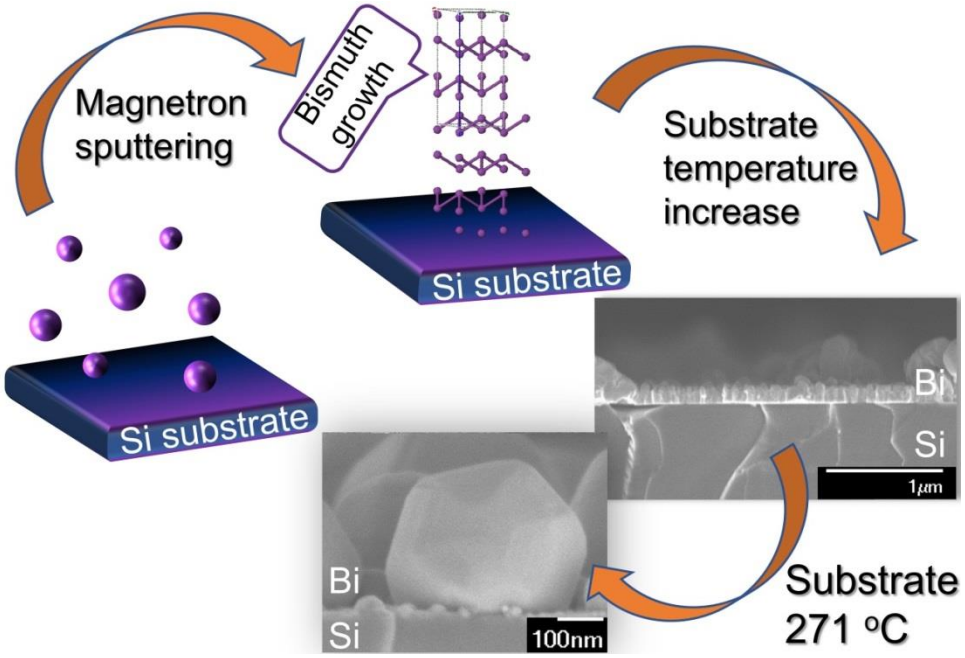

Figure 1. *The fabrication process of Bi nanoscale thin films that follows two different growth modes, namely Stranski-Krastanov and Volmer-Weber depending on the deposition temperature.*

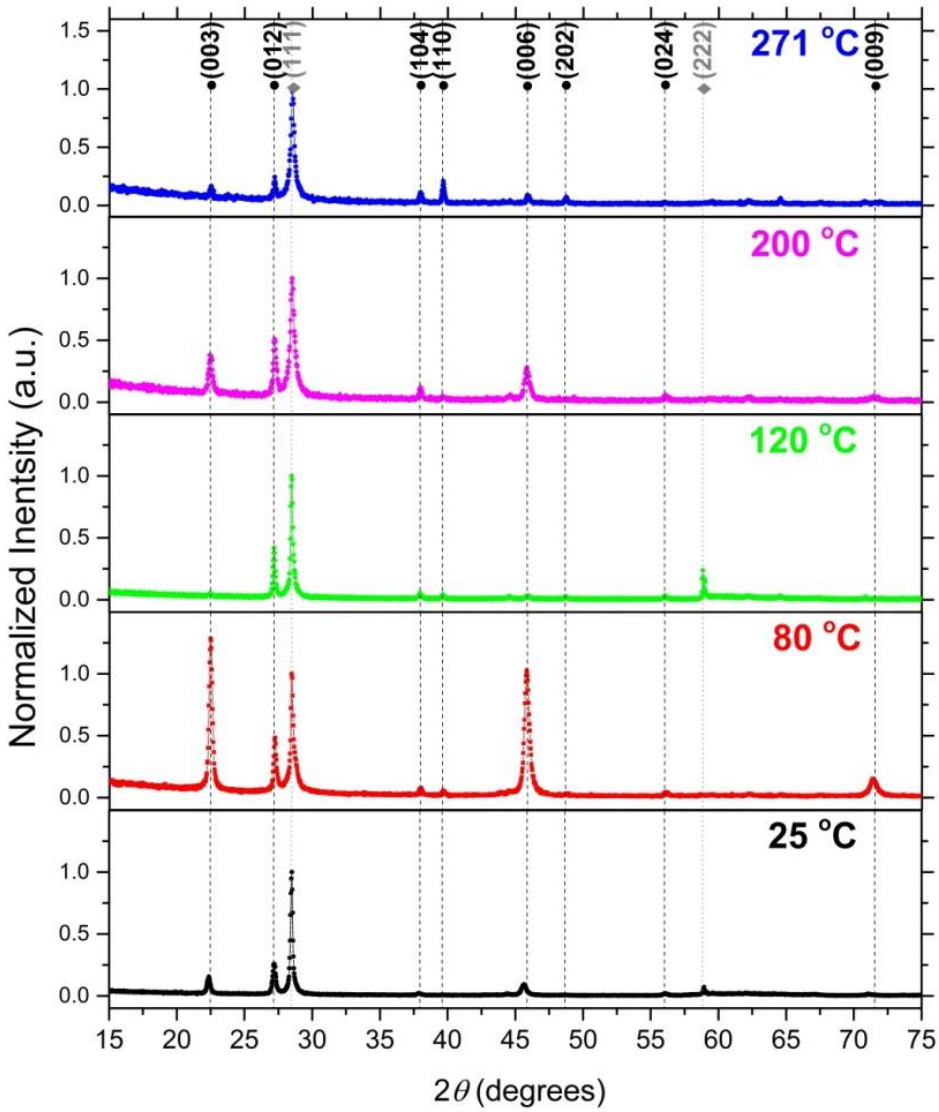

Figure 2. *X-ray diffraction: θ-2θ patterns for Bi films (50 nm) grown at different substrate temperatures. The peak positions for bulk Bi, from MATCH! reference entry, are marked by black dots and the ones for the Si(111) substrate by grey diamonds.*

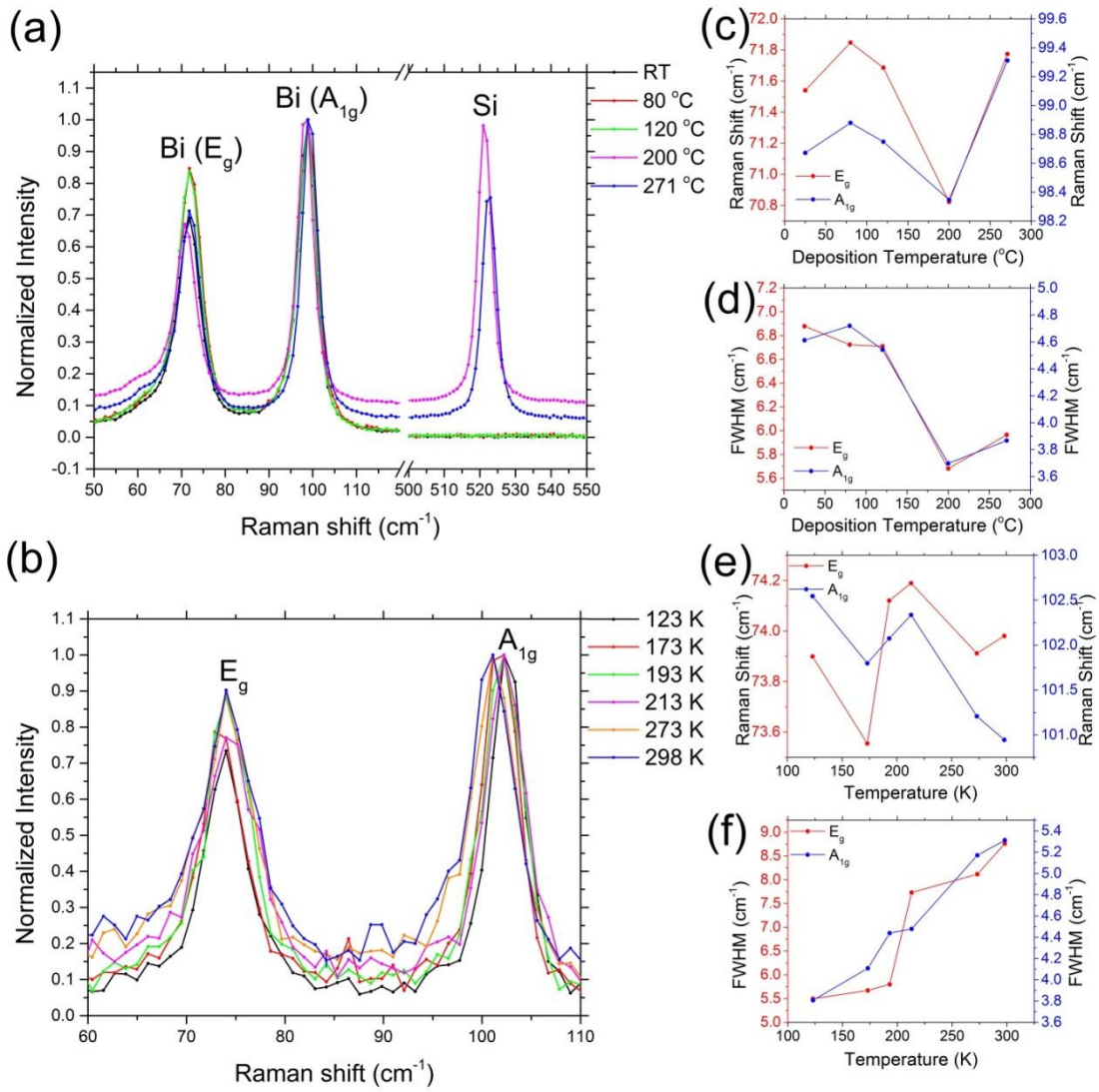

Figure 3. *(a) Raman spectra for Bi samples of 100 nm thickness deposited at different temperatures. (b) Raman spectra of 100 nm Bi sample deposited at 80 °C measured at different temperatures. (c) Peak positions for the samples deposited at different temperatures. (d) FWHM of E_g and A_{1g} peaks for the samples deposited at different temperatures. (e) Peak positions for the sample deposited at 80 °C and measured at lower temperatures. (f) FWHM of E_g and A_{1g} peaks for the sample deposited at 80 °C and measured at lower temperatures.*

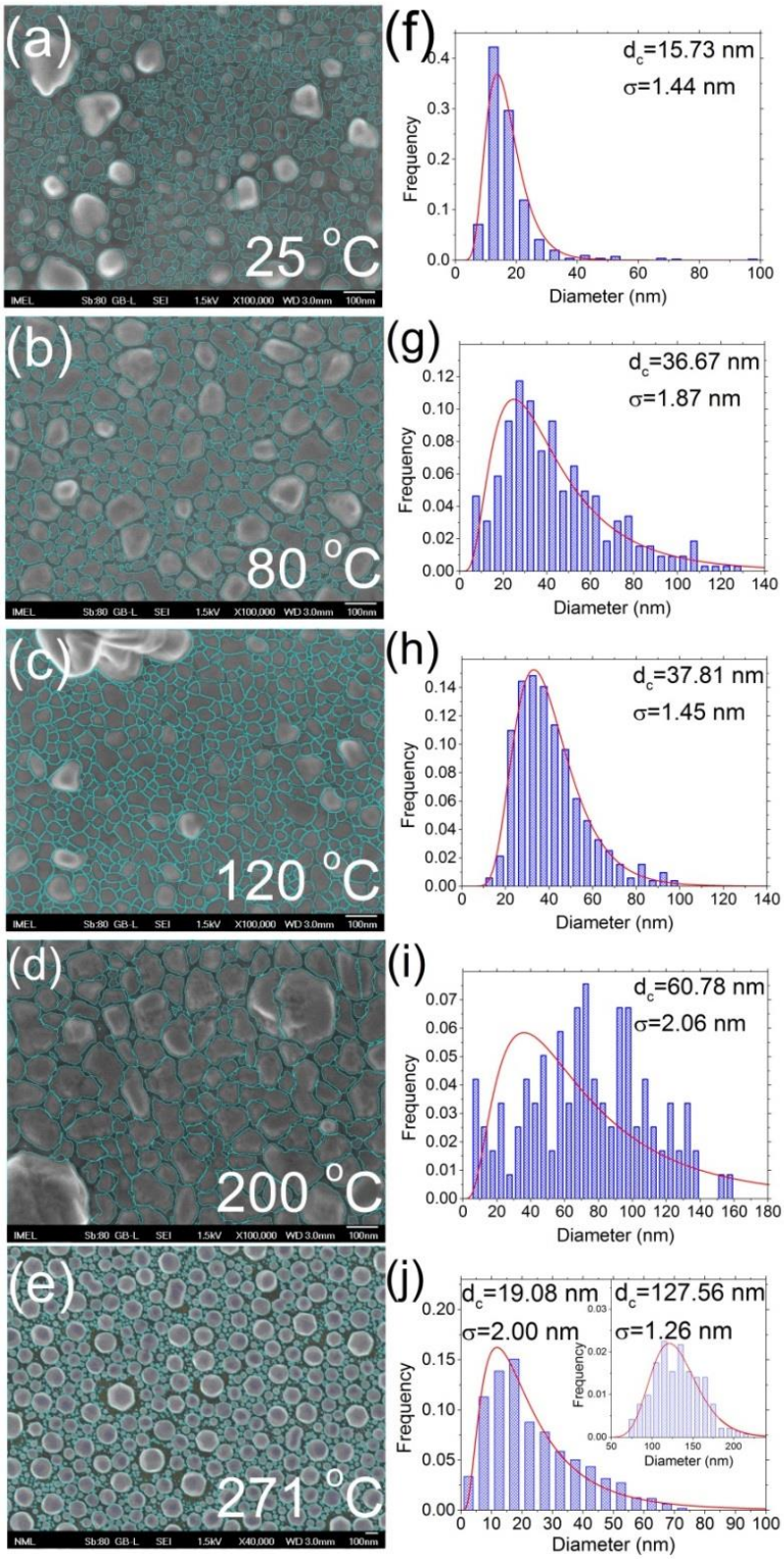

Figure 4. *FESEM images of 50 nm thick Bi samples deposited at different temperatures (a-e). The images were analyzed with ImageJ software and the grain diameter distribution is presented in (f-j).*

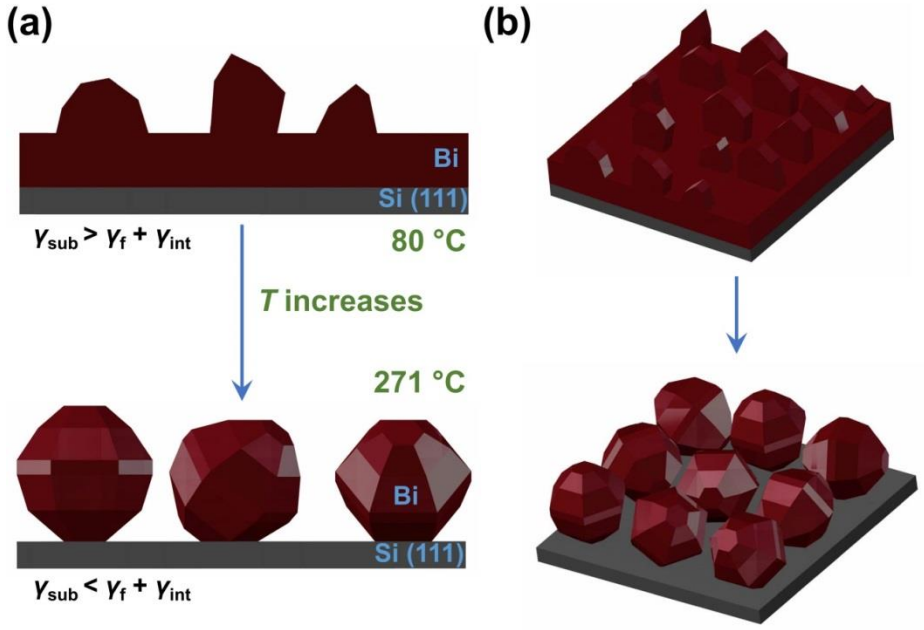

Figure 5. *Illustration of different growth modes found on Bi deposition. (a) 2D and (b) 3D representation of the transition from the Stranski-Krastanov to the Volmer-Weber growth mode as the temperature increases.*

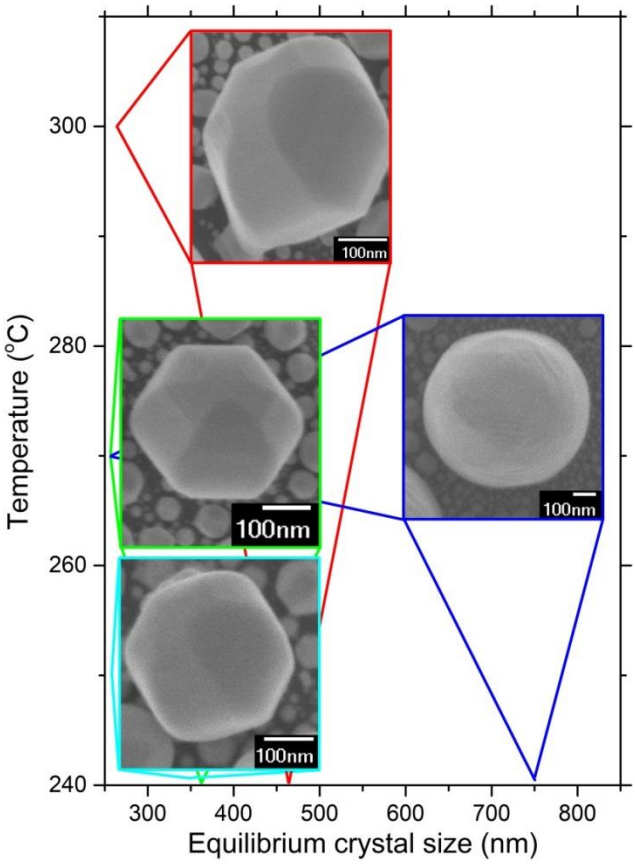

Figure 6. *Equilibrium-crystal growth and sizes depending on temperature.*

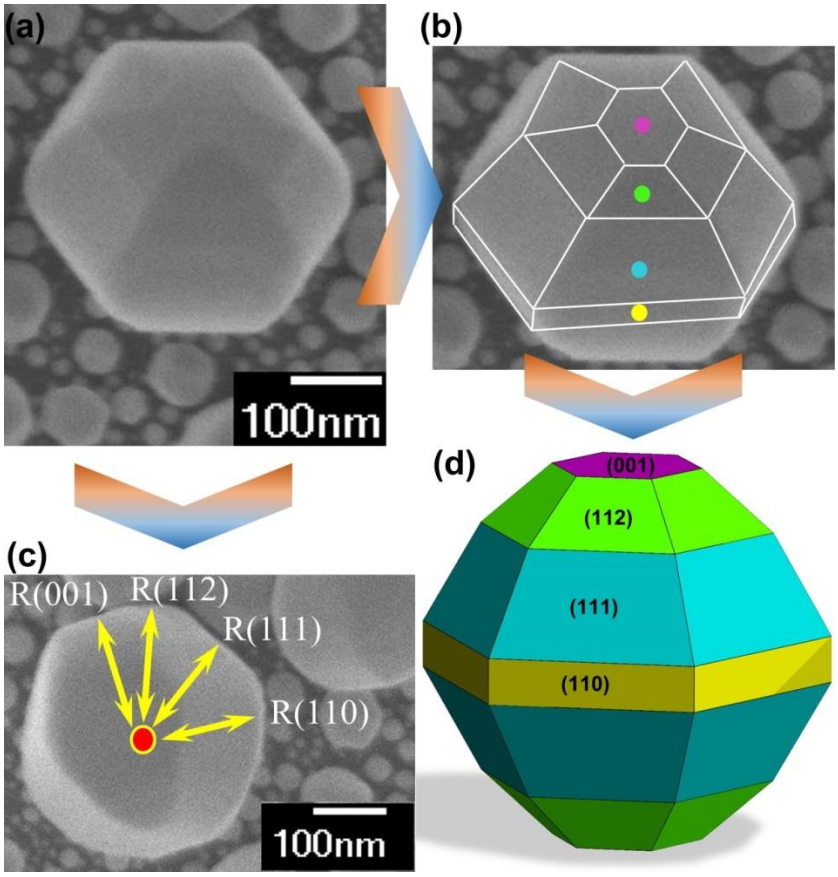

Figure 7. *(a) FESEM image of an equilibrated Bi crystal. (b) The same crystal with outlined edges and colored planes. (c) The distances of the facets from the Wulff center at an equilibrium crystal detected at a 90-degree rotation (side view). (d) The corresponding representation of the Wulff shape of the crystal in Wulffmaker.*

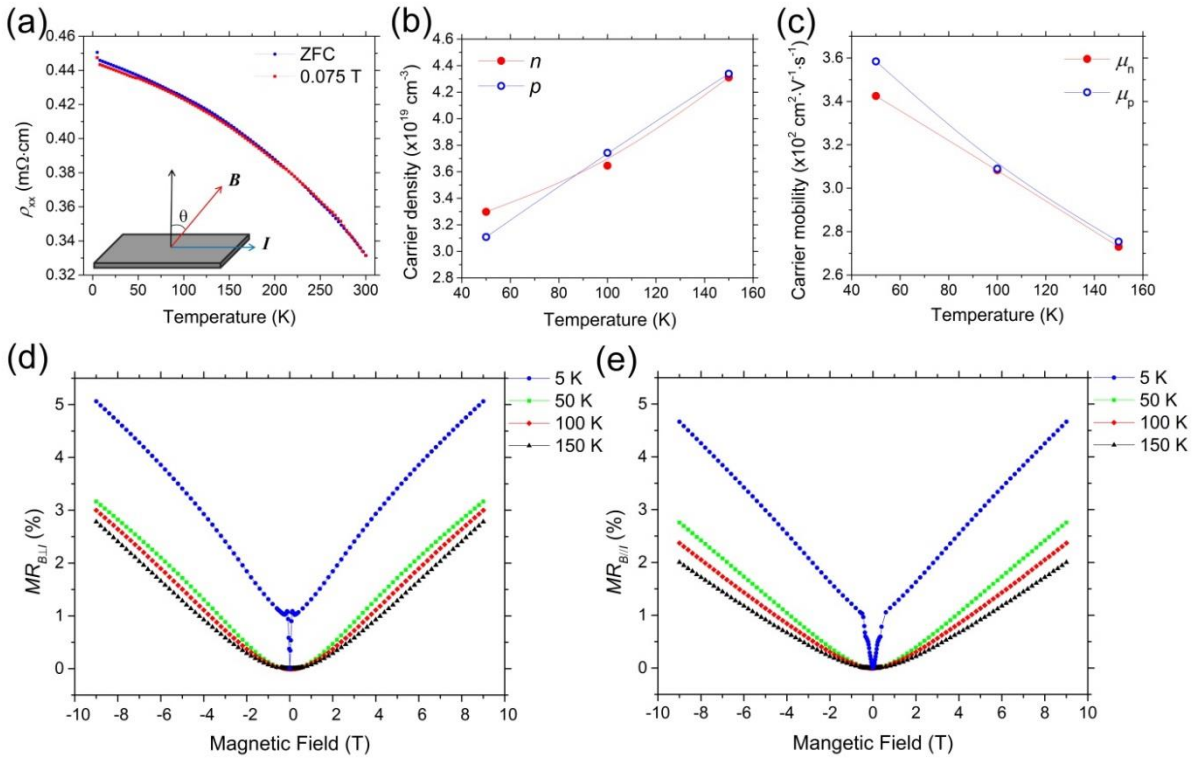

Figure 8. *(a) Temperature dependence of resistivity for ZFC and cooling with a magnetic field of 0.075 T. (b) Carrier density for electrons, n, and holes, p, versus temperature. (c) Carrier mobility of electrons, μ_n, and holes, μ_p, versus temperature. (d), (e) MR curves with magnetic field (d) perpendicular and (e) parallel to the film plane.*

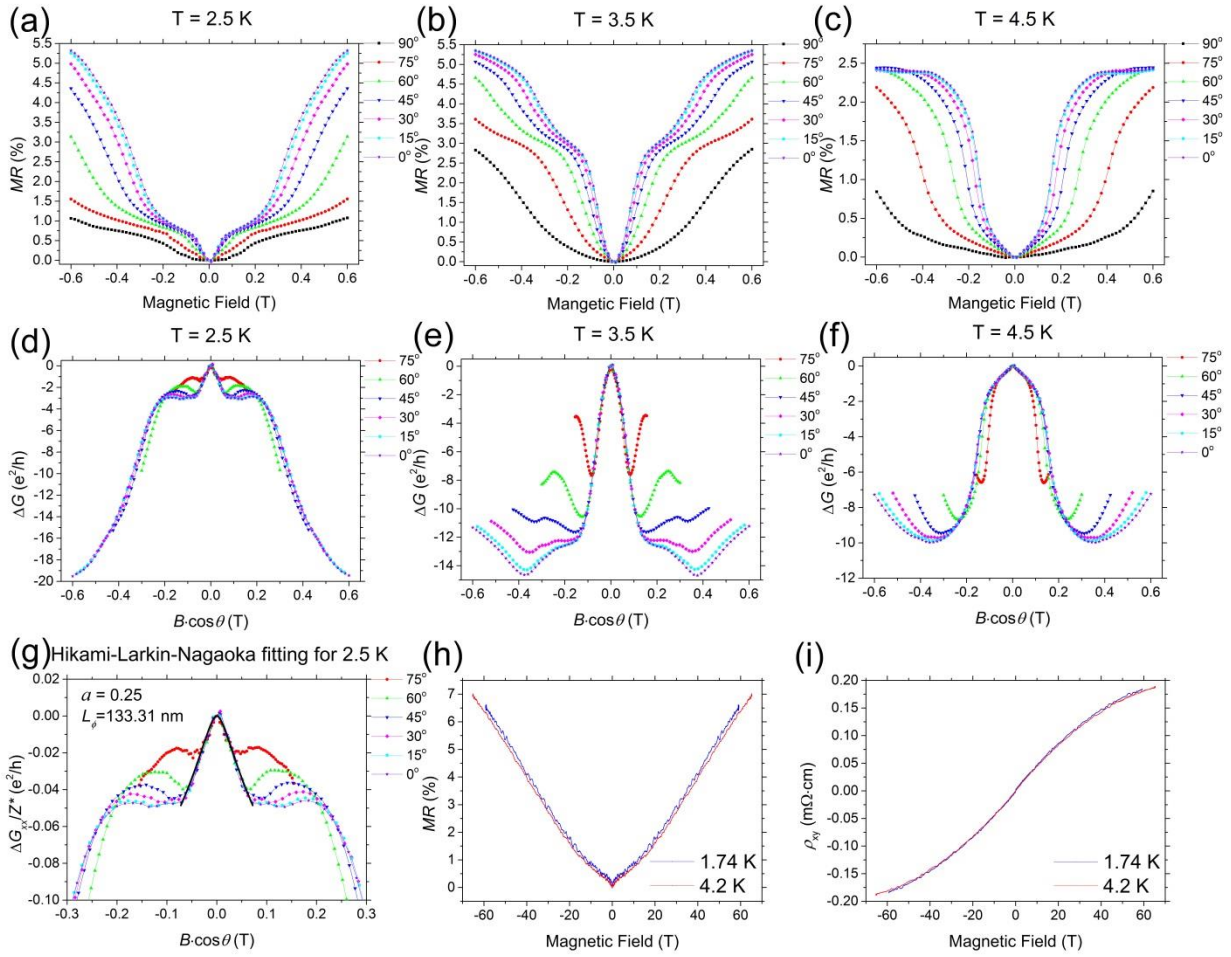

Figure 9. *(a) – (c) MR curves at different tilt angles for 2.5, 3.5, and 4.5 K, respectively. (d)-(f) Magnetoconductance curves for different tilt angles plotted versus B cosθ. (g) Fitting to the Hikami-Larkin-Nagaoka formula at 2.5 K. (h), (i) Magnetotransport measurements performed in pulsed high magnetic fields at low temperatures for a 100 nm thick Bi film (h) MR and (i) Hall resistivity.*

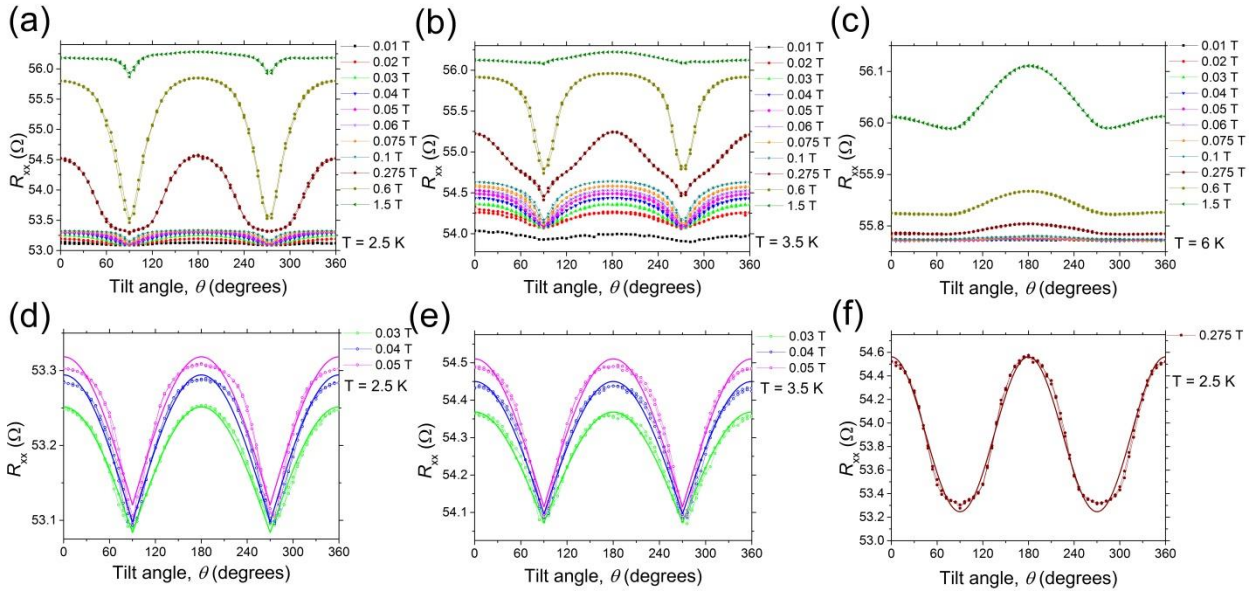

Figure 10. Angle-dependent MR with variation of tilt angle for (a) 2.5 K, (b) 3.5 K, and (c) 6 K with magnetic field up to 1.5 T. (d), (e) Fitting of $R_{xx}(\theta)$ to the functional form $|\cos\theta|$ for 2.5 K and 3.5 K, respectively, and for magnetic fields from 0.03 to 0.05 T. (f) Fitting of $R_{xx}(\theta)$ to the functional form $\cos 2\theta$ for 2.5 K and 0.275 T.

Structural and magnetotransport properties of Bi_2Te_3 – Co bilayers and related proximity effects

The aim of this study was to prepare and characterize bilayer structures of Bi_2Te_3 – Co, and the corresponding reference samples of Bi_2Te_3 and Co. The structural, morphological and magnetotransport properties are presented in the following diagrams. The magnetic proximity effect is manifested as a divergence of the magnetoresistance measurements from the values expected according to a two parallel resistors model, that does not involve any interaction in the interface of topological insulator and ferromagnet.

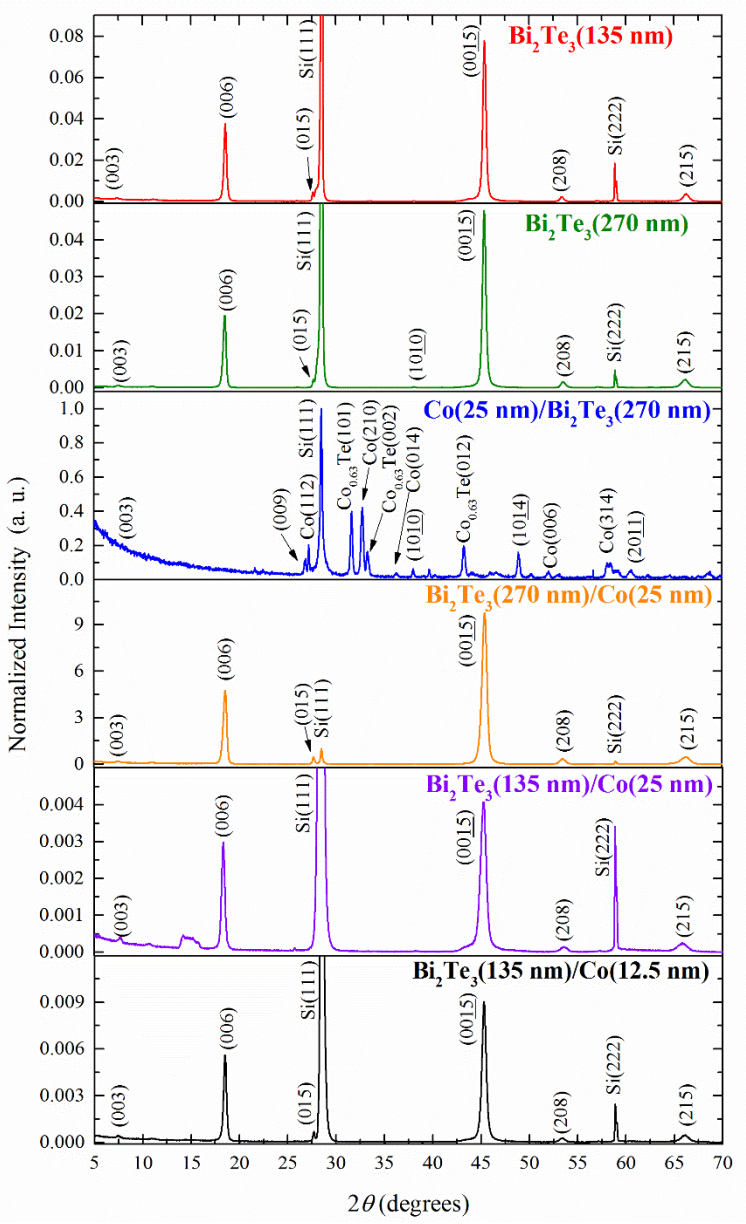

Figure 11. *XRD patterns for Bi_2Te_3–Co bilayers and Bi_2Te_3 reference samples deposited on Si(111) substrates.*

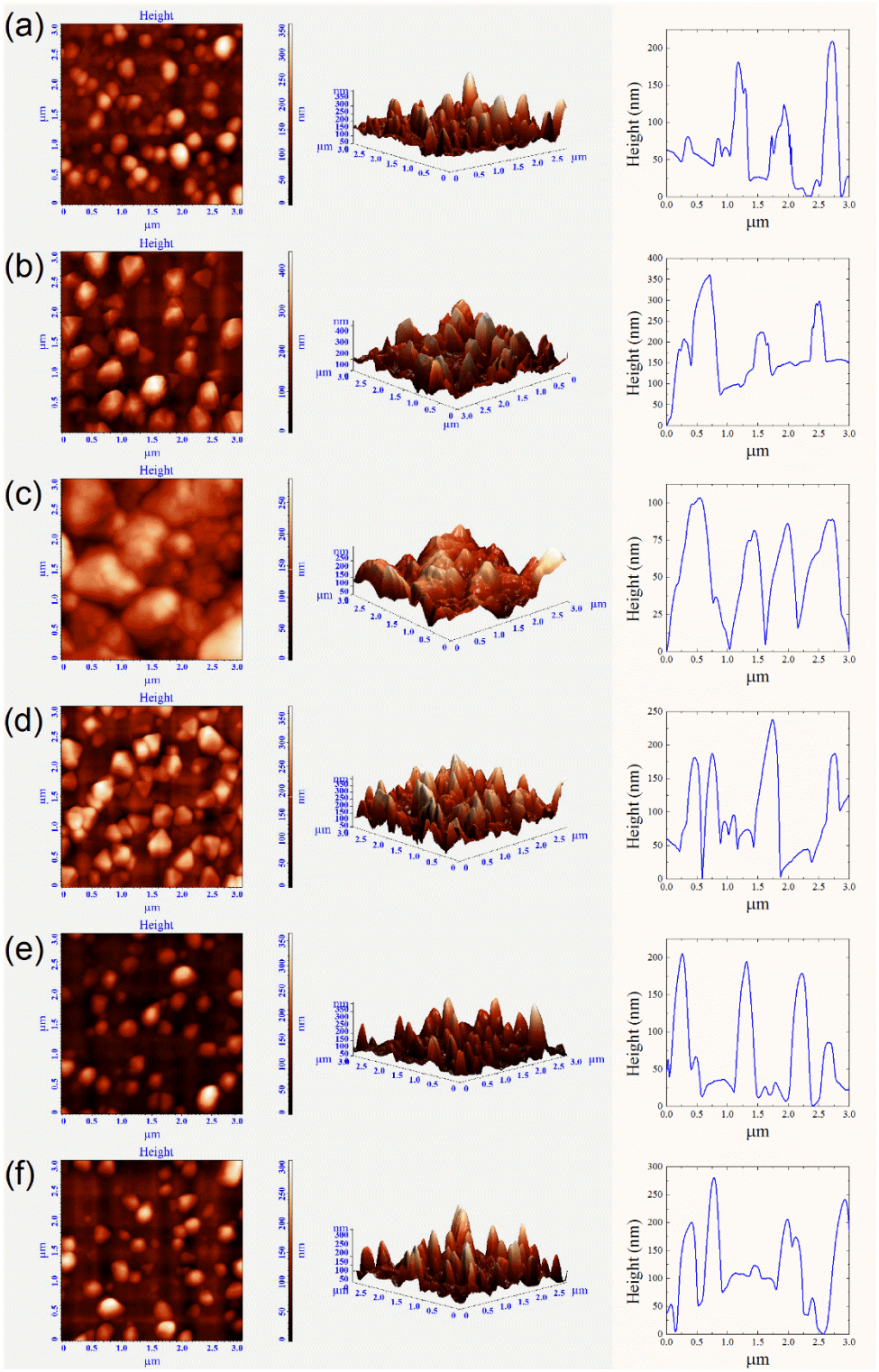

***Figure 12**. AFM scans of a 3x3 μm² surface for the thin films (a) Bi_2Te_3(135 nm), (b) Bi_2Te_3(270 nm), (c) Co(25 nm)/Bi_2Te_3(270 nm), (d) Bi_2Te_3(270 nm)/Co(25 nm), (e) Bi_2Te_3(135 nm)/Co(25 nm) and (f) Bi_2Te_3(135 nm)/Co(12.5 nm). For each scan the 3D representation and height profile of last scan are presented.*

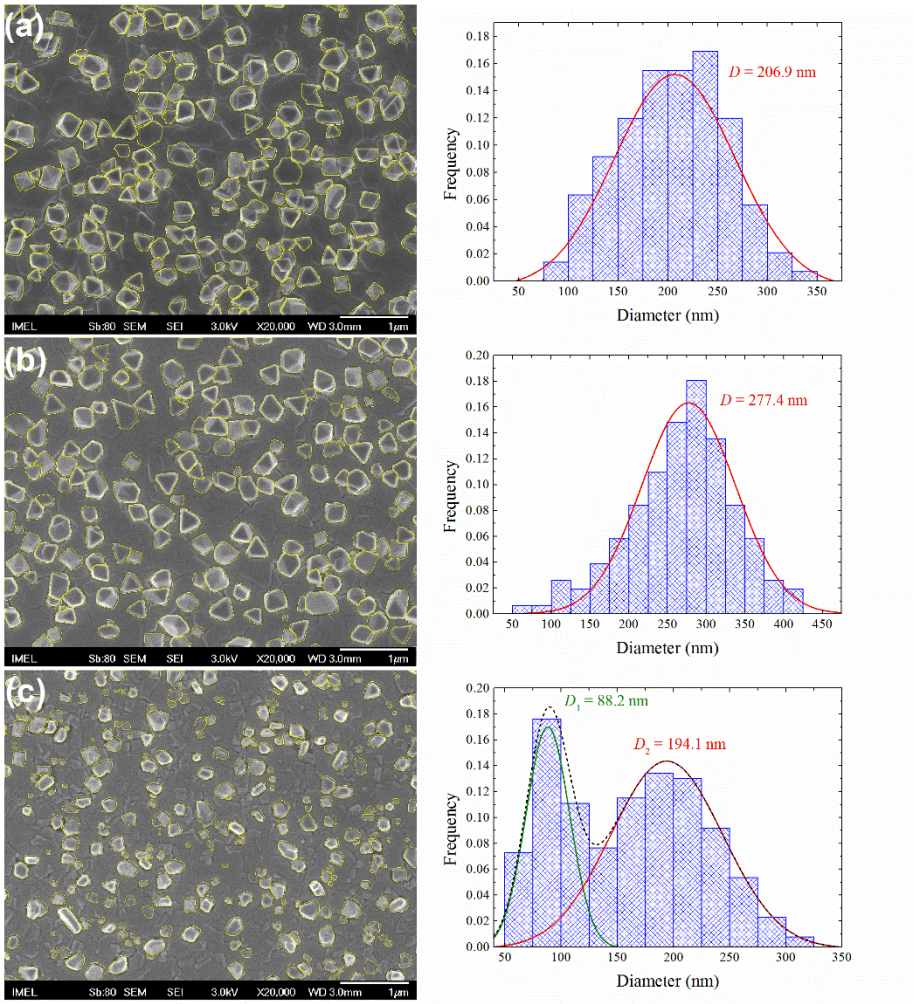

***Figure 13**. FESEM scans for the thin films (a) Bi_2Te_3(270 nm), (b) Bi_2Te_3(270 nm)/Co(25 nm) and (c) Bi_2Te_3(135 nm), each accompanied by the corresponding grain diameter distribution diagram.*

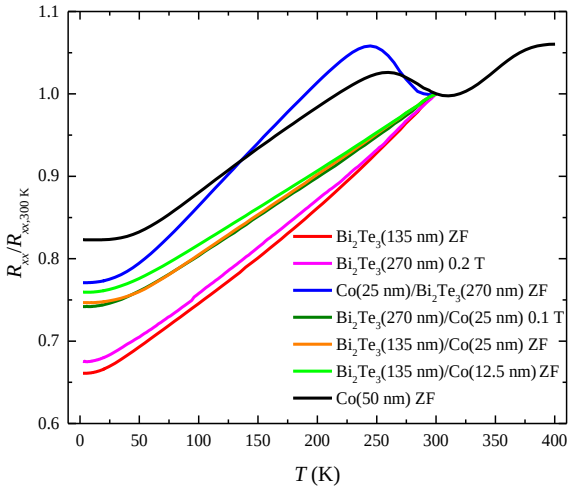

***Figure 14.** Variation of longitudinal resistance, R_{xx}, with temperature for the bilayer thin films Bi_2Te_3-Co and the reference samples of Bi_2Te_3 and Co.*

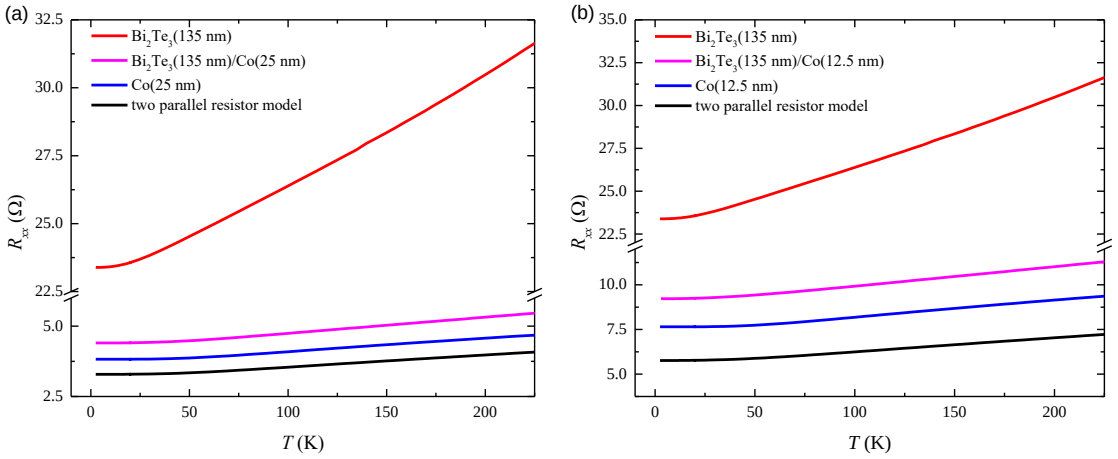

Figure 15. *Comparison of the zero field temperature variation of longitudinal resistance for the bilayer structures (a) Bi_2Te_3(135 nm) and Bi_2Te_3(135 nm)/Co(12.5 nm) in comparison to a two parallel resistor model.*

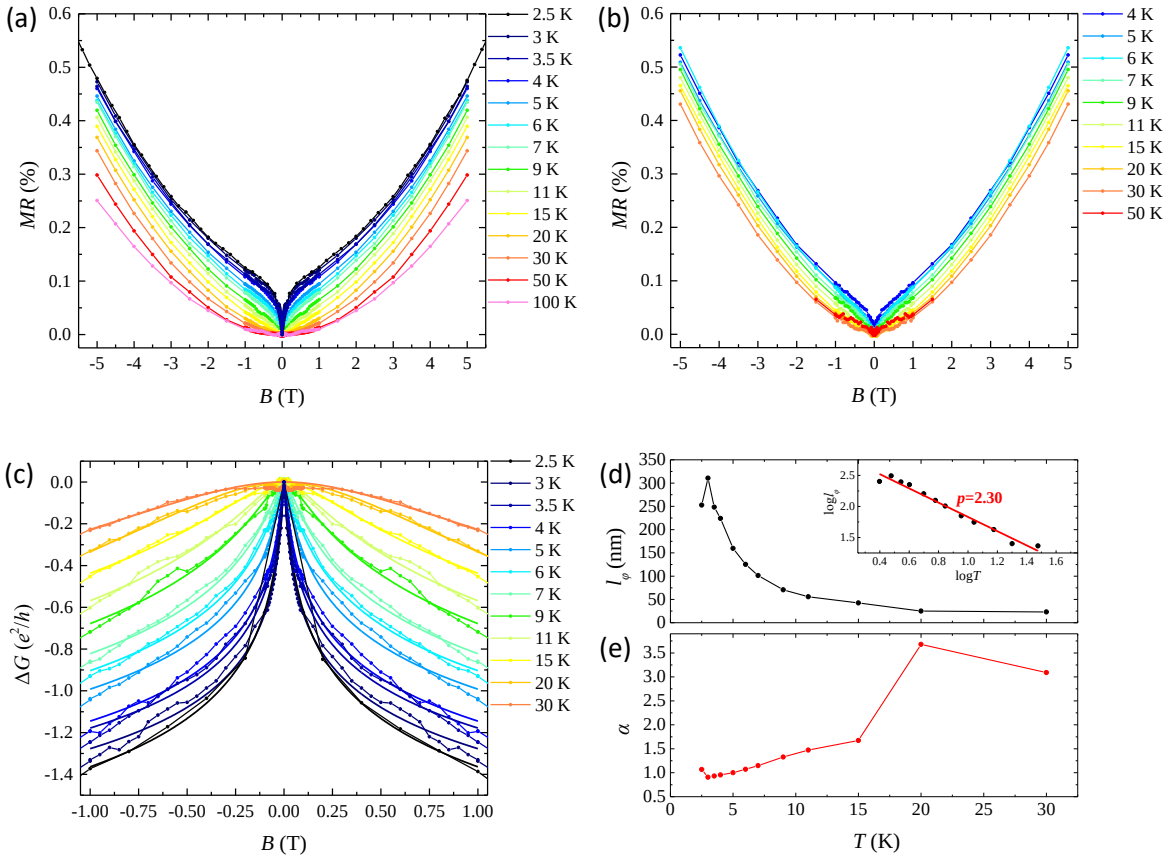

Figure 16. *(a) MR measurements for the reference sample Bi_2Te_3(135 nm), (b) MR measurements for the reference sample Bi_2Te_3(270 nm), (c) ΔG curves and fitting to HLN formula for the sample Bi_2Te_3(135 nm), (d) and (e) α and l_φ parameters extracted from the HLN fitting (c).*

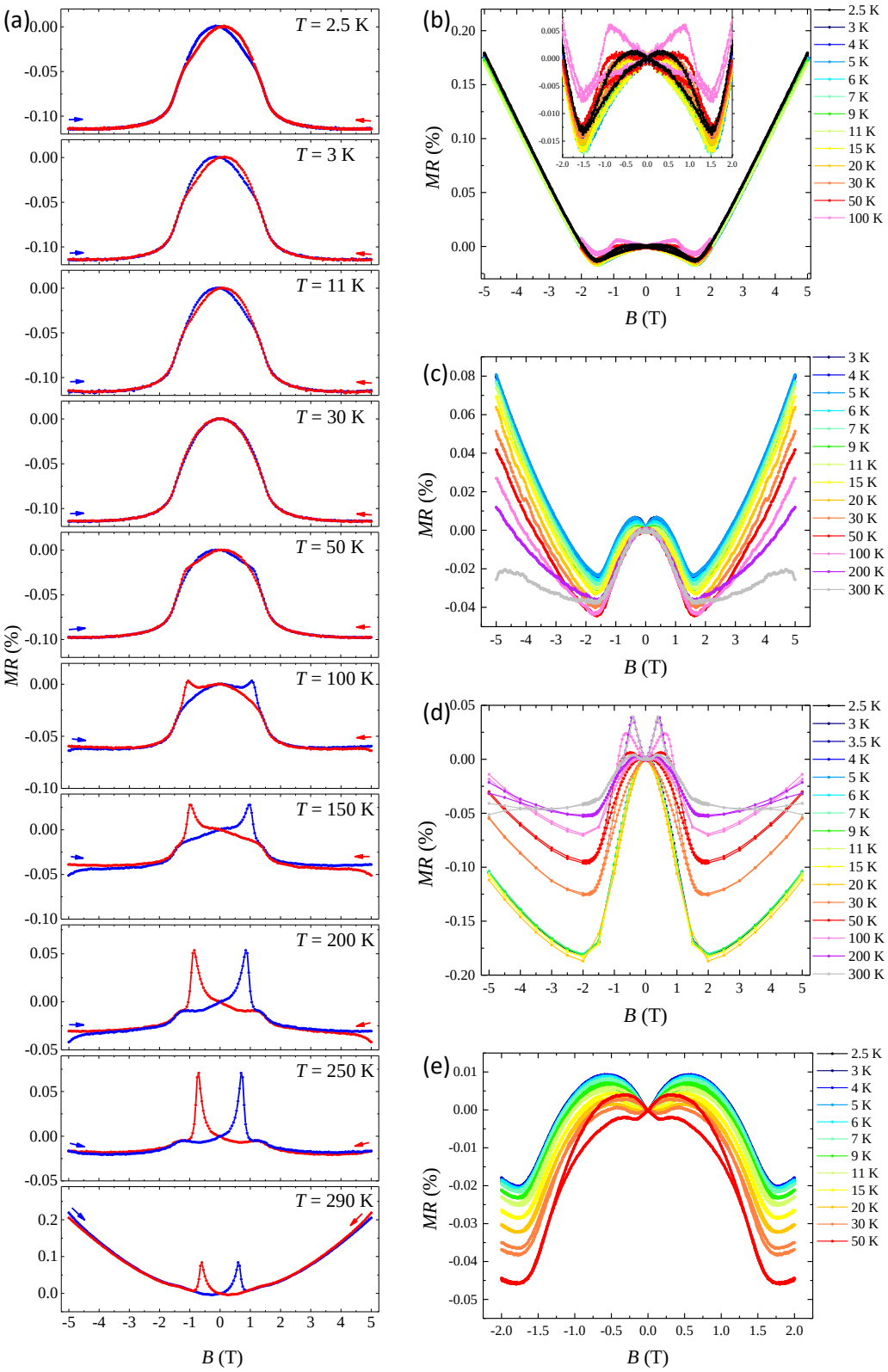

Figure 16. *MR curves for (a) the Co(50 nm) reference sample and the structures (b) Co(15 nm)/Bi_2Te_3(270 nm), (c) Bi_2Te_3(270 nm)/Co(25 nm), (d) Bi_2Te_3(135 nm)/Co(25 nm) and (e) Bi_2Te_3(135 nm)/Co(12.5 nm).*

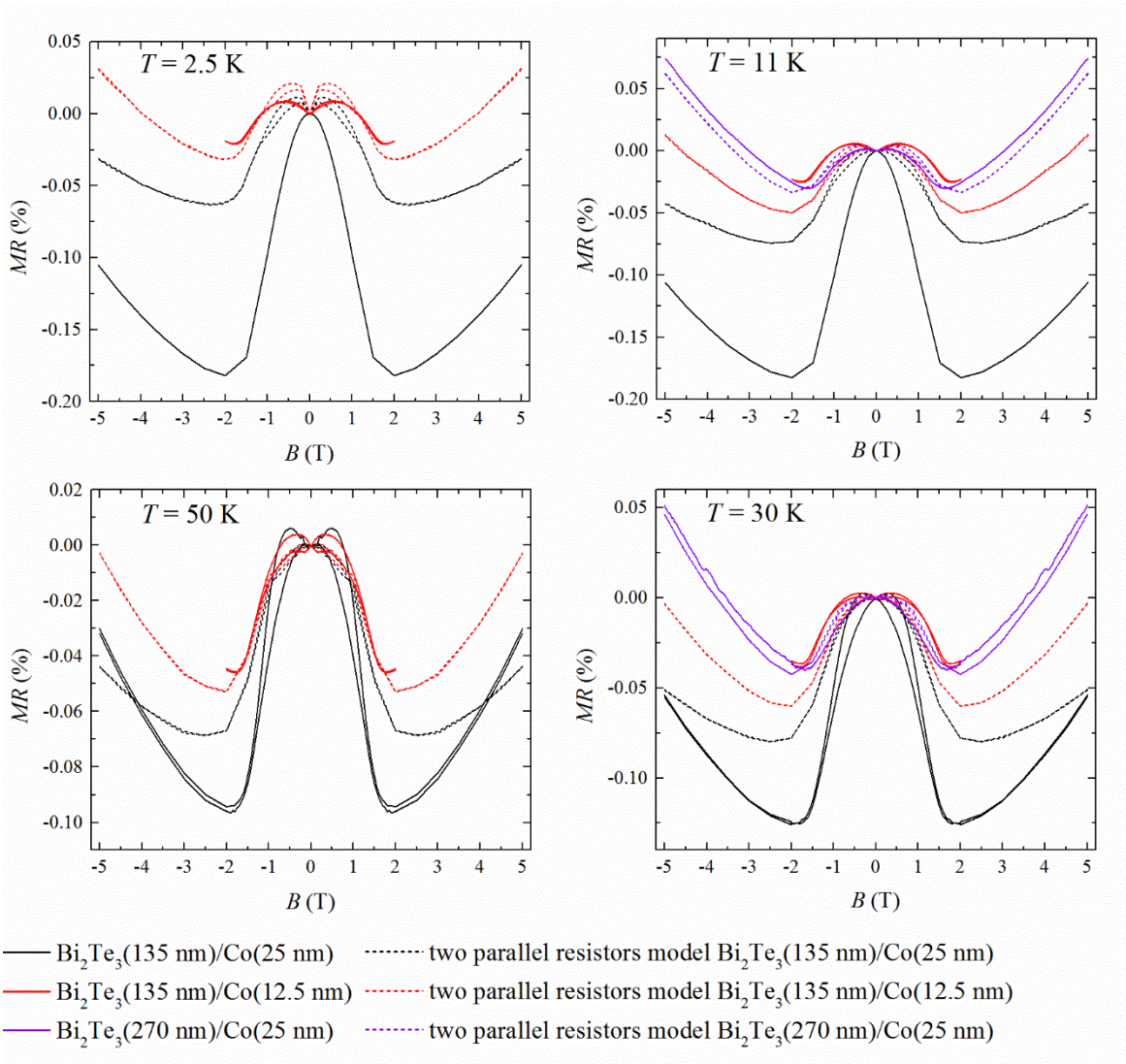

Figure 17. *Comparison of the measured MR curves for the bilayer structures with respect to the two parallel resistors model for T = 2.5, 11, 30 and 50 K.*

Structural and magnetotransport properties of Mn doped Bi_2Te_3 thin films

In this work we describe a thorough study of the structural, and magnetotransport properties of Mn-doped Bi_2Te_3 thin films grown by magnetron sputtering. The substitution of bismuth from manganese was performed by repeating ten times an alternating deposition of Bi_2Te_3 and Mn layers. The crystal structure is the tetradymite with the (00*l*) preferential orientation. Magneto-conductance data shows weak anti-localization phenomena at low temperatures. The presence of ferromagnetism is also demonstrating a strong anomalous Hall effect and the sign of AHE resistances changes from negative to positive as the Mn concentration increases.

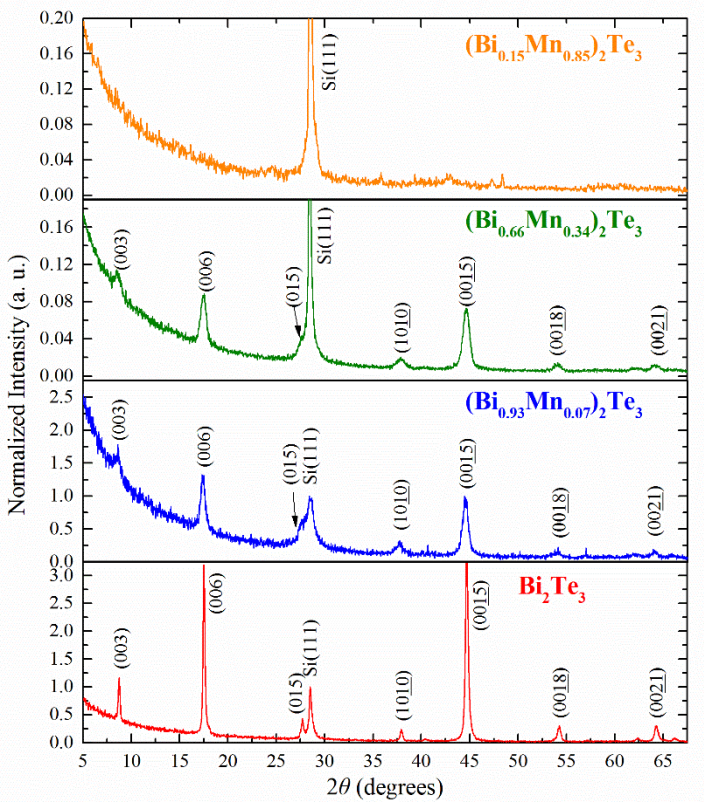

Figure 18. *XRD patterns for $(Bi_{1-x}Mn_x)_2Te_3$ thin films, with an estimated thickness of 200 nm and a doping concentration of Mn x=0, 0.07, 0.34 and 0.85.*

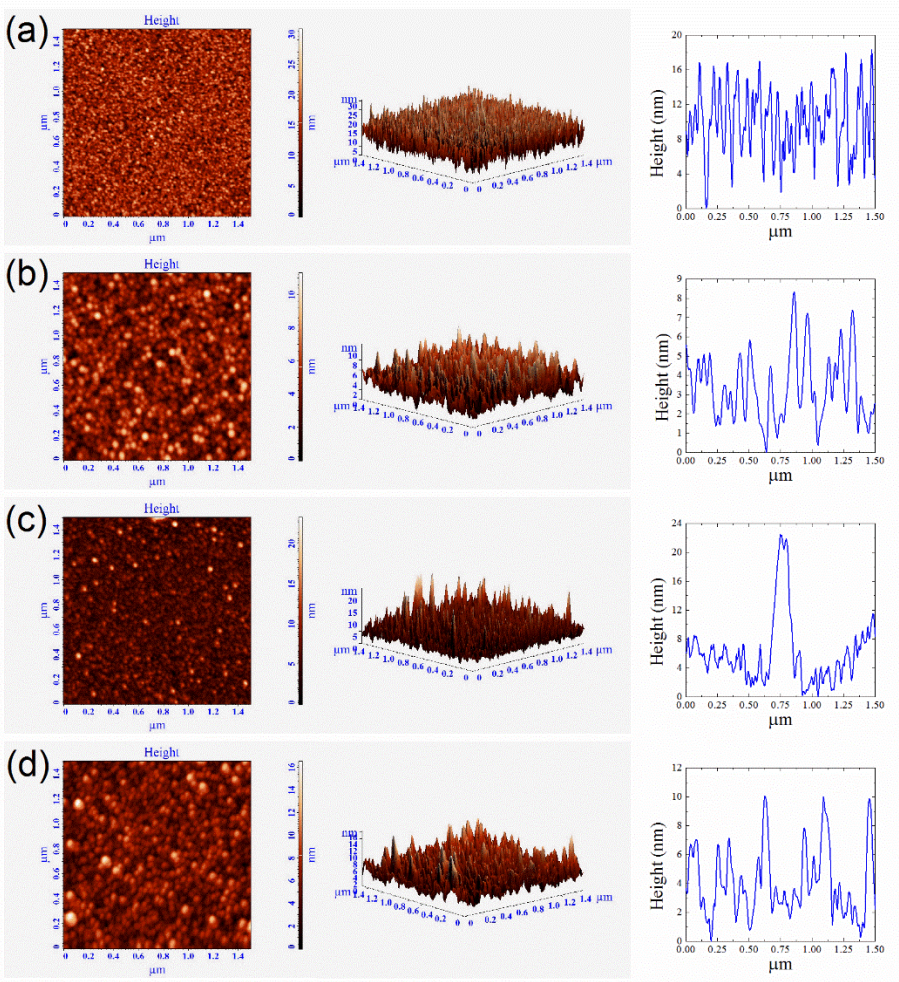

Figure 19. *AFM scans for a surface of 1.5x1.5 µm² for thin films of $(Bi_{1-x}Mn_x)_2Te_3$ with doping concentration of (a) x=0, (b) x=0.07, (c) x=0.34 and (d) x=0.85. For each scan the 3D representation and last scan height profile are presented.*

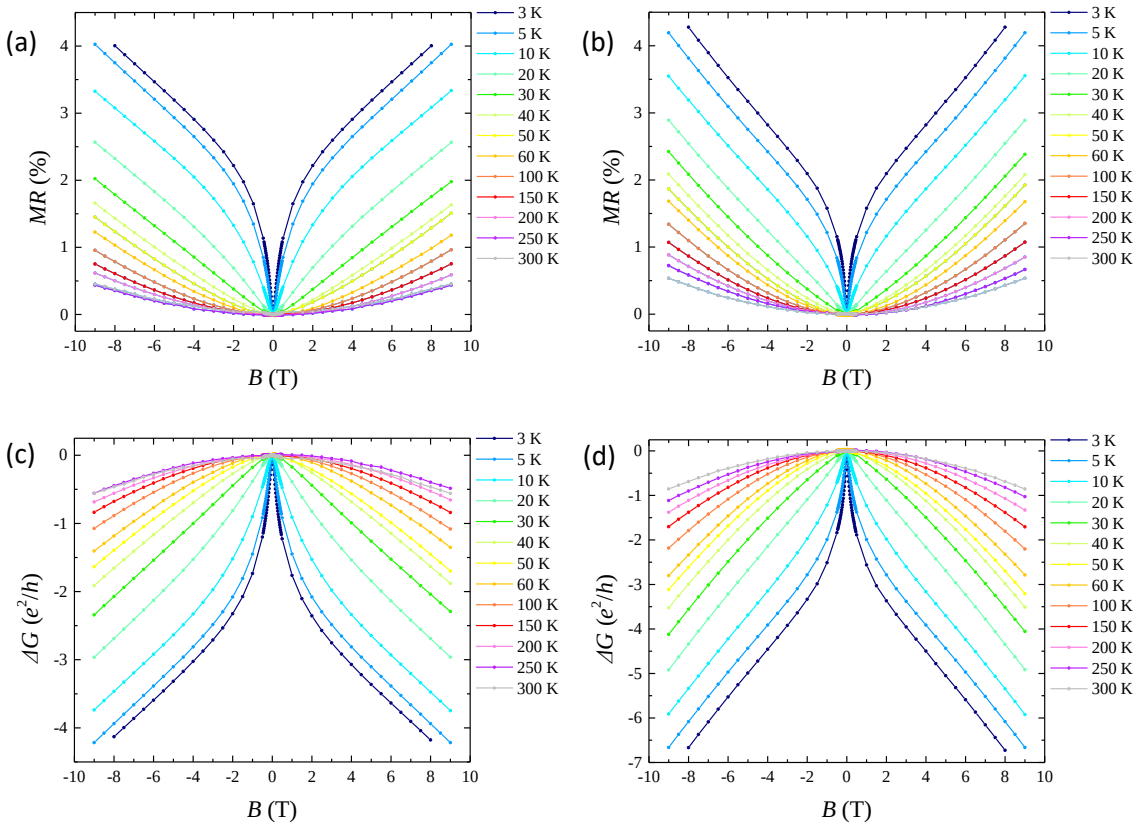

Figure 20. *(a) και (b) MR curves for the samples $(Bi_{1-x}Mn_x)_2Te_3$ with concentration of Mn x=0.34 and x=0.85, respectively. (c) and (d) Magnetoconductance plots for the measurements presented in (a) and (b) respectively.*

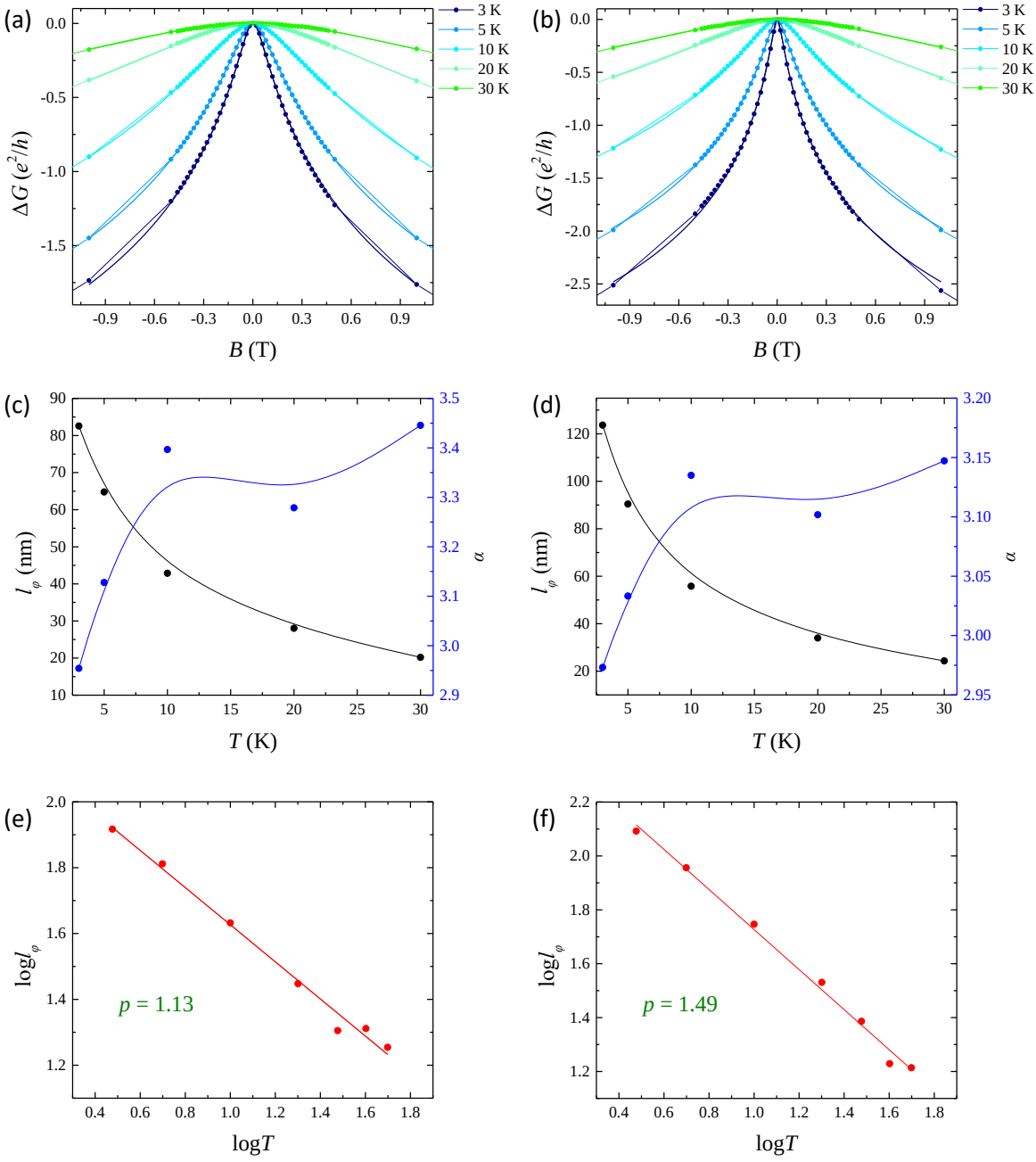

Figure 21. *(a) and (b) Fitting to LHN equation, for temperatures up to 30 K,for the magnetoconductance curves of the samples $(Bi_{1-x}Mn_x)_2Te_3$ for the concentrations of x=0.34 and x=0.85, respectively. (c) and (d) Parameters α and l_φ versus temperature, as extracted from the fitting (a) and (b), respectively. (e) and (f) $\log l_\varphi = f(\log T)$ plot, for the phase coherence length, l_φ, that are presented in (c) and (d) from which the dephasing mechanism is predicted via linear fitting.*

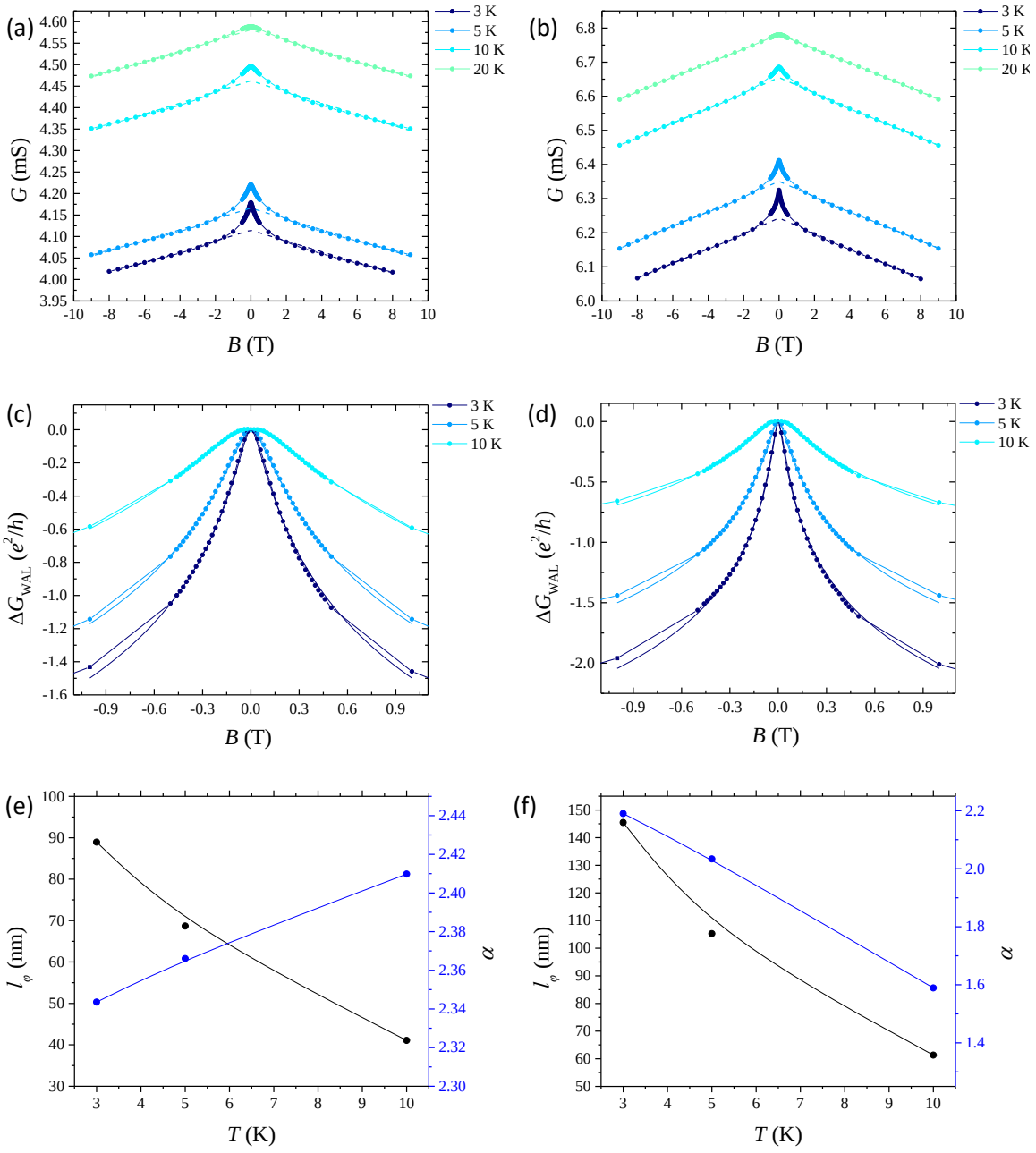

Figure 22. *(a) and (b) Estimation of the linear MR contribution to magnetoconductance for the films of $(Bi_{1-x}Mn_x)_2Te_3$, with x = 0.34 and 0.85, respectively. (c) and (d) Contribution of weak antilocalization to magnetoconductance following the extraction of the linear MR contribution as estimated in plots (a) and (b), respectively. (e) and (f) Fitting parameters to the HLN formula as extracted from the corresponding fitting after subtracting the linear MR contribution, for x = 0.34 and x = 0.85, respectively.*

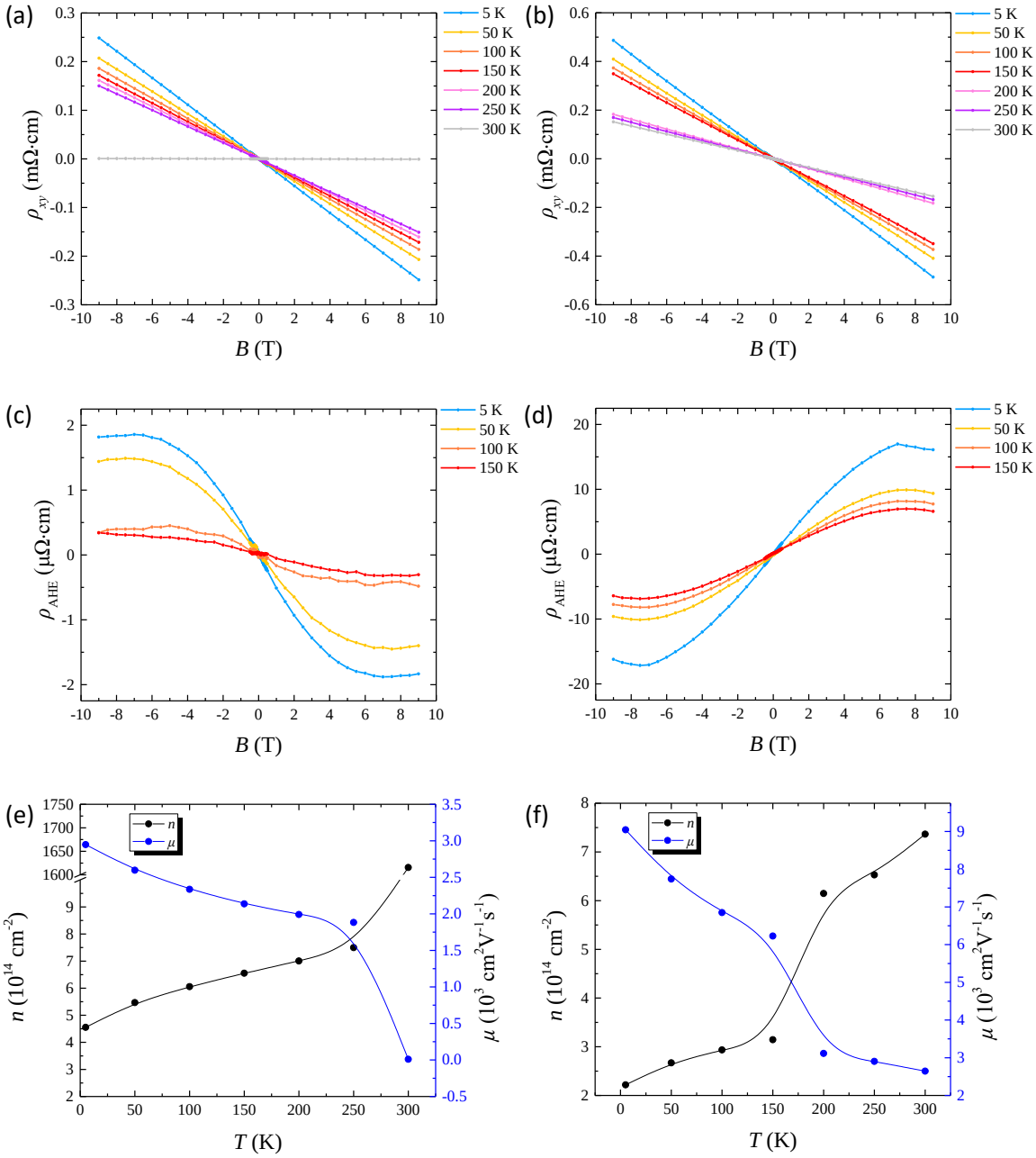

Figure 23. *(a) and (b) Hall resistance measurements, ρ_{xy}, for the thin films $(Bi_{1-x}Mn_x)_2Te_3$ with x = 0.34 and x = 0.85, respectively. (c) and (d) The contribution of the anomalous Hall effect in ρ_{xy} after subtracting the contribution of ordinary Hall effect from the measurements of (a) and (b), respectively. (e) and (f) Density and mobility of carriers for the concentrations of x = 0.34 and x = 0.85, respectively.*

Structural and magnetotransport properties of Co doped Bi_2Te_3 thin films

In this work we investigate the growth and magnetotransport properties of Co doped topological insulator Bi_2Te_3 deposited on Si(111) substrates by means of DC magnetron sputtering. The structure and morphology of the films were studied using X-Ray Diffraction (XRD), Field-Emission Scanning Electron Microscopy (FESEM) and Atomic Force Microscopy (AFM). Magnetotransport measurements were performed with a Physical Property Measurement System (PPMS). The pristine samples have a metallic behavior while the Co-doped are semiconductors. The magnetoresistance curves exhibit a sharp cusp for temperatures below 20 K that correspond to weak antilocalization phenomena and are analysed using the Hikami-Larkin-Nagaoka model. The WAL phenomenon vanishes with temperature increase due to electron-phonon scattering. The doped samples present an ambipolar transport with a change in the sign of the dominant carriers with temperature.

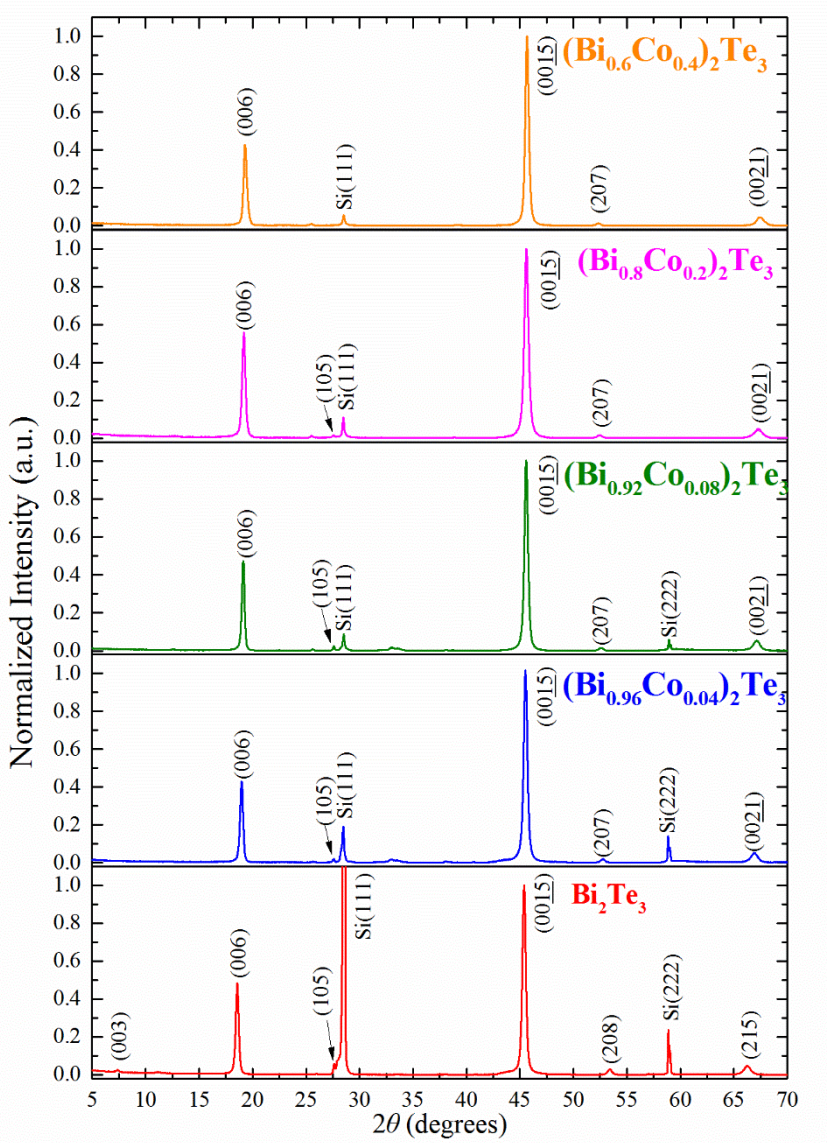

Figure 24. *XRD patterns for $(Bi_{1-x}Co_x)_2Te_3$ thin films with doping concentrations of Co, x=0, 0.04, 0.08, 0.2 and 0.4.*

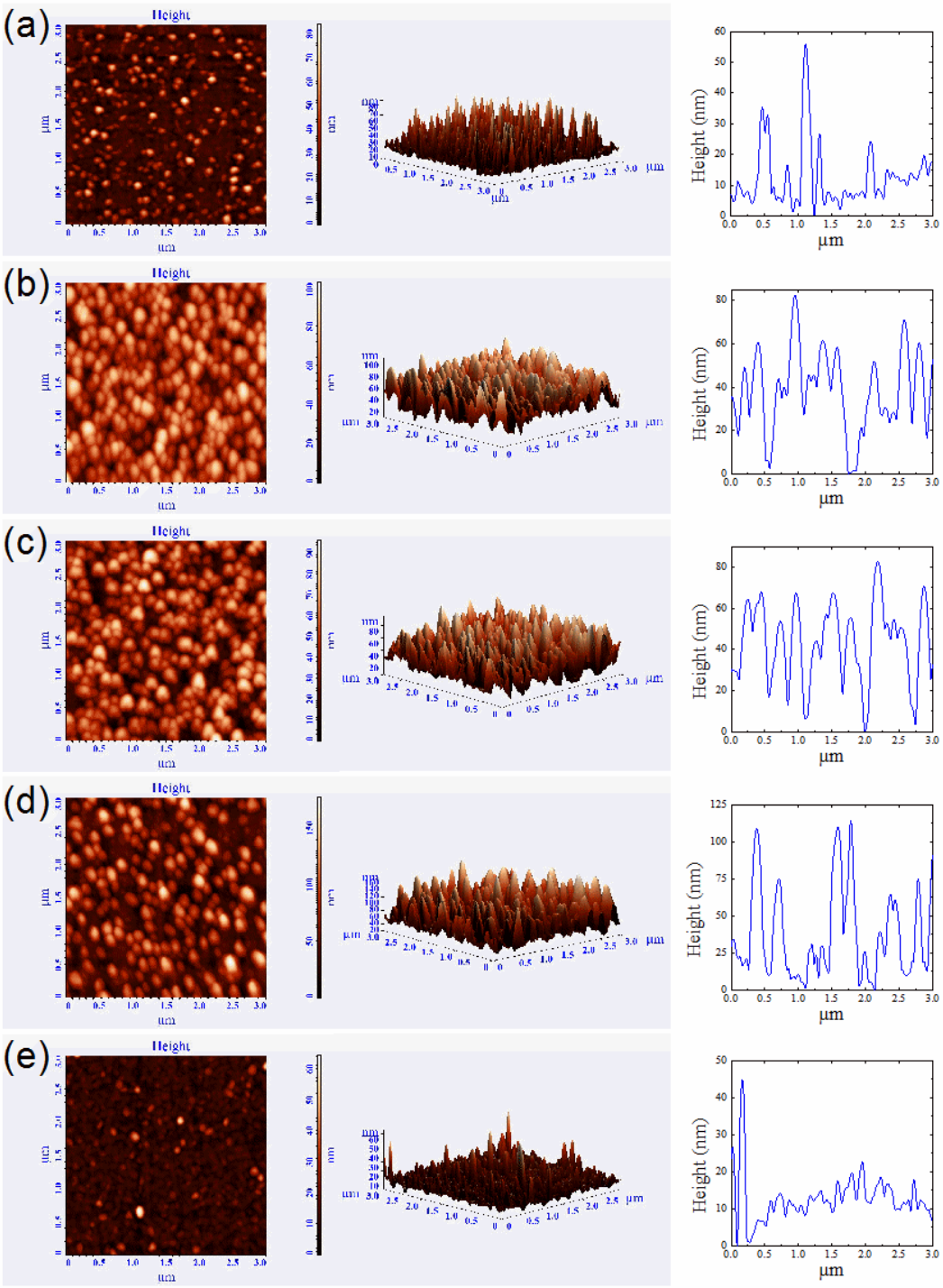

Figure 25. *AFM scans of a 3x3 μm^2 surface, for thin films of $(Bi_{1-x}Co_x)_2Te_3$ for concentrations of Co (a) x=0, (b) x=0.04, (c) x=0.08, (d) x=0.2 and x=0.4. For each scan the 3D representation and last scan height profile are presented.*

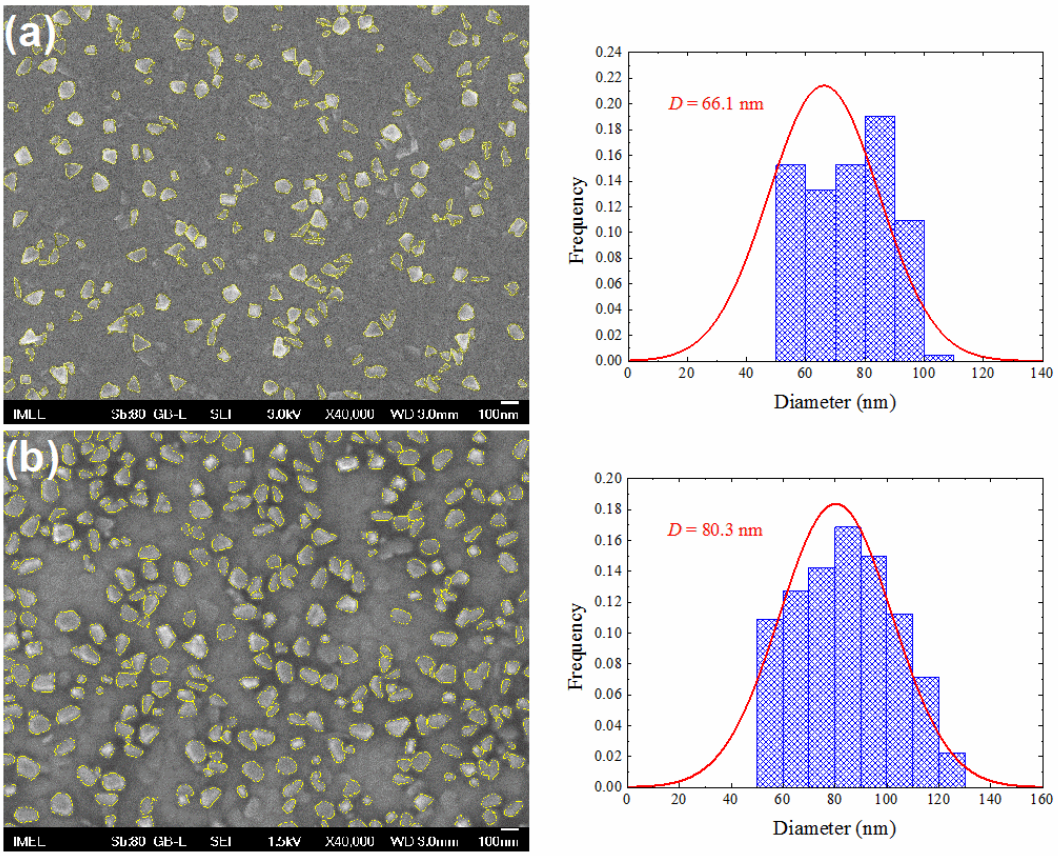

Figure 26. *FESEM scans for (a) Bi_2Te_3 and (b) $(Bi_{0.96}Co_{0.04})_2Te_3$ thin films. Each scan is accompanied by the grain diameter distribution plot.*

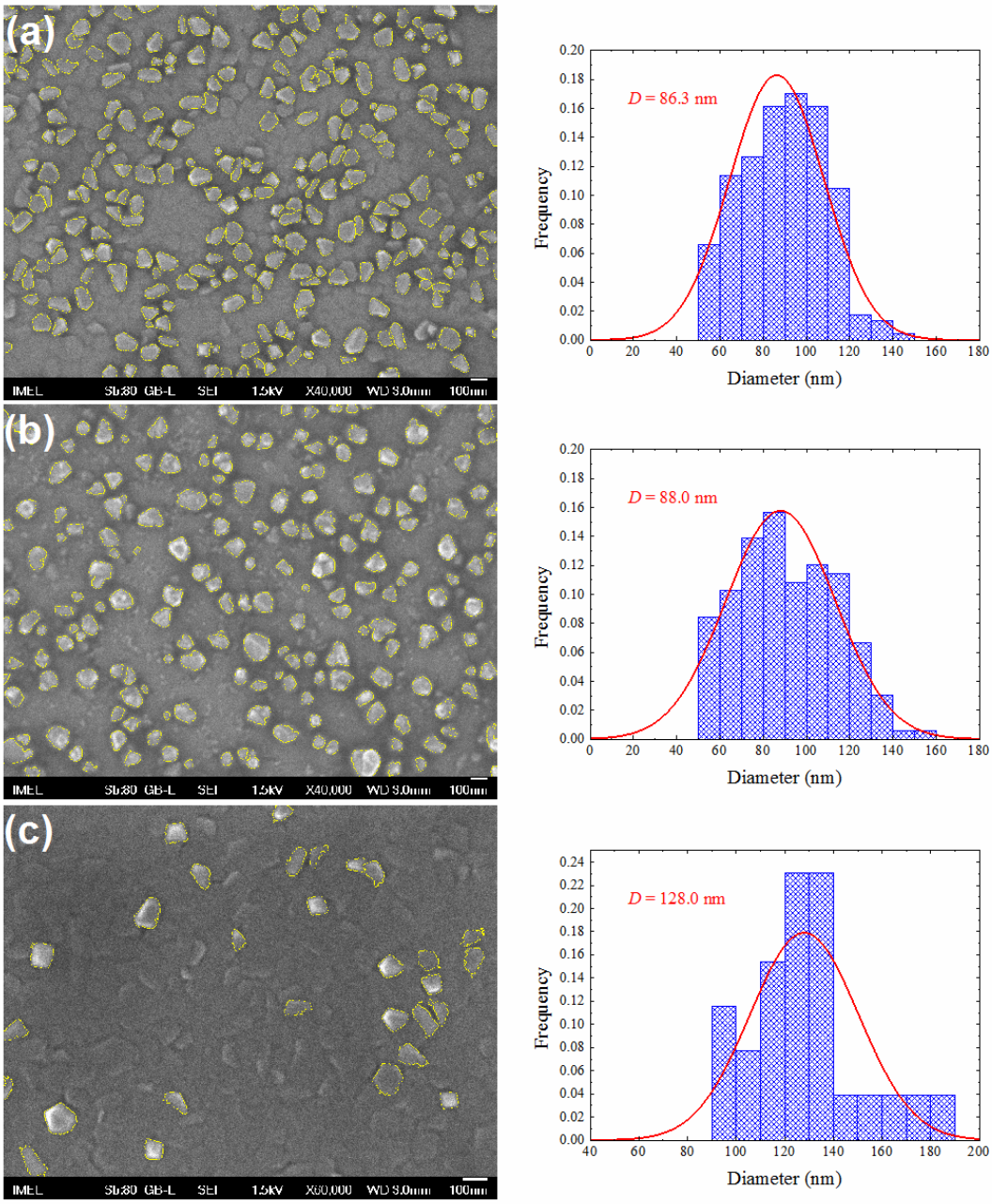

Figure 27. *FESEM scans for (a) $(Bi_{0.92}Co_{0.08})_2Te_3$, (b) $(Bi_{0.8}Co_{0.2})_2Te_3$ and (c) $(Bi_{0.6}Co_{0.4})_2Te_3$ thin films. Each scan is accompanied by the grain diameter distribution plot.*

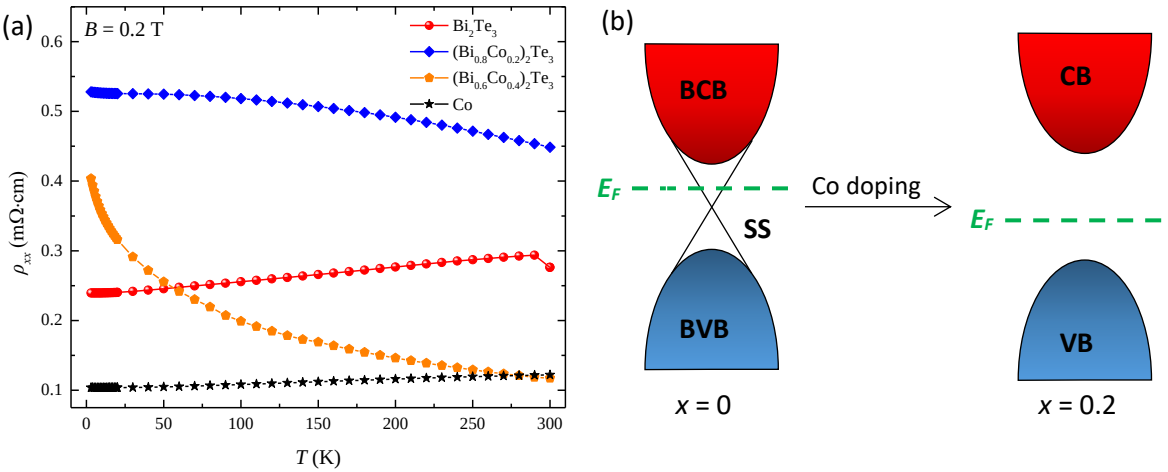

Figure 28. *(a) Longitudinal resistance measurements, ρ_{xx}, with respect to temperature, under stable magnetic field of B=0.2 T, for the reference samples Bi_2Te_3 and Co and the samples doped with Co, $(Bi_{0.8}Co_{0.2})_2Te_3$ and $(Bi_{0.6}Co_{0.4})_2Te_3$. (b) Band structure, as estimated from the measurements $\rho_{xx}(T)$ and $\rho_{xy}(B)$, for the reference sample Bi_2Te_3 and the sample $(Bi_{0.8}Co_{0.2})_2Te_3$.*

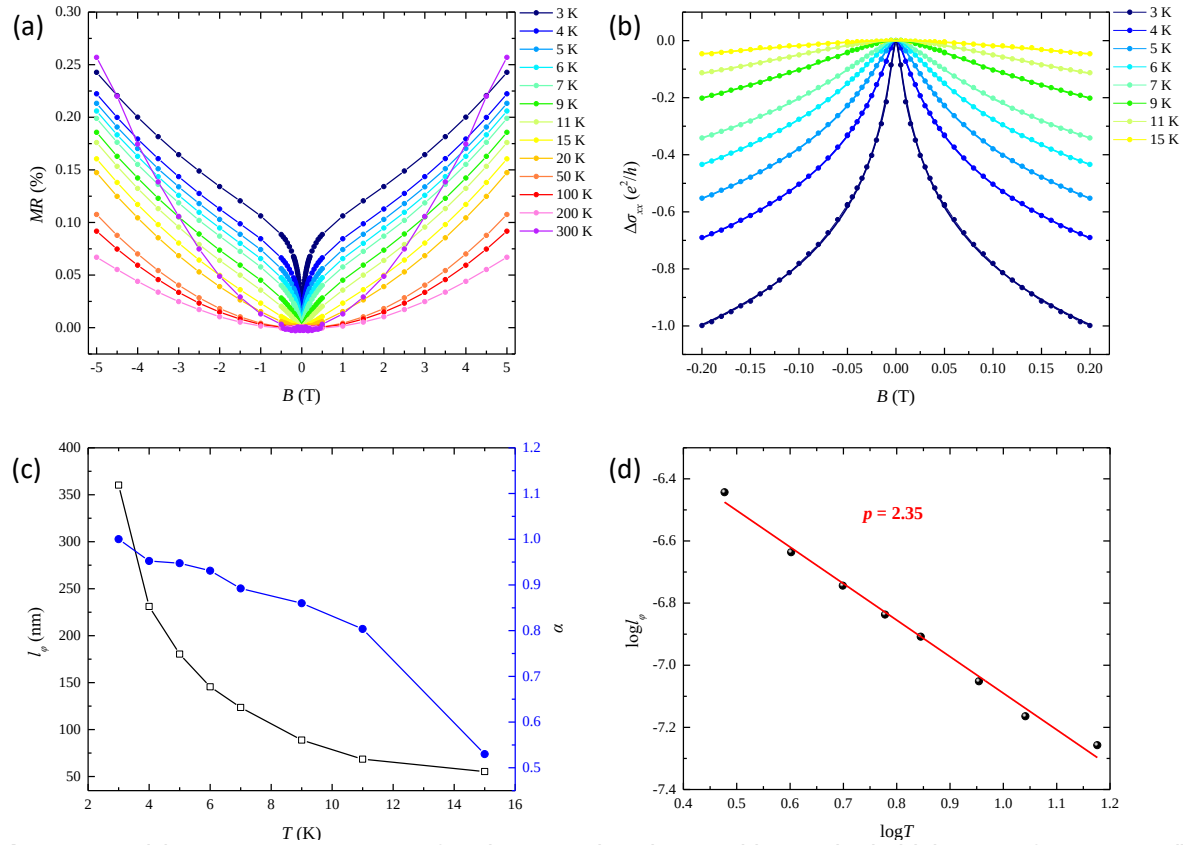

Figure 29. *(a) MR measurements for the sample Bi_2Te_3 with nominal thickness of 135 nm. (b) Magnetoconductance curves and the corresponding fitting to HLN formula for temperatures up to 15 K. (c) Parameters, α and l_φ, extracted from the fittings in (b), versus temperature. (d) $\log l_\varphi = f(\log T)$ for the estimation of dephasing mechanism.*

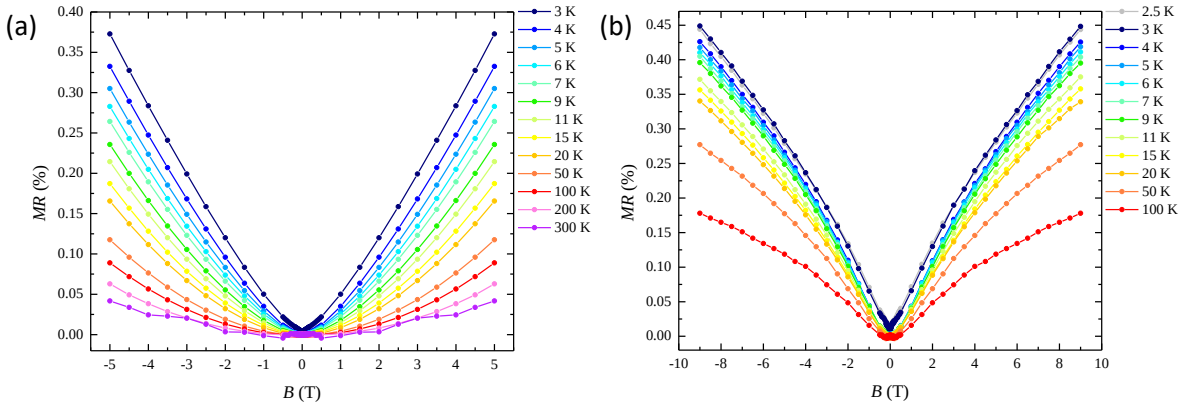

Figure 30. *MR measurements for thin films of (a) $(Bi_{0.8}Co_{0.2})_2Te_3$ and (b) $(Bi_{0.6}Co_{0.4})_2Te_3$.*

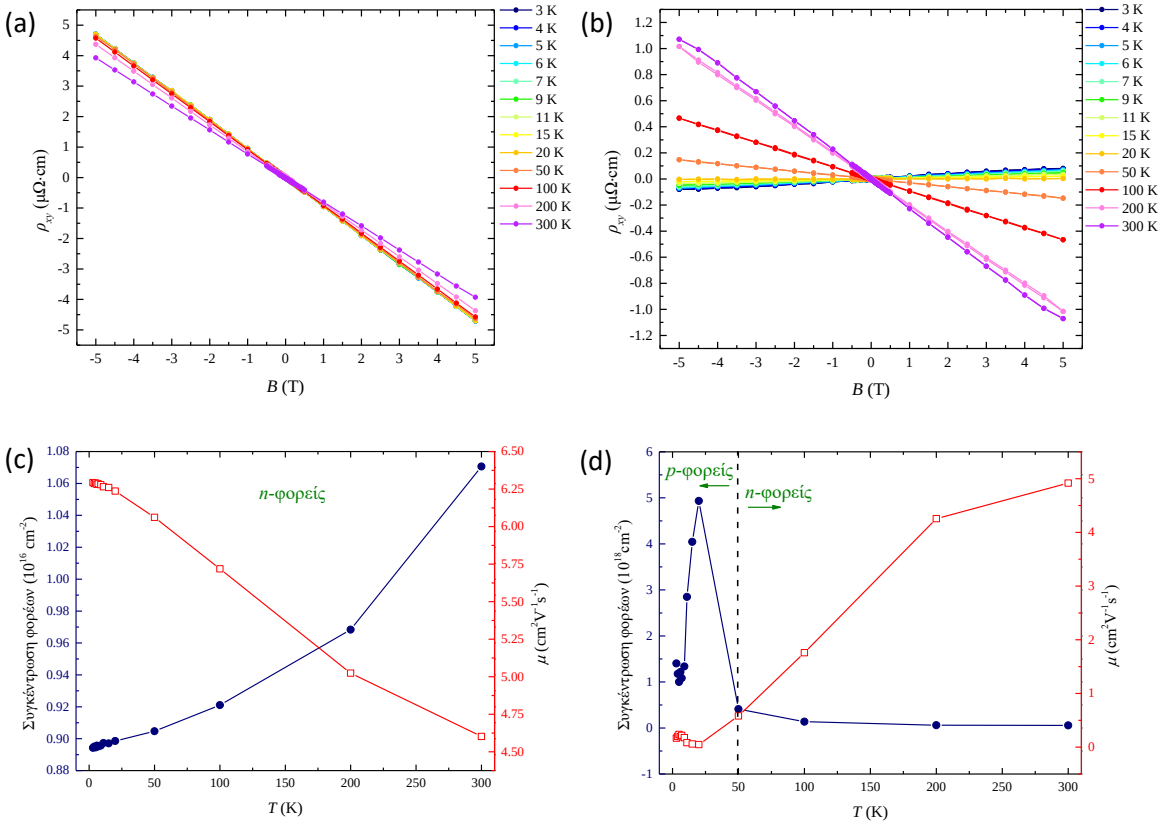

Figure 31. *(a) and (b) Hall resistance measurements for the reference sample Bi_2Te_3 and the sample $(Bi_{0.8}Co_{0.2})_2Te_3$, respectively. (c) and (d) Concentration and carrier mobility that were calculated from the plots (a) and (b), respectively.*

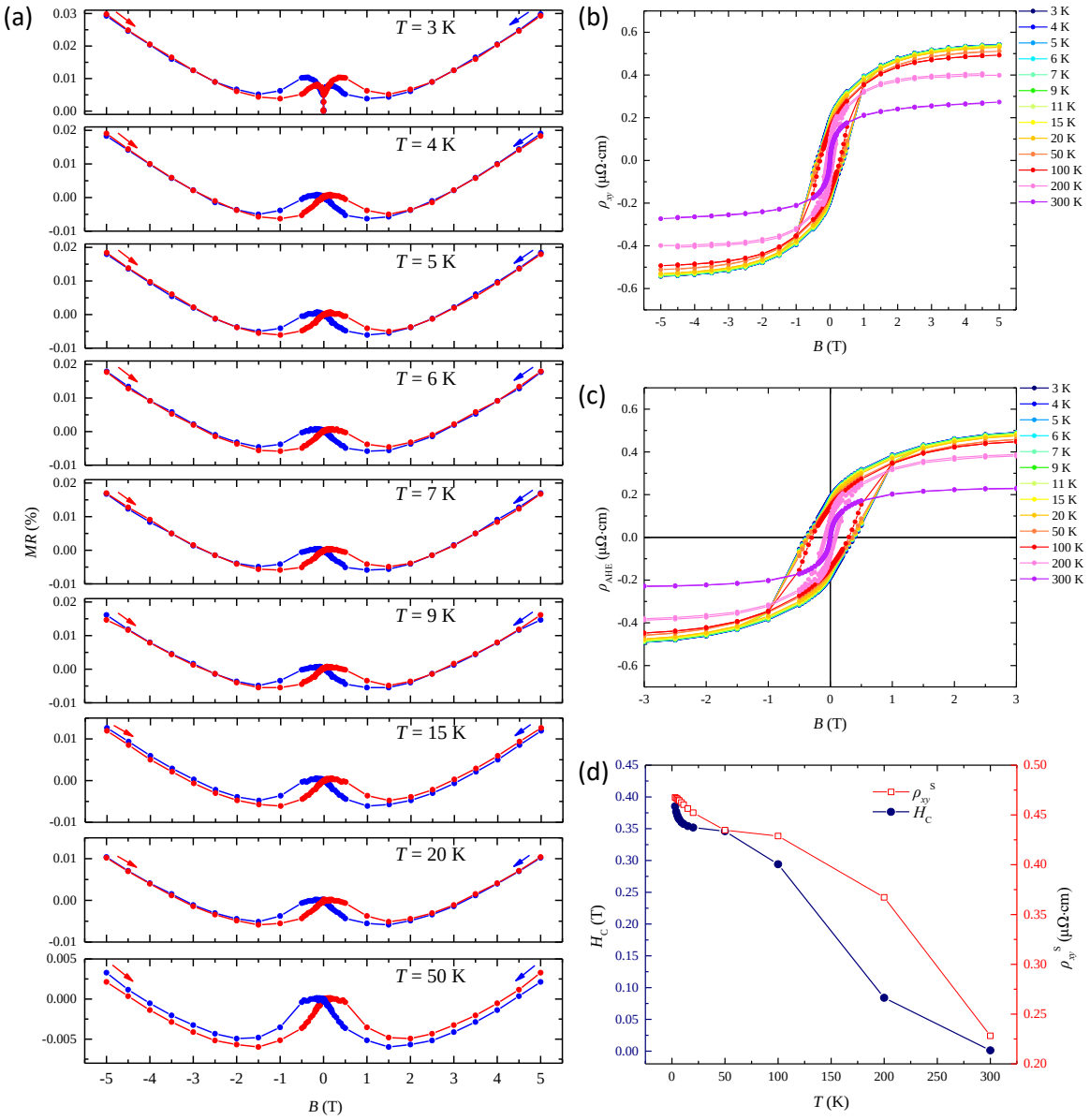

Figure 32. *(a) MR measurements and (b) Hall resistance measurements for the thin film reference of Co, with nominal thickness of 50 nm. (c) Contribution of anomalous Hall effect to Hall resistance. (d) Coercive field and spontaneous Hall resistance versus temperature.*

Structural and magnetotransport properties of Cr doped Bi_2Te_3 thin films

In this study we aim to prepare and characterize thin films of Cr-doped Bi2Te3. Doping with Cr leads to the development of intense ferromagnetic behavior, breaking of time reversal symmetry and opening of the band gap in the topological insulator. The films prepared show the presence of anomalous Hall effect that could probably lead to applications such as magnetic field sensors based on anomalous Hall effect. Below are presented the data of the structural, morphological and magnetotransport properties.

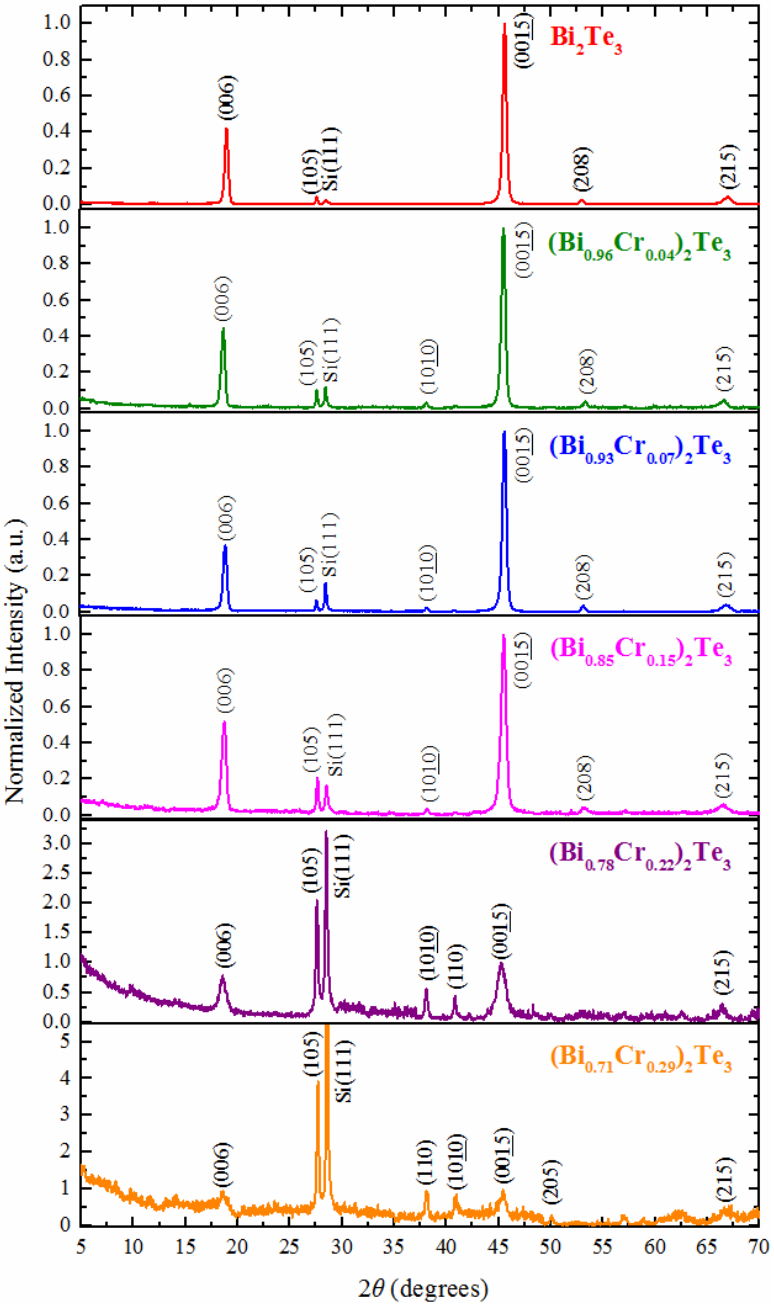

Figure 33. *XRD patterns for thin films of $(Bi_{1-x}Cr_x)_2Te_3$ with an estimated thickness of 200 nm, that have been doped with Cr in concentrations x=0,0.04,0.07,0.15,0.22 and 0.29.*

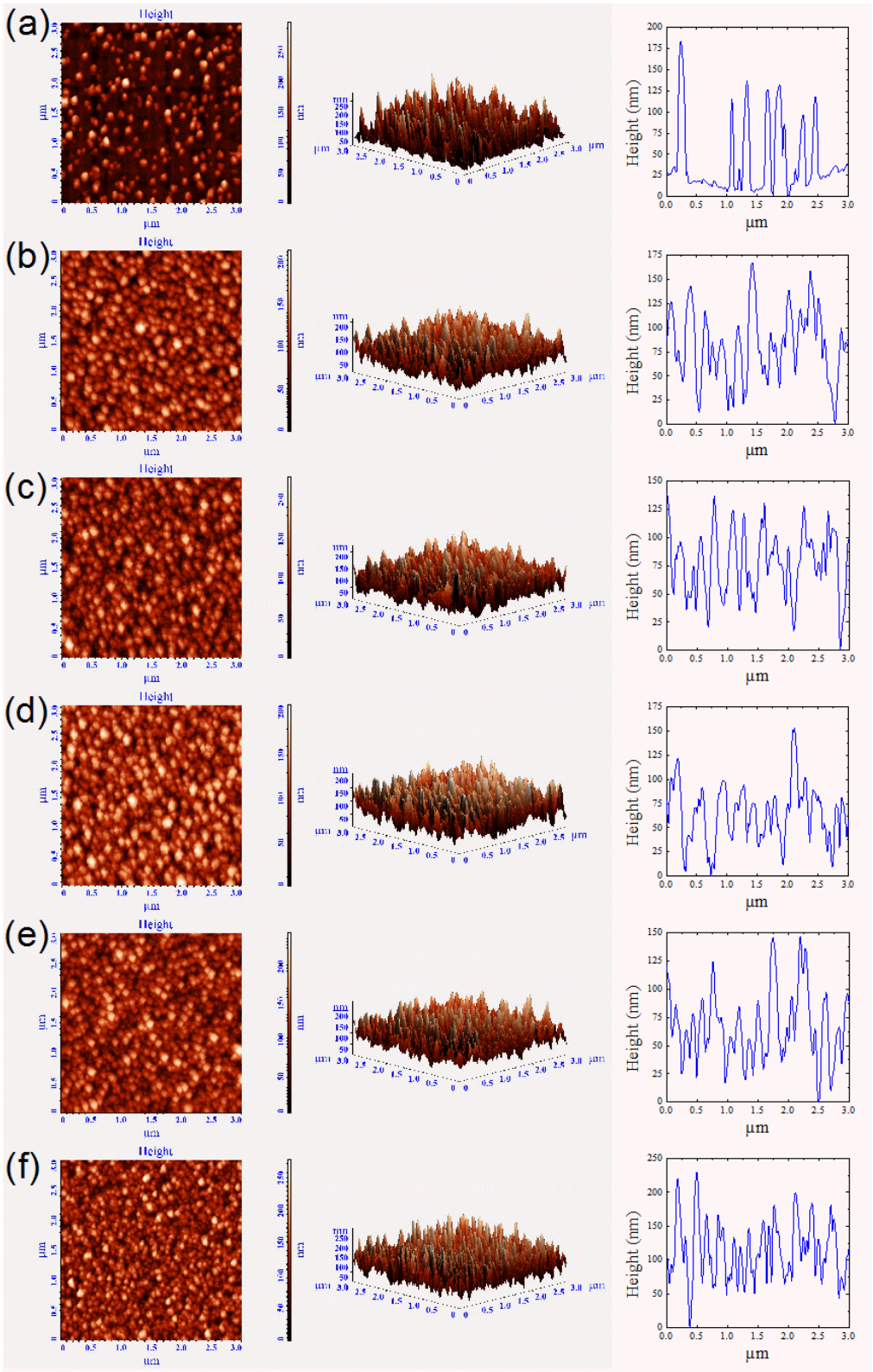

Figure 34. *AFM scans of a 3x3 µm² surface, for thin films of $(Bi_{1-x}Cr_x)_2Te_3$ for concentrations of Cr (a) x=0, (b) x=0.04, (c) x=0.07, (d) x=0.15, (e) x=0.22 and (f) x=0.29. Each scan is accompanied by the 3D representation and the last scan height profile.*

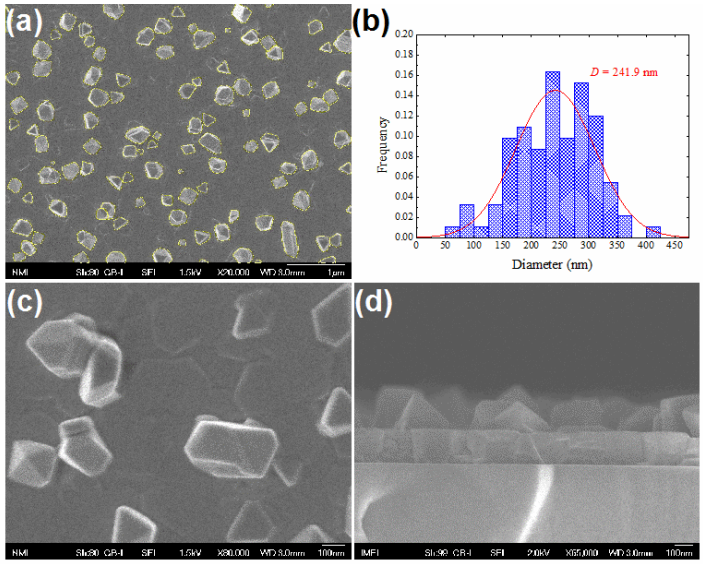

Figure 35. *FESEM scans for the Bi2Te3 sample with nominal thickness of 200 nm*. (a) and (c) Top view in magnifications of x20,000 and x80,000, respectively. (b) Grain diameter distribution extracted from picture (a), (d) Picture of the sample in cross-section.

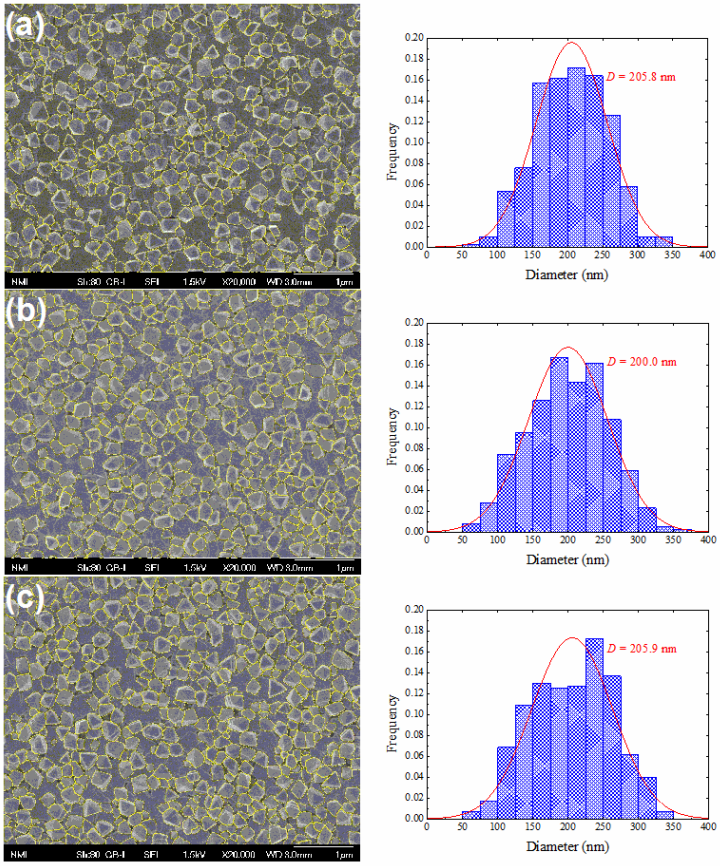

Figure 36. *FESEM scans for thin films of $(Bi_{1-x}Cr_x)_2Te_3$ with (a) x = 0.04, (b) x = 0.07 and (c) x= 0.15. Each scan is accompanied by the corresponding grain diameter distribution.*

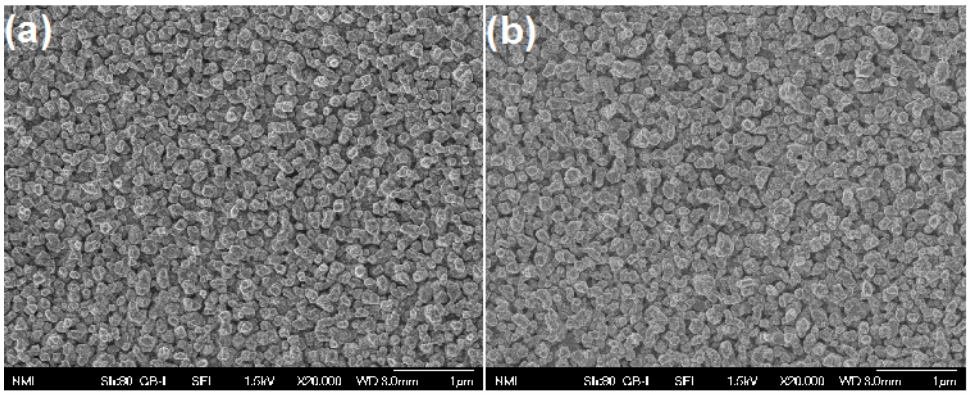

Figure 37. *FESEM scans for the thin films of $(Bi_{1-x}Cr_x)_2Te_3$ with (a) x = 0.22 and (b) x = 0.29.*

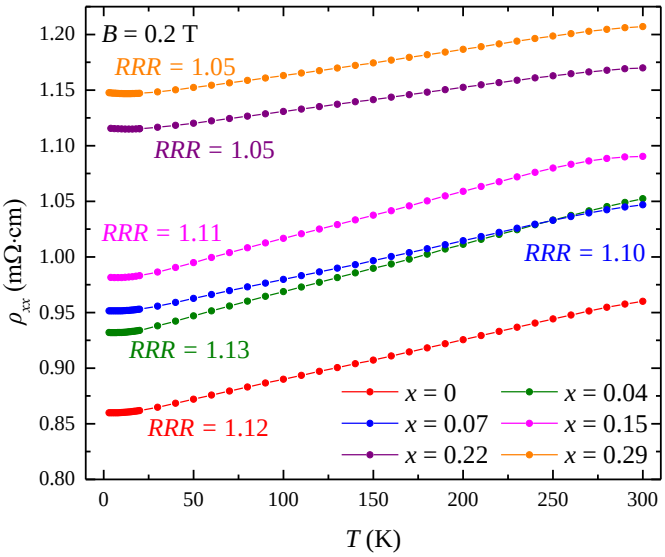

Figure 38. Measurements of longitudinal resistivity, ρ_{xx}, with variation of temperature, under fixed magnetic field of B=0.2 T, for thin films of $(Bi_{1-x}Cr_x)_2Te_3$ with x=0, 0.04, 0.07, 0.15, 0.22 and 0.29.

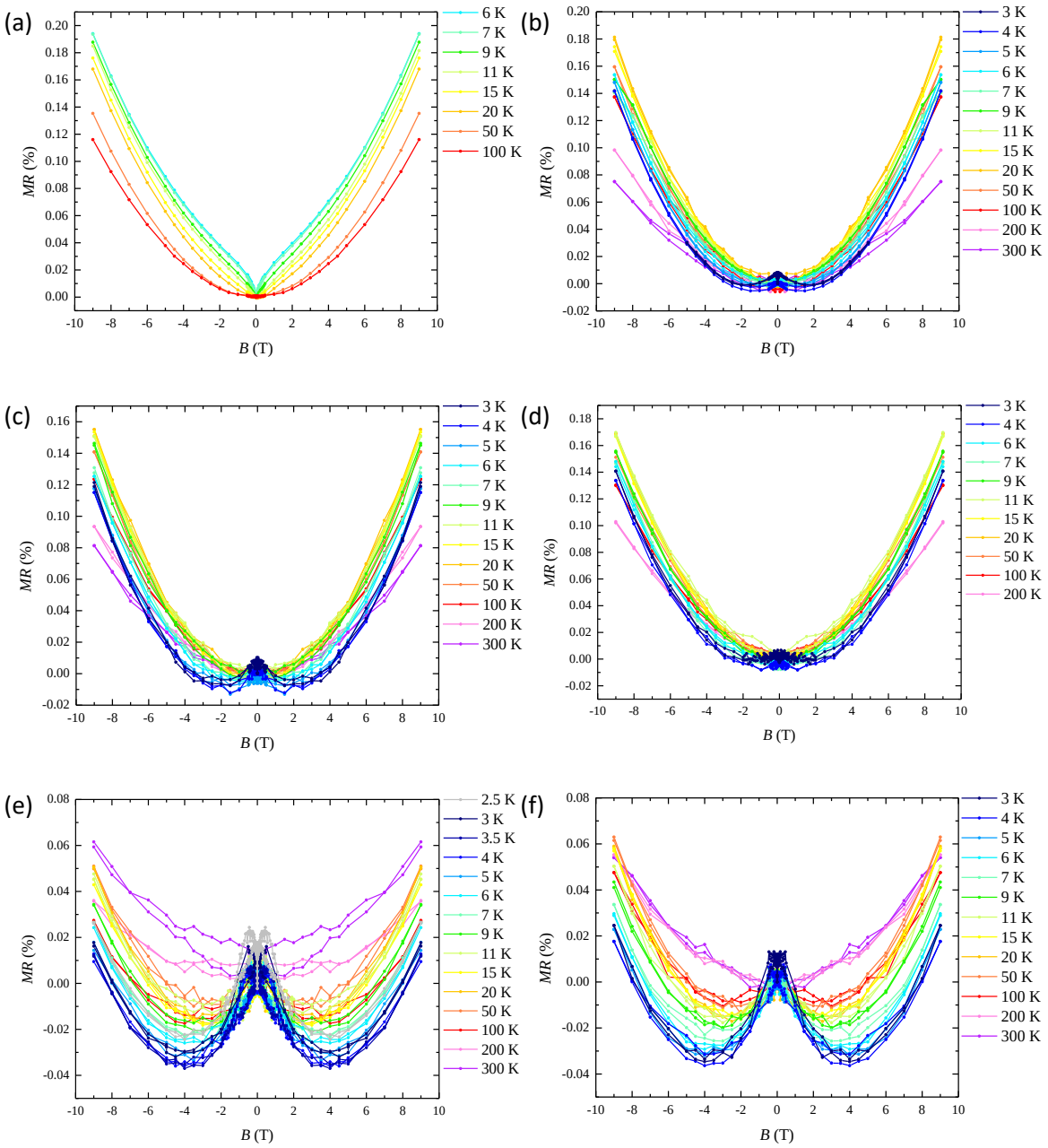

Figure 39. *MR measurements of thin films $(Bi_{1-x}Cr_x)_2Te_3$ with Cr concentration (a) x=0, (b) x=0.04, (c) x=0.07, (d) x=0.15, (e) x=0.15 and (f) x=0.29.*

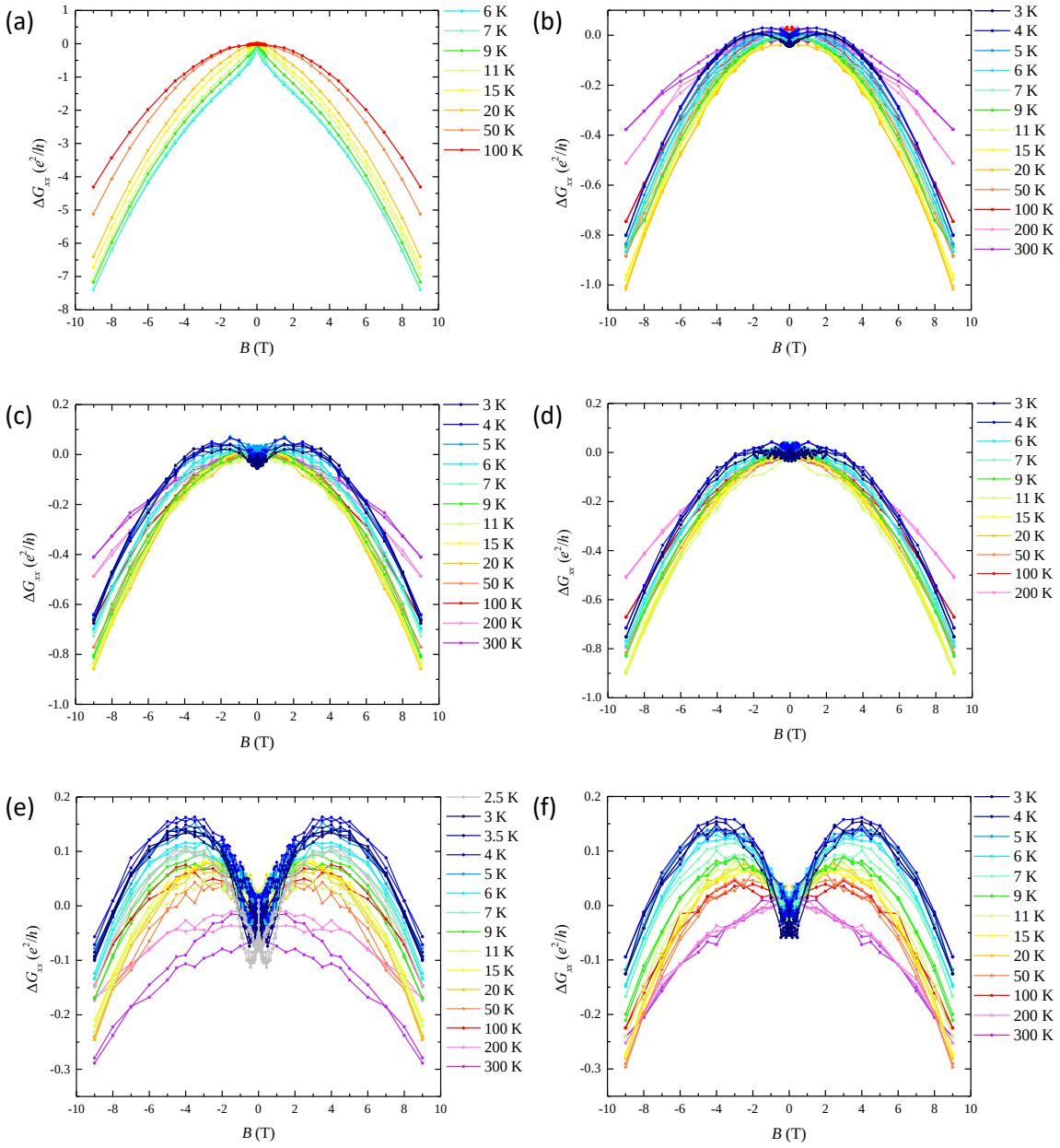

Figure 40. *Magnetoconductance curves, ΔG_{xx}, for thin films of $(Bi_{1-x}Cr_x)_2Te_3$ with Cr concentration (a) x=0, (b) x=0.04, (c) x=0.07, (d) x=0.15, (e) x=0.22 and (f) x=0.29.*

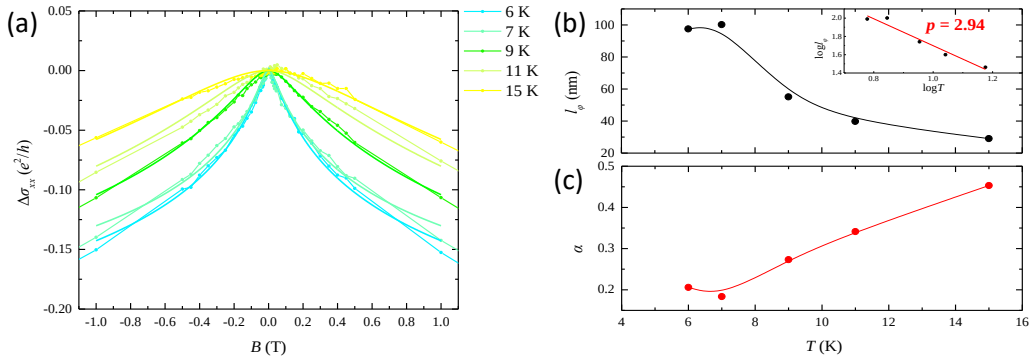

Figure 41. *(a) Fitting to HLN formula for the sample Bi_2Te_3 (x=0) with nominal thickness of 200 nm, (b) Phase coherence length, l_φ, and (c) prefactor α versus temperature.*

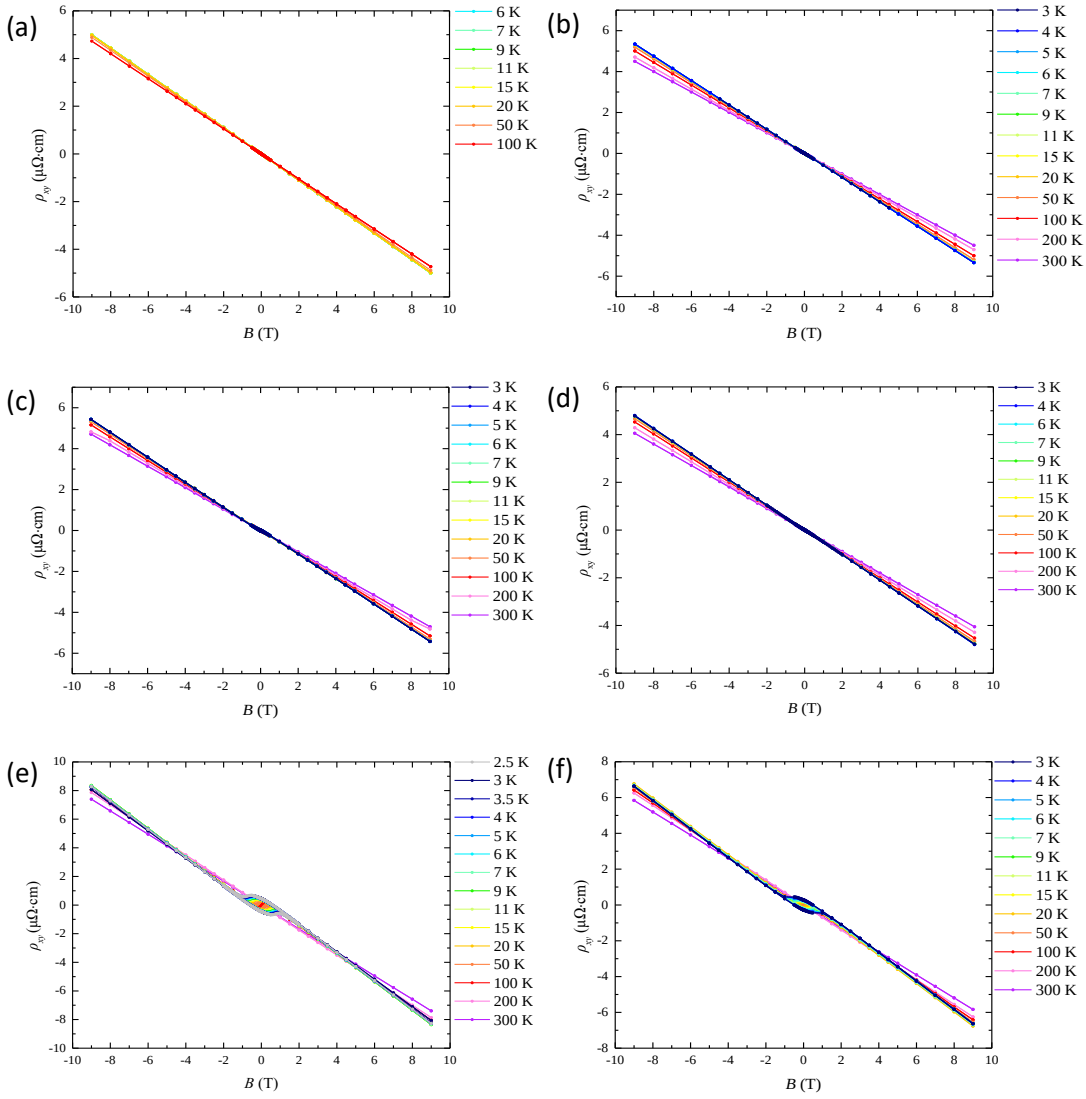

Figure 42. *Hall resistance measurements, ρxy, for thin films $(Bi_{1-x}Cr_x)_2Te_3$ with Cr concentration of (a) x=0, (b) x=0.04, (c) x=0.07, (d) x=0.15, (e) x=0.22 and (f) x=0.29.*

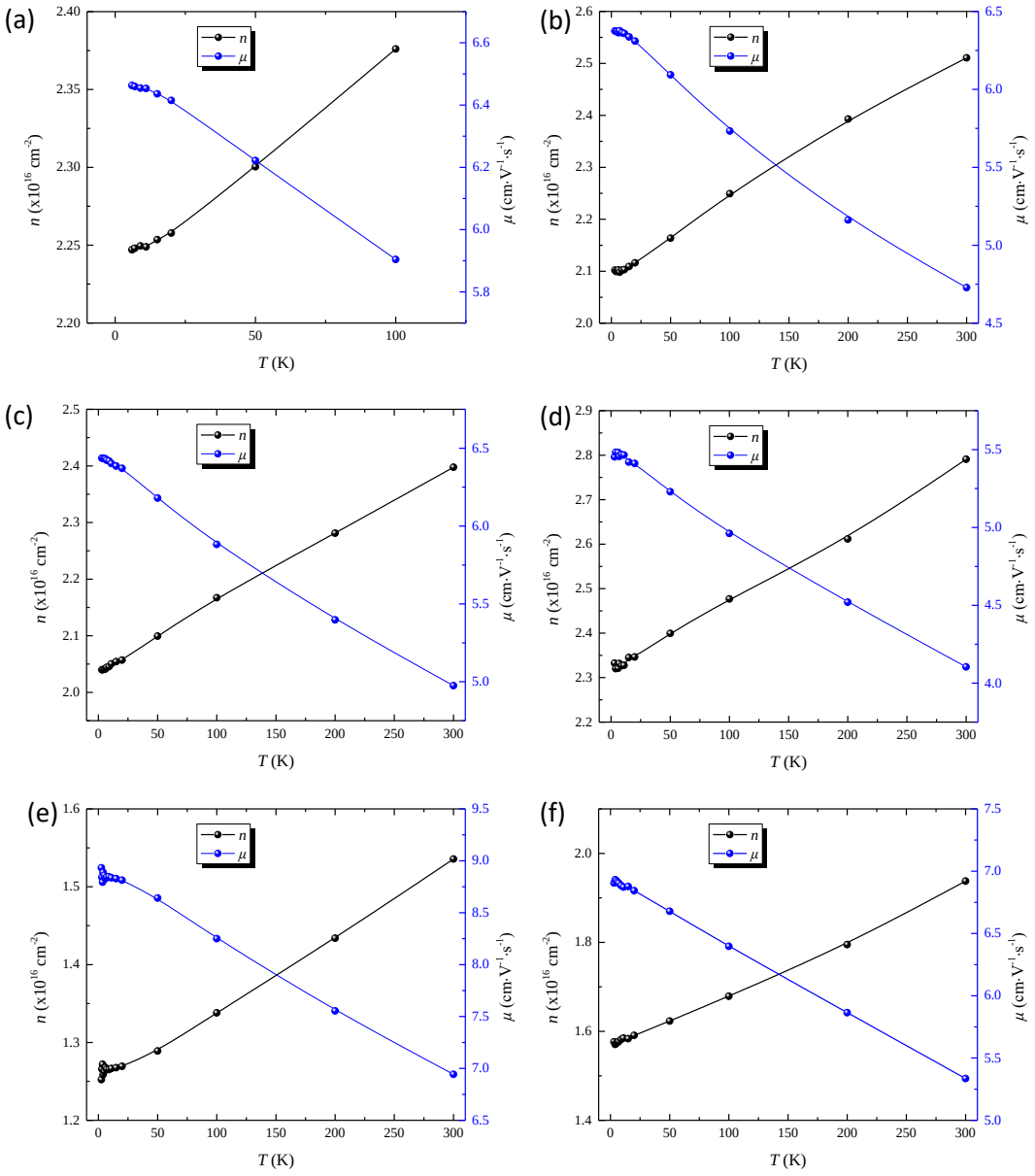

Figure 43. *Carrier density for thin films of $(Bi_{1-x}Cr_x)_2Te_3$ with Cr concentration of (a) x=0, (b) x=0.04, (c) x=0.07, (d) x=0.15, (e) x=0.22 and (f) x=0.29.*

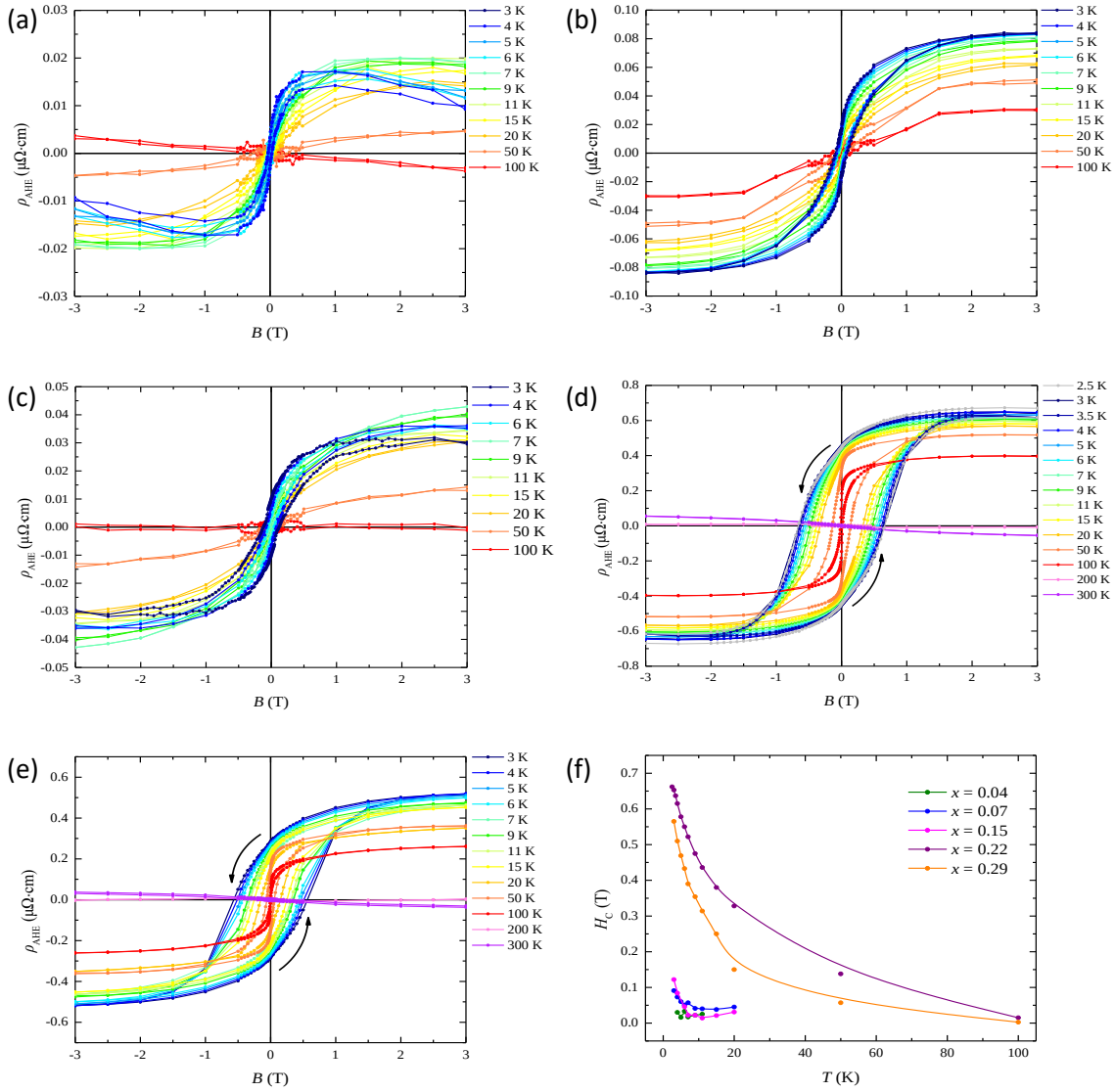

Figure 44. *Anomalous Hall effect contribution, ρ_{AHE}, for thins films of $(Bi_{1-x}Cr_x)_2Te_3$ with Cr concentration (a) x=0.04, (b) x=0.07, (c) x=0.15, (d) x=0.22 and (e) x=0.29. (f) Coercive filed versus temperature extracted graphically from plots (a)-(e).*

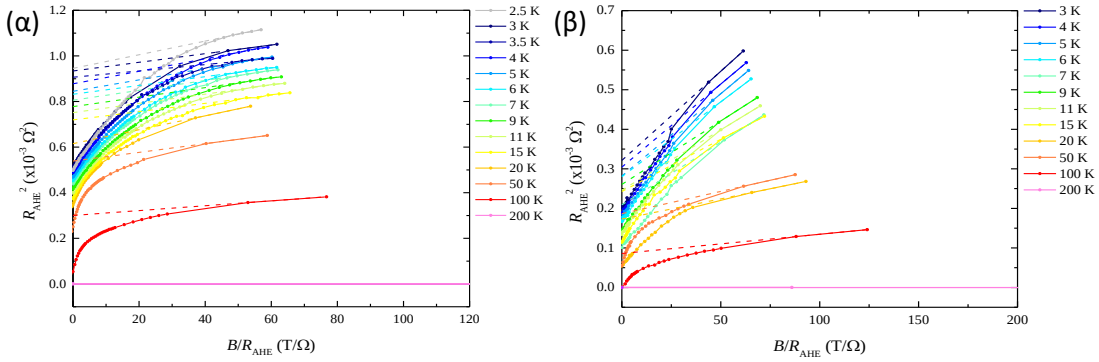

Figure 45. *Arrott plots for thin films of $(Bi_{1-x}Cr_x)_2Te_3$ with Cr concentrations of (a) x=0.22 and (b) x=0.29.*

Topological Superonductivity

Bi_2Te_3 is a three-dimensional topological insulator, whose surface exhibits metallic electronic states, while its bulk is effectively free of mobile charge carriers. These states are formed by topological effects that also render the electrons travelling on such surfaces insensitive to scattering by impurities. Such topological insulators combined with a superconductor may provide new routes to the study of transport through their unconventional surface states. Here, we show transport experiments on Bi_2Te_3/Nb bilayer and Nb/Bi_2Te_3/Nb trilayer, a system which is important to investigate the appearance of the predicted Majorana states at the interface between a topological insulator and a superconductor. Interestingly, with the measurements at 3 K we observe that the onset of superconductivity of Nb layer, that is adjacent to the topological insulator, creates novel phenomena that arise from the interplay between a superconductor and a topological insulator with a superconducting state at the surfaces of Bi_2Te_3.

Our results show that Bi2Te3 is a promising material system to get a better understanding of the superconducting proximity effect in topological surface states, and to examine the appearance of zero-energy Majorana states in transport experiments.

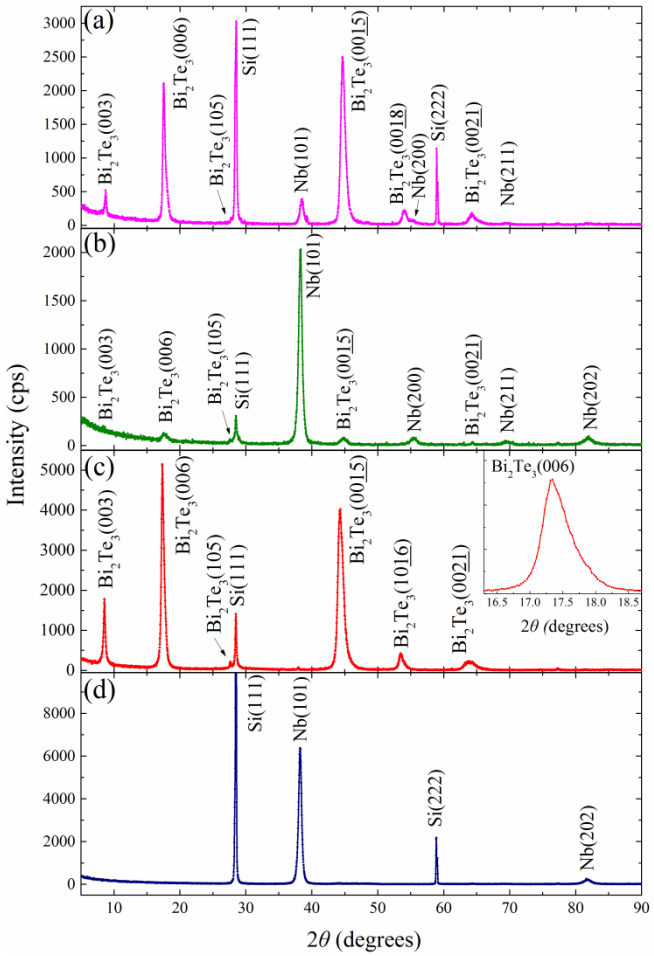

Figure 46. *XRD patterns for (a) Si(111)/Bi_2Te_3(100 nm)/Nb(100 nm) bilayer sample, (b) Si(111)/Nb(100 nm)/Bi_2Te_3(40 nm)/Nb(100 nm) trilayer sample, (c) Si(111)/Bi_2Te_3(40 nm) and (d) Si(111)/Nb(100 nm) reference samples.*

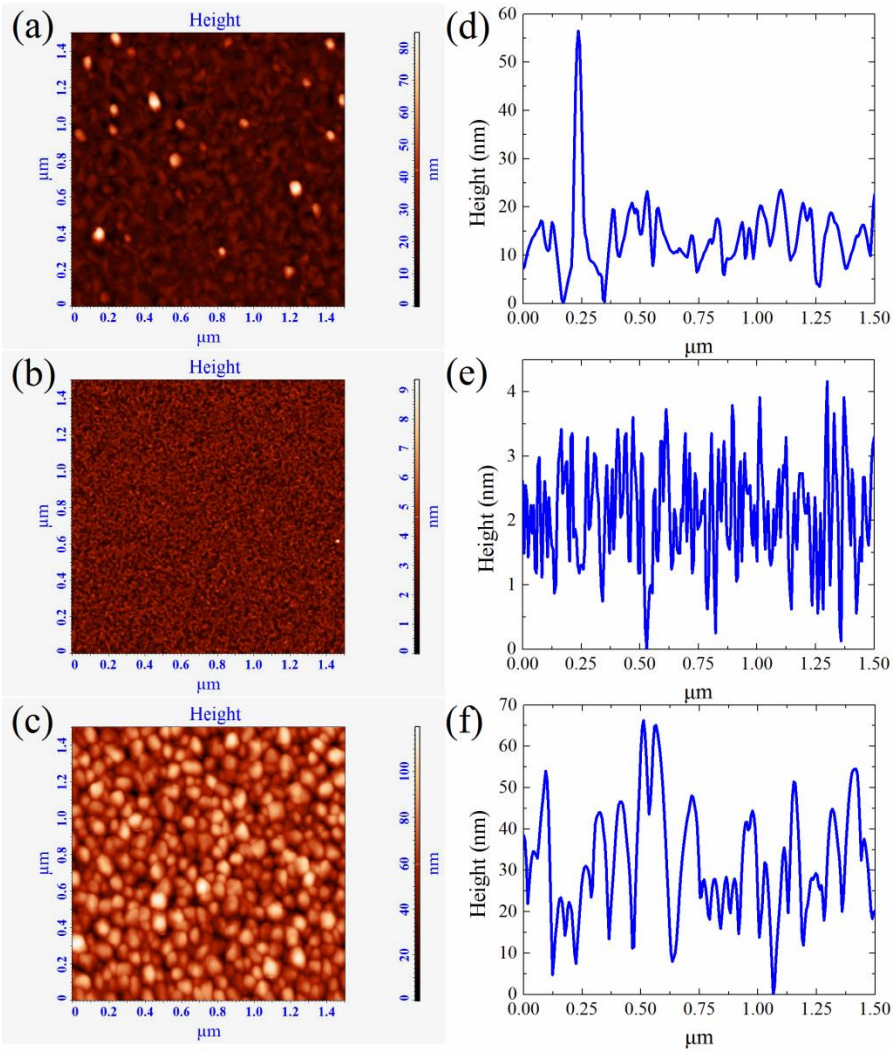

Figure 47. *AFM scans for (a) Bi_2Te_3 reference sample, (b) Nb reference sample and (c) Nb/Bi_2Te_3/Nb trilayer sample. (d), (e) and (f) are the corresponding last scan height profile for scans (a), (b) and (c), respectively.*

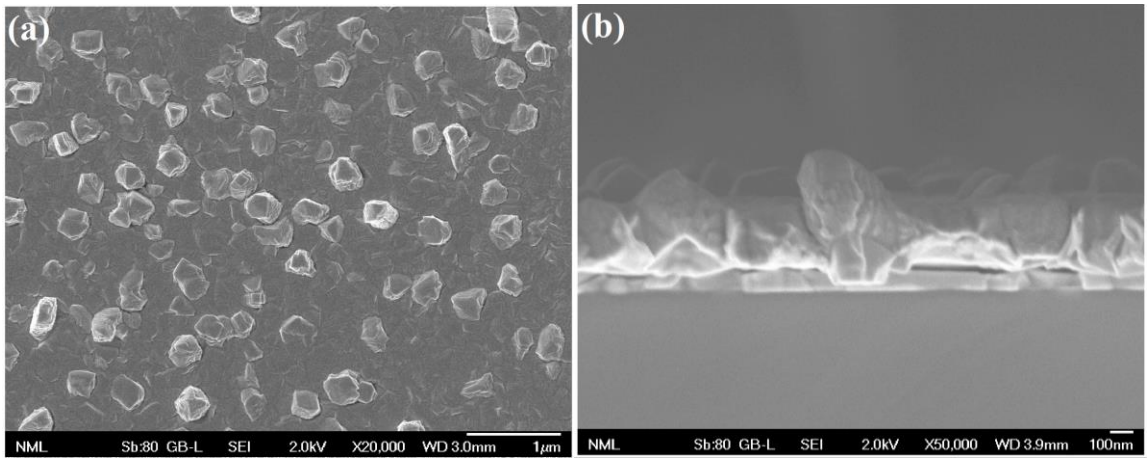

Figure 48. *FESEM images for Bi_2Te_3/Nb bilayer in (a) top-view and (b) 90-degree rotation.*

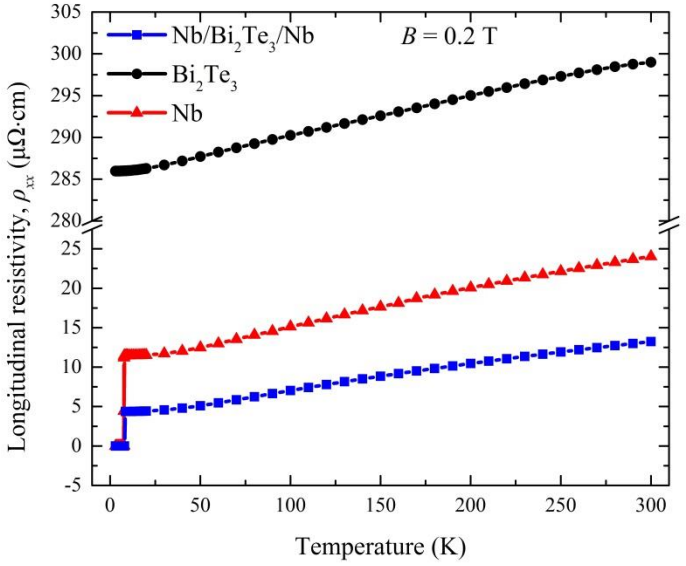

Figure 49. *Temperature dependence of longitudinal resistivity for trilayer and reference samples.*

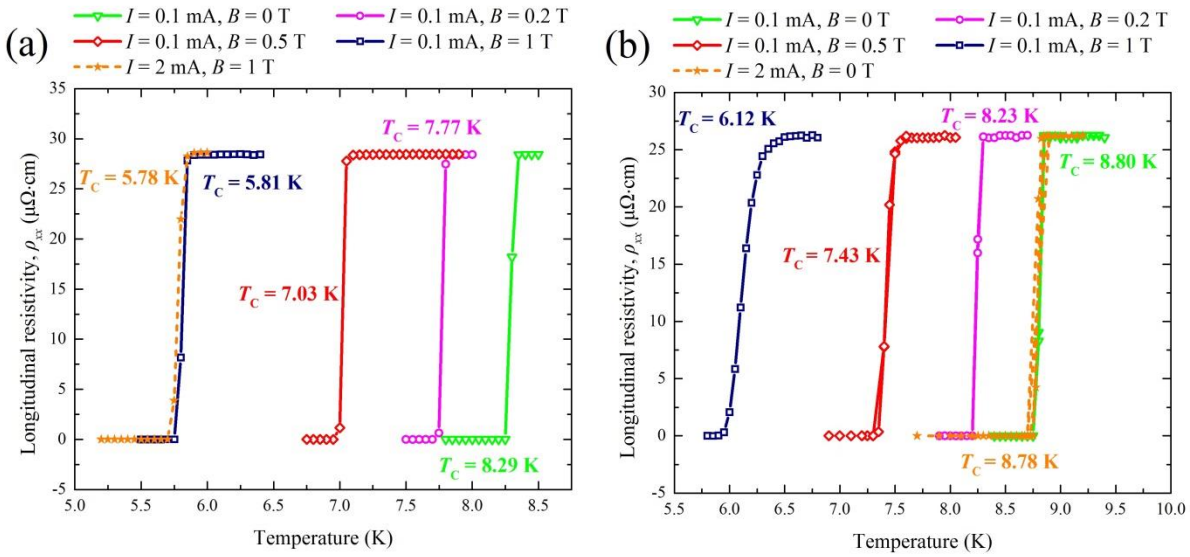

Figure 50. *Temperature dependence of longitudinal resistivity for the estimation of the critical temperature, T_C, for Nb reference (a) and trilayer (b) samples.*

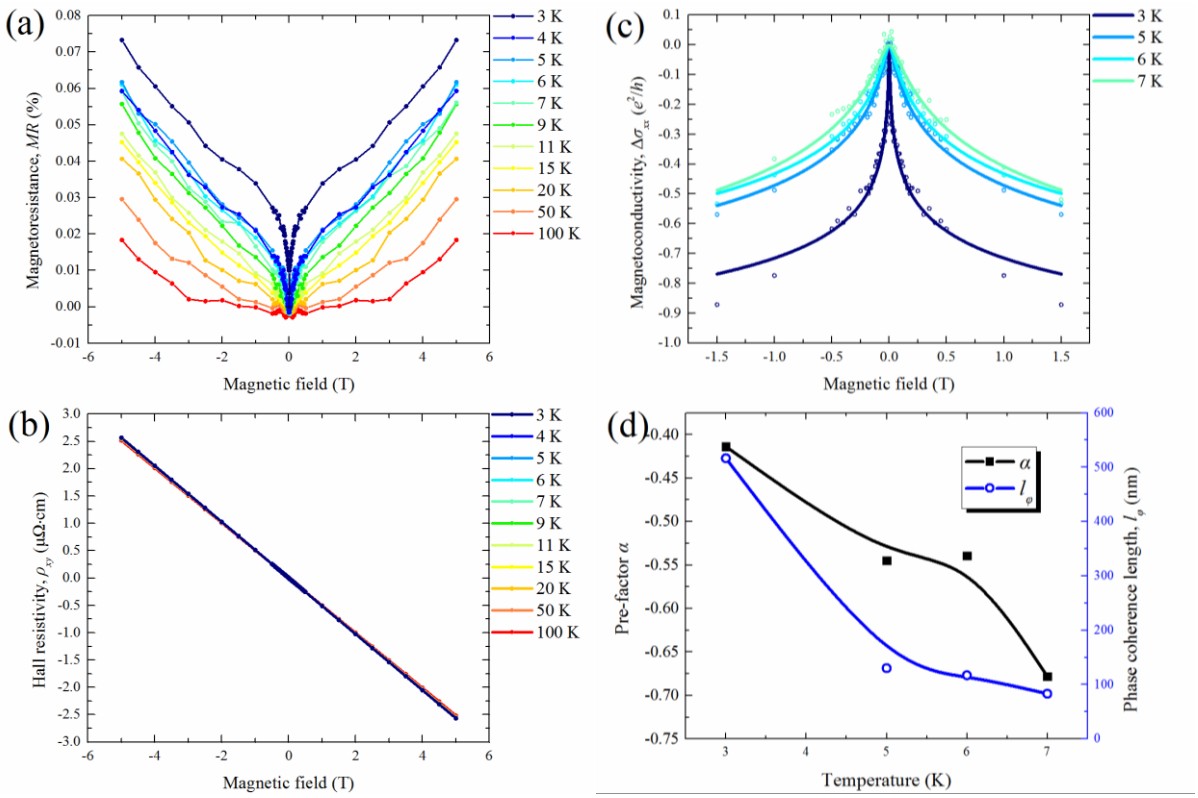

Figure 51. *Magnetotransport characterization for Bi_2Te_3(40 nm) film. (a) Magnetoresistance, (b) Hall resistivity, (c) HLN fitting to magnetoconductivity and (d) HLN fitting parameters.*

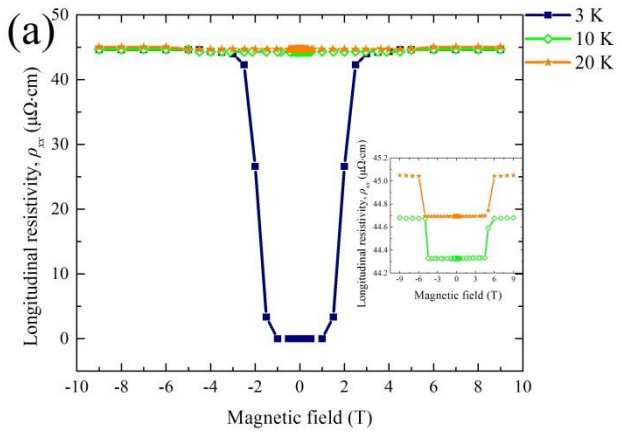

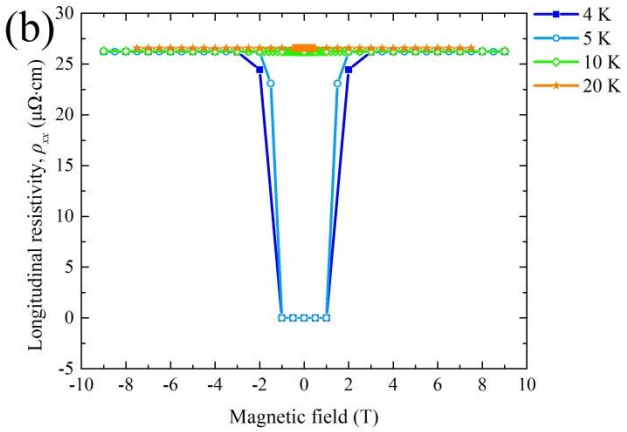

Figure 52. *Longitudinal resistivity, ρ_{xx}, of (a) Bi_2Te_3(100 nm)/Nb(100 nm) bilayer and (b) Nb(100 nm)/Bi_2Te_3(40 nm)/Nb(100 nm) trilayer samples.*

Preliminary data on other systems that were studied

Structural and magnetotransport characterization of V doped Bi_2Te_3 thin films

A series of $(Bi_{1-x}V_x)_2Te_3$ (x= 0.12, 0.15, 0.21 atomic percent) films were prepared with magnetron sputtering on Si(111) substrates with substrate's temperature fixed at 300 ^oC. The doping was achieved by a ten times repetition of Bi_2Te_3/V bilayer pattern. The samples were prepared as Hall-bar shaped devices using a Hall stencil mask and second stencil masks to make pads by Cr/Au magnetron sputtering deposition.

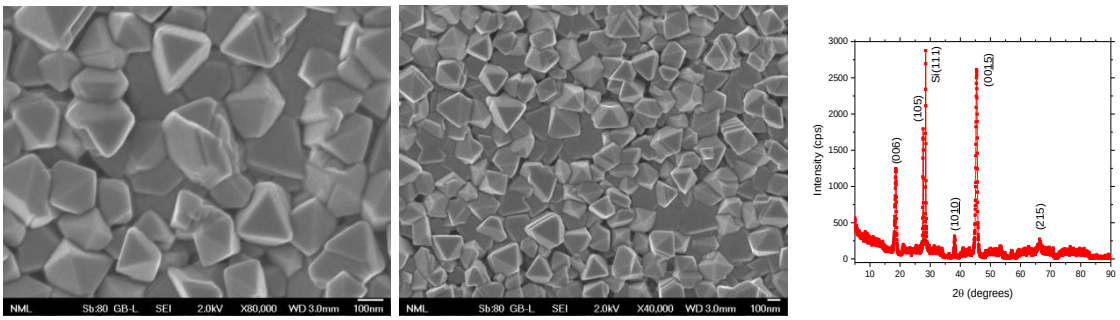

Figure 53. *FESEM images and XRD for Si(111)/$(Bi_{0.88}V_{0.12})_2Te_3$ sample.*

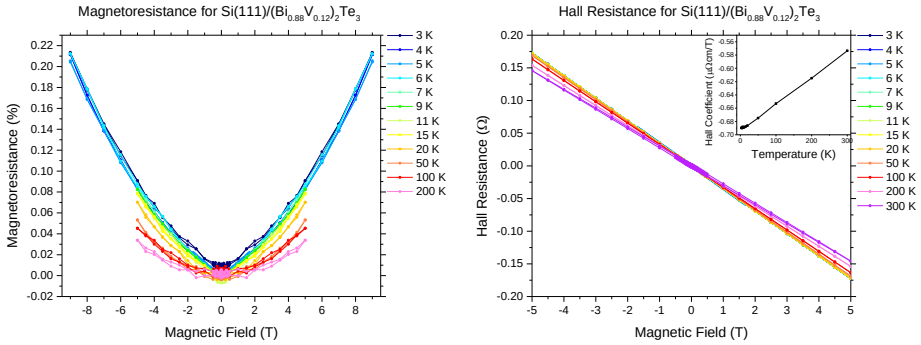

Figure 54. *Magnetoresistance and Hall resistance for Si(111)/$(Bi_{0.88}V_{0.12})_2Te_3$ sample.*

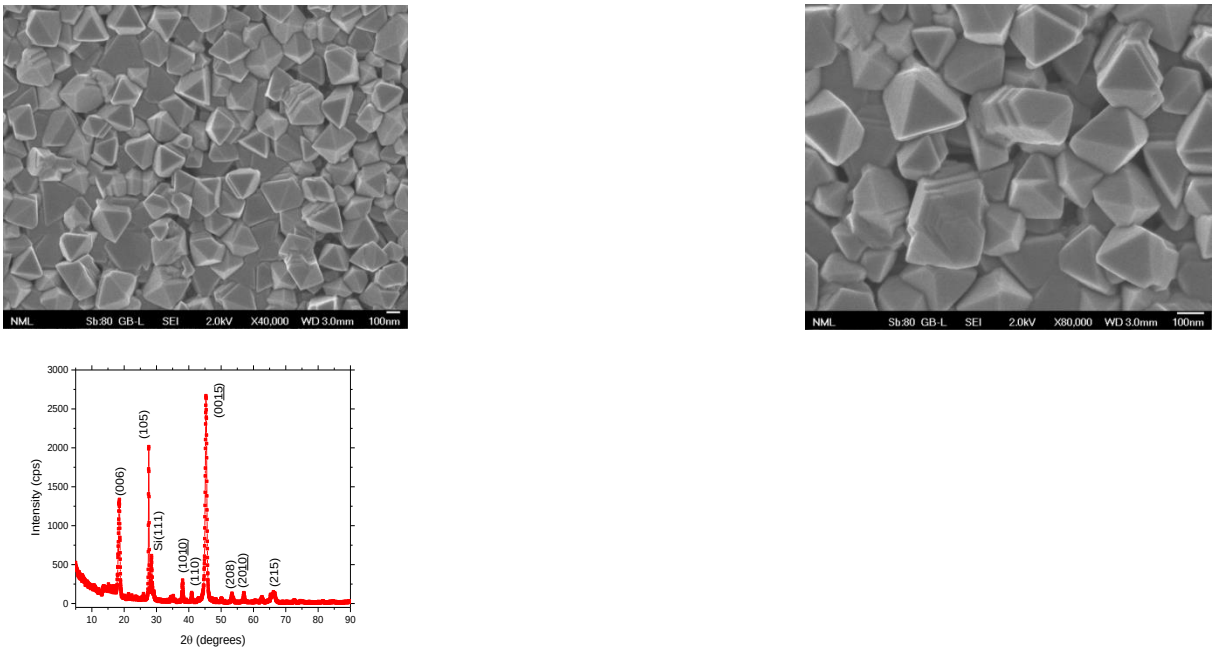

Figure 55. *FESEM images and XRD for Si(111)/$(Bi_{0.85}V_{0.15})_2Te_3$ sample.*

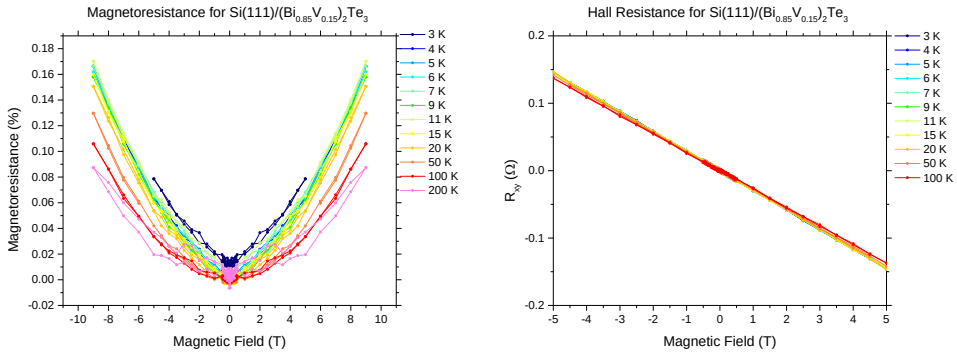

Figure 56. *Magnetoresistance and Hall resistance for Si(111)/$(Bi_{0.85}V_{0.15})_2Te_3$ sample.*

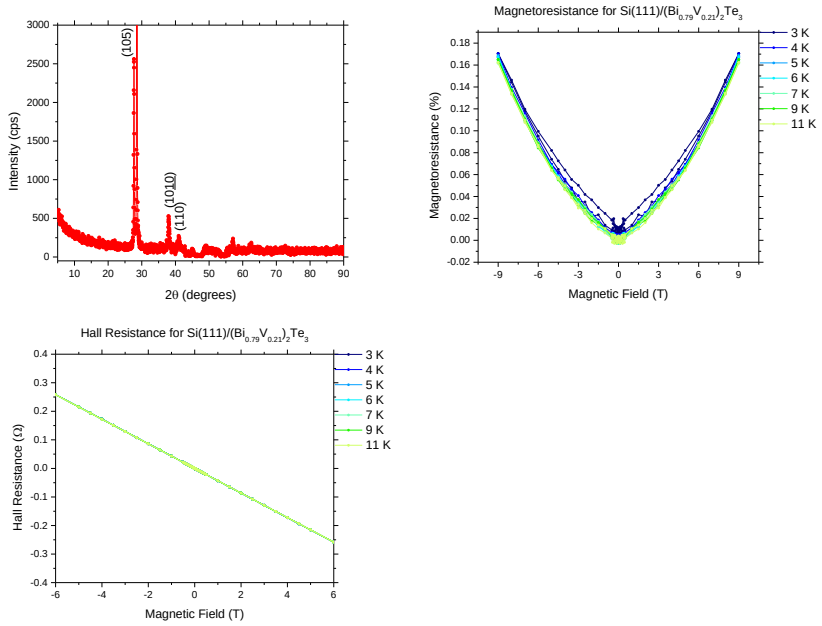

Figure 57. *XRD pattern, magnetoresistance and Hall resistance for Si(111)/$(Bi_{0.79}V_{0.21})_2Te_3$ sample*

Structural and magnetotransport characterization of highly doped Co Bi_2Te_3 thin films

A series of $(Bi_{1-x}Co_x)_2Te_3$ (x= 0.3, 0.4, 0.8 atomic percent) films were prepared with magnetron sputtering on Si(111) substrates with substrate's temperature fixed at 300 ^oC. The doping was achieved by a ten times repetition of Bi_2Te_3/Co bilayer pattern. The samples were prepared as Hall-bar shaped devices using a Hall stencil mask and second stencil masks to make pads by Cr/Au magnetron sputtering deposition.

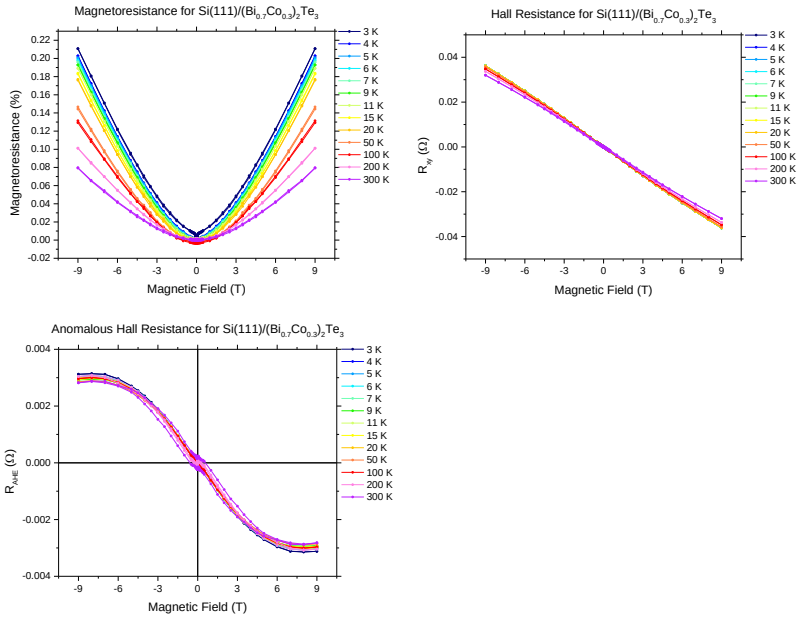

Figure 58. *Magnetotransport measurements for Si(111)/$(Bi_{0.7}Co_{0.3})_2Te_3$*

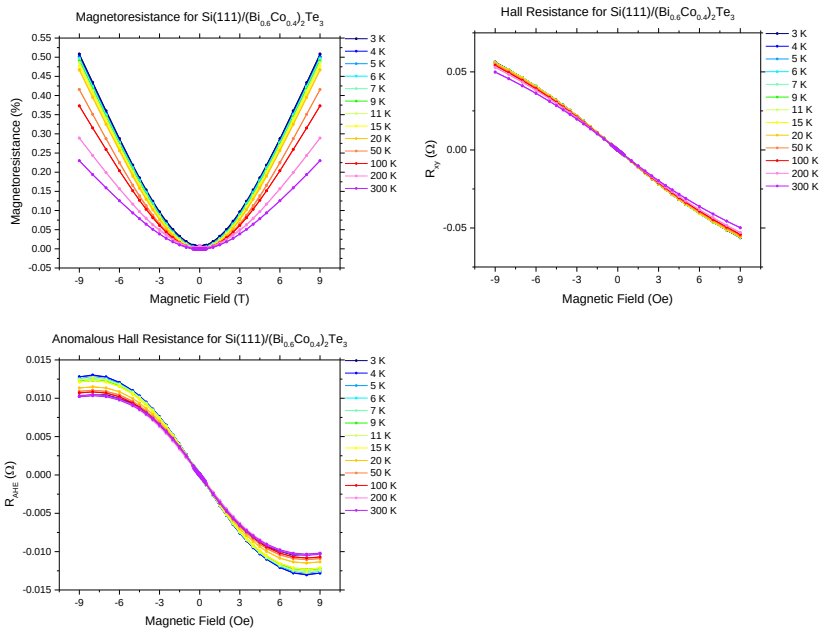

Figure 59. *Magnetotransport measurements for Si(111)/$(Bi_{0.6}Co_{0.4})_2Te_3$*

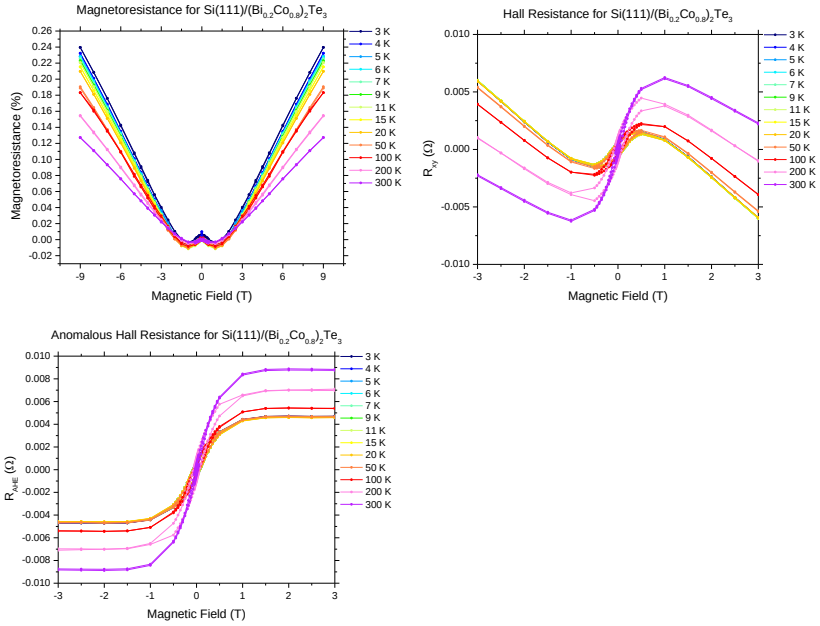

Figure 60. *Magnetotransport measurements for Si(111)/($Bi_{0.2}Co_{0.8}$)$_2Te_3$*

Structural and magnetotransport characterization of Sm doped Bi_2Te_3 thin films

A series of $(Bi_{1-x}Sm_x)_2Te_3$ (x=0, 0.02, 0.03, 0.05, 0.1, atomic percent) films were prepared with magnetron sputtering on Si(111) substrates with substrate's temperature fixed at 300 ^oC. The doping was achieved by a five times repetition of Bi_2Te_3/Sm bilayer pattern. Sm concentration was controlled by appropriate variation of the Sm layer thickness while the Bi_2Te_3 layer was 40nm thick.

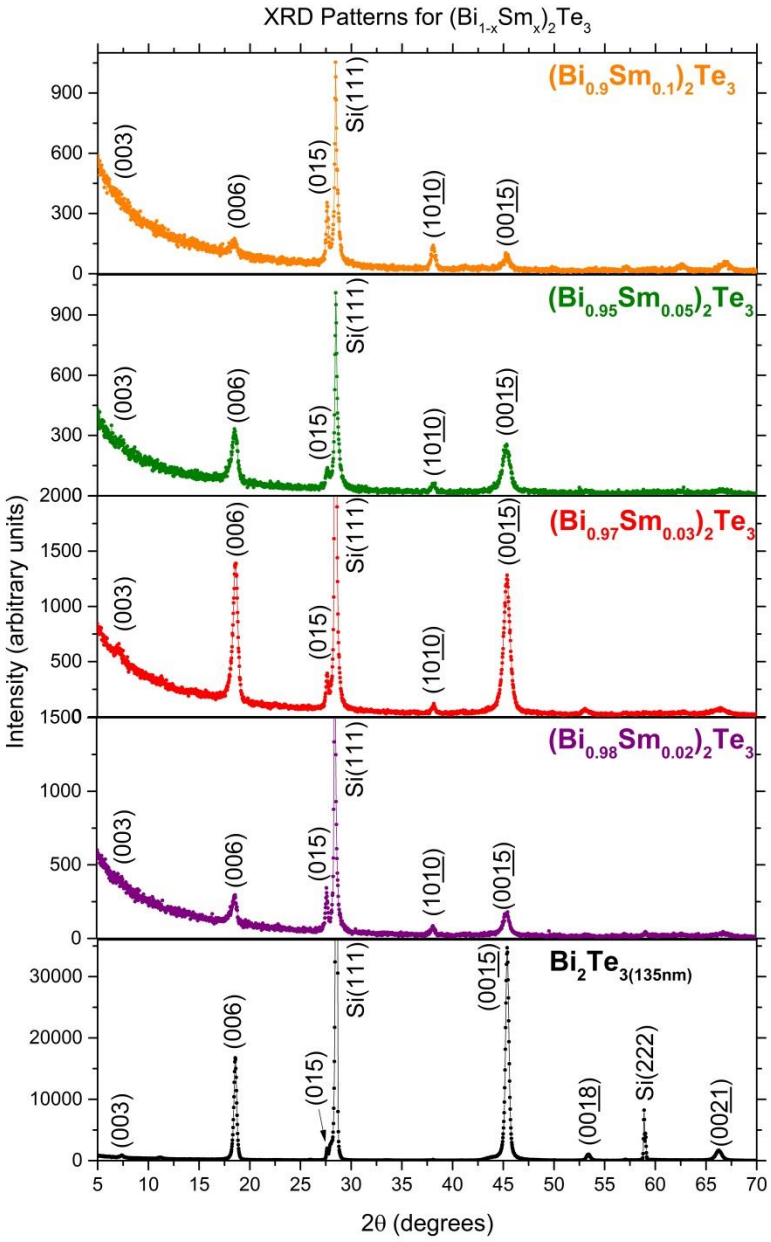

Figure 61. *XRD patterns for $(Bi_{1-x}Sm_x)_2Te_3$ thin films and a reference sample of Bi_2Te_3.*

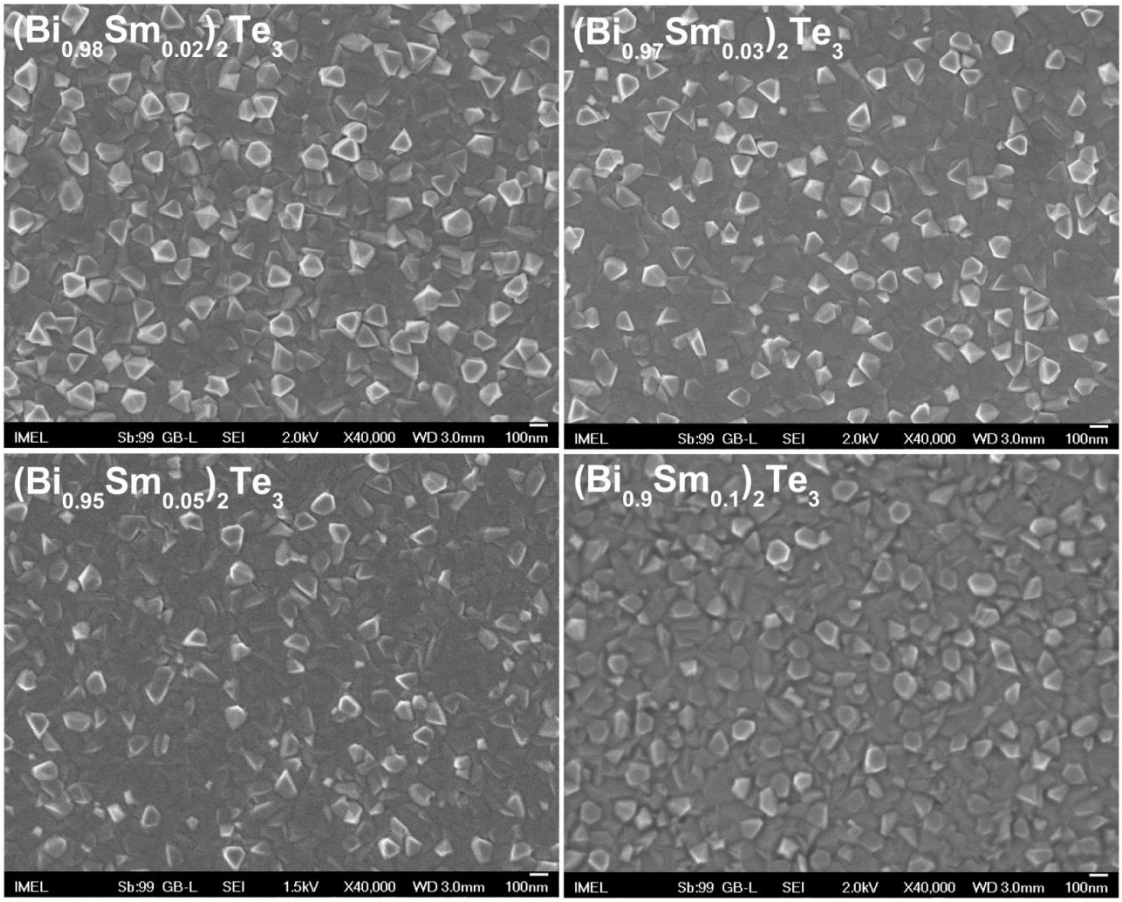

Figure 62. *FESEM scans of $(Bi_{1-x}Sm_x)_2Te_3$ thin films*

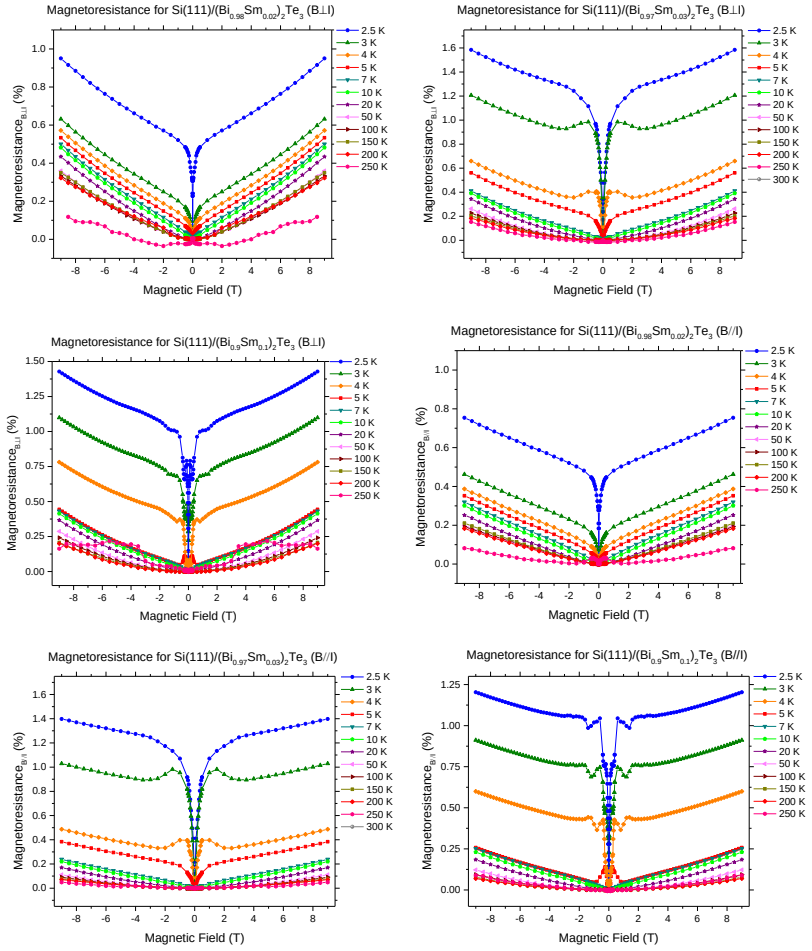

Figure 63. *Perpendicular and parallel MR measurements for $(Bi_{1-x}Sm_x)_2Te_3$ thin films*

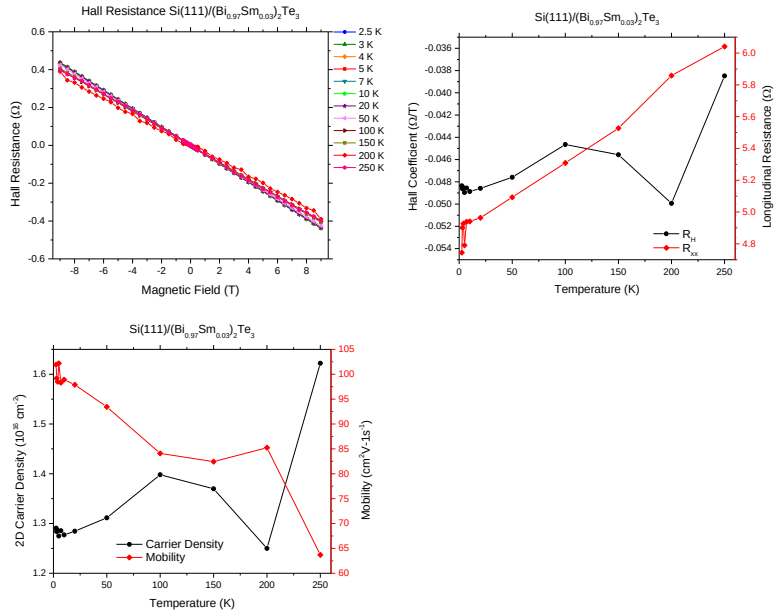

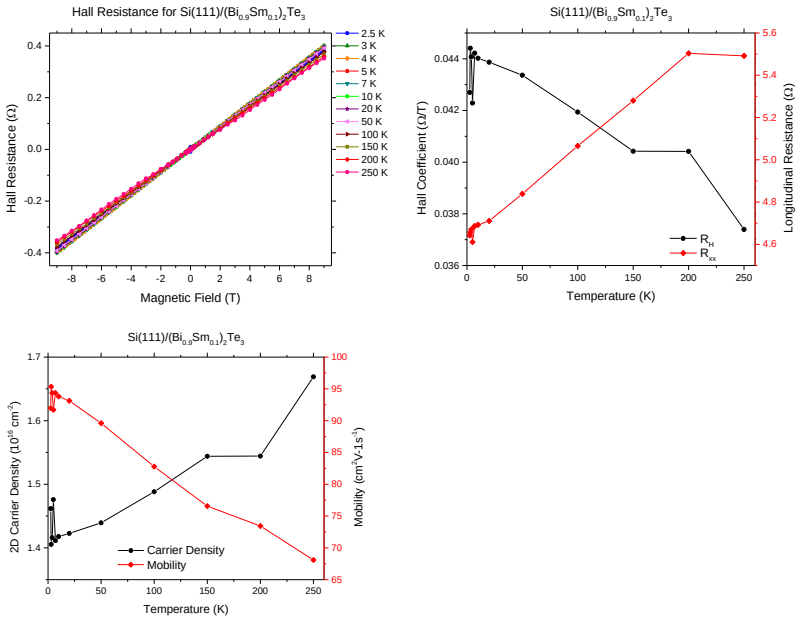

Figure 64. *Hall resistance measurements and magnetotransport properties for $(Bi_{1-x}Sm_x)_2Te_3$ thin films*

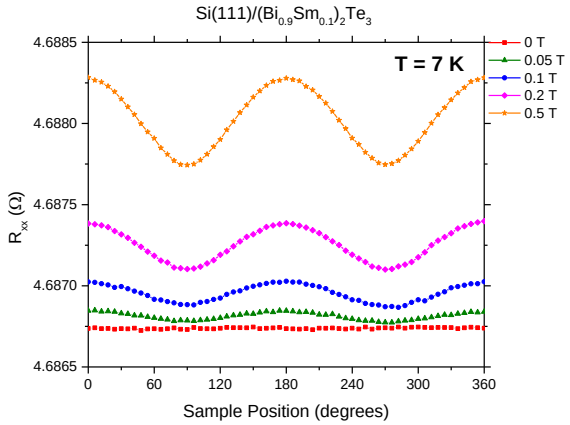

Figure 65. *Longitudinal resistance versus rotation angle for the thin film $(Bi_{0.9}Sm_{0.1})_2Te_3$ at 7 K.*

Structural and magnetotransport characterization of $Bi_{1-x}Sb_x$ thin films

A series of $Bi_{1-x}Sb_x$ (x=0, 0.1, 0.2, 0.3, 0.5, 1, atomic percent) films were prepared with magnetron sputtering on Si(111) substrates. After the deposition films were annealed for 30 min at 80 ºC in order to reduce the surface roughness due to bismuth coarsening during deposition.

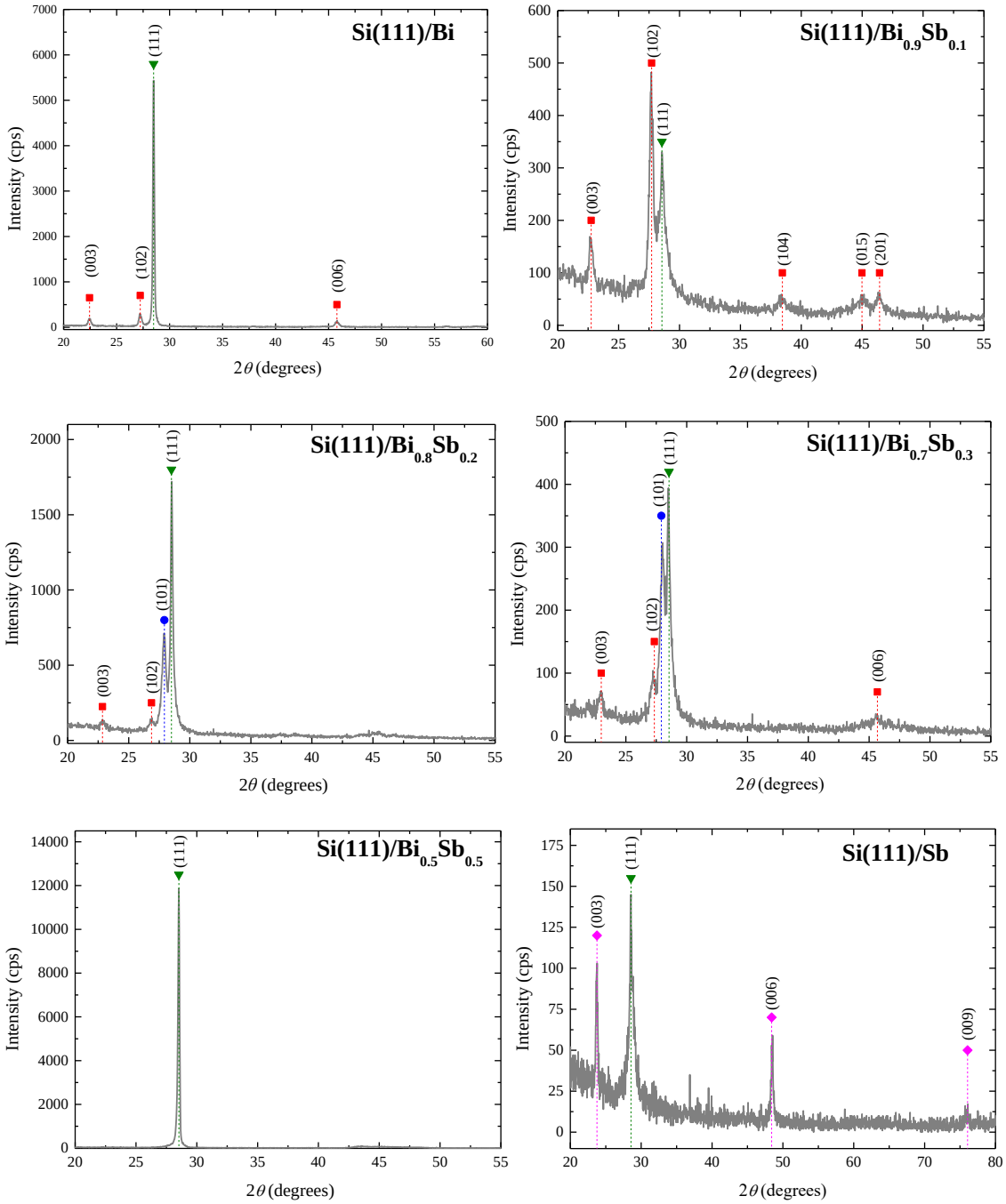

Figure 66. *XRD patterns of $Bi_{1-x}Sb_x$ thin films. The (■) peaks refer to rhombohedral Bi structure, the (●) peaks to the rhombohedral Sb structure, the (◆) peaks to the hexagonal Sb structure and the (▼) peak refers to the Si(111) peak of the substrate.*

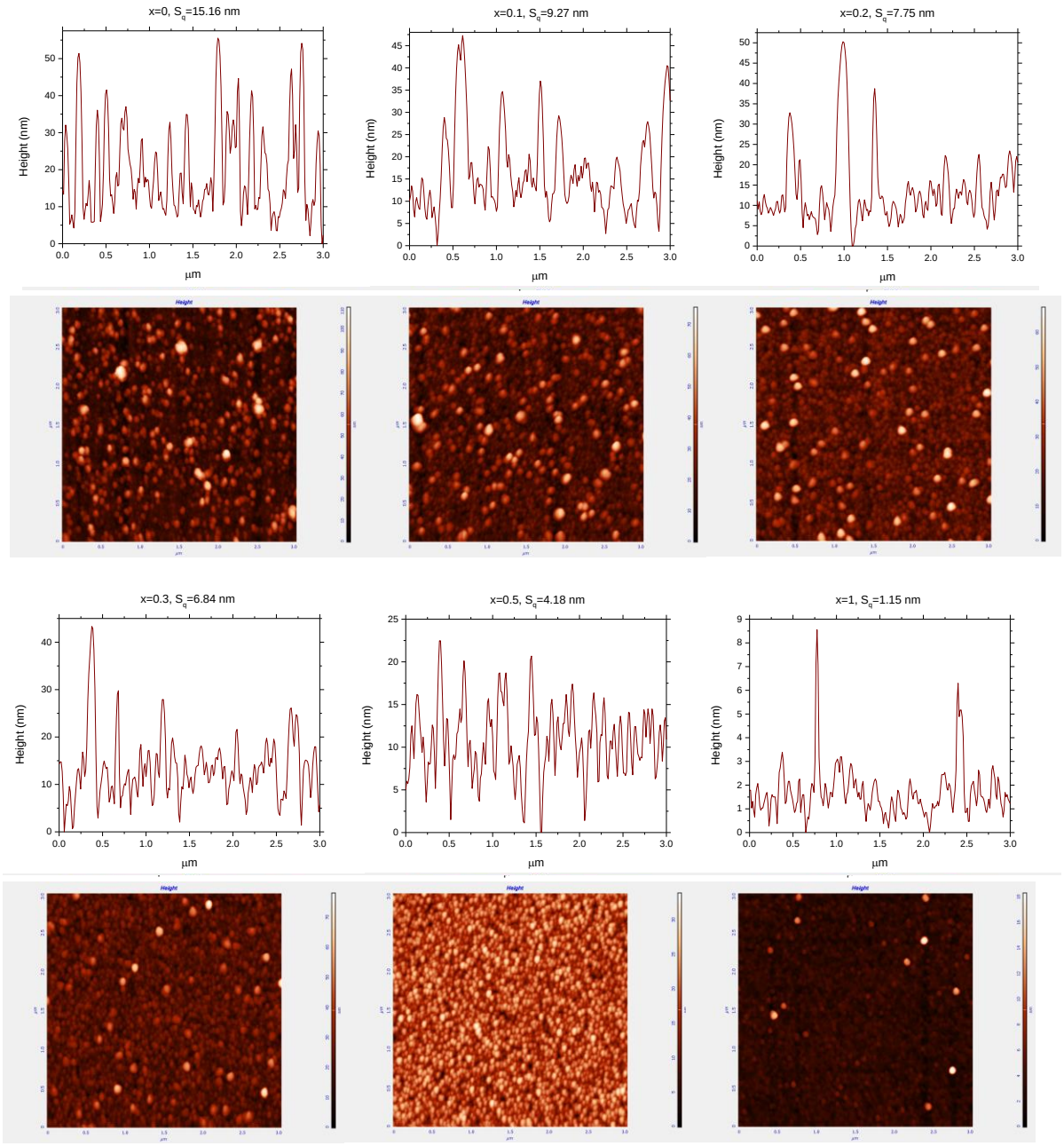

Figure 67. *AFM scans along with the last scan height profile of $Bi_{1-x}Sb_x$ thin films.*

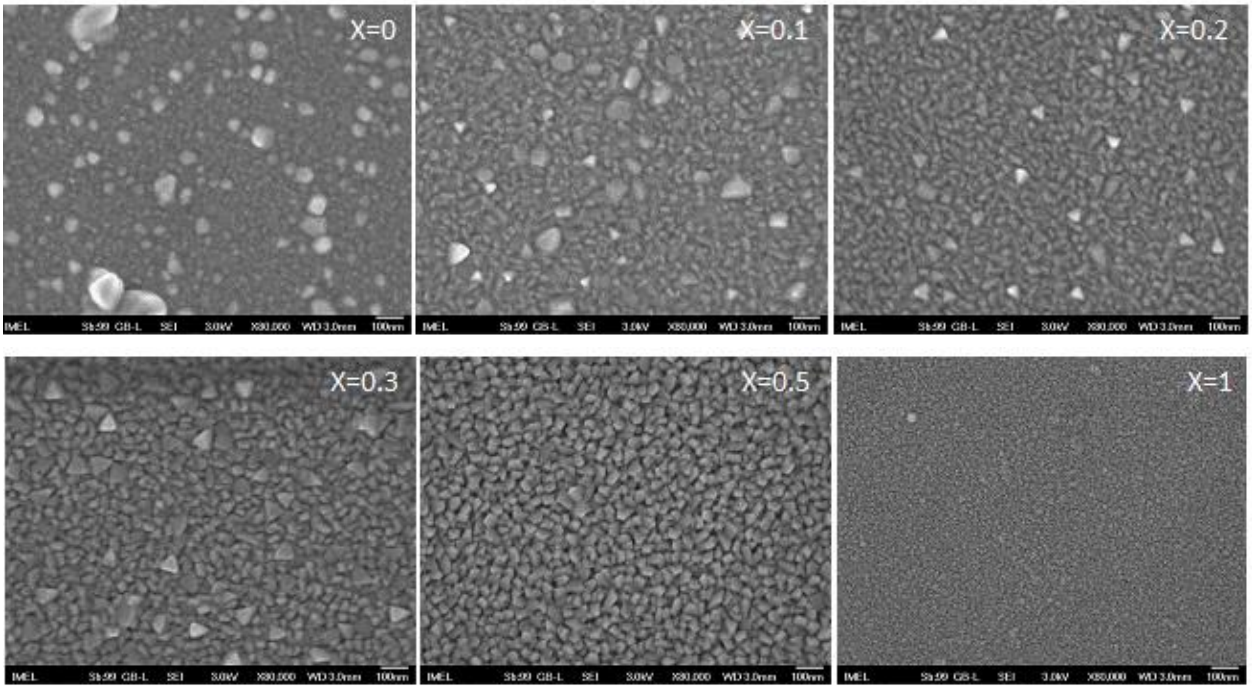

Figure 68. *FESEM scan of $Bi_{1-x}Sb_x$ thin films.*

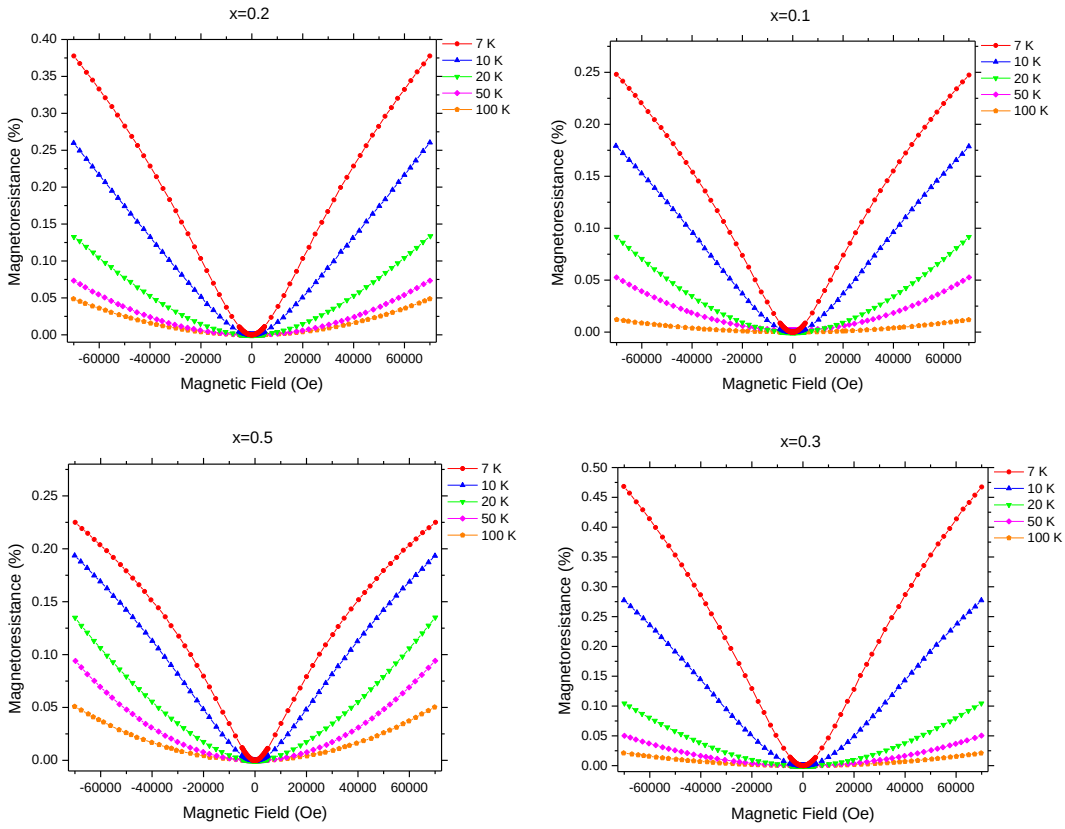

Figure 69. *MR measurements for $Bi_{1-x}Sb_x$ thin films.*

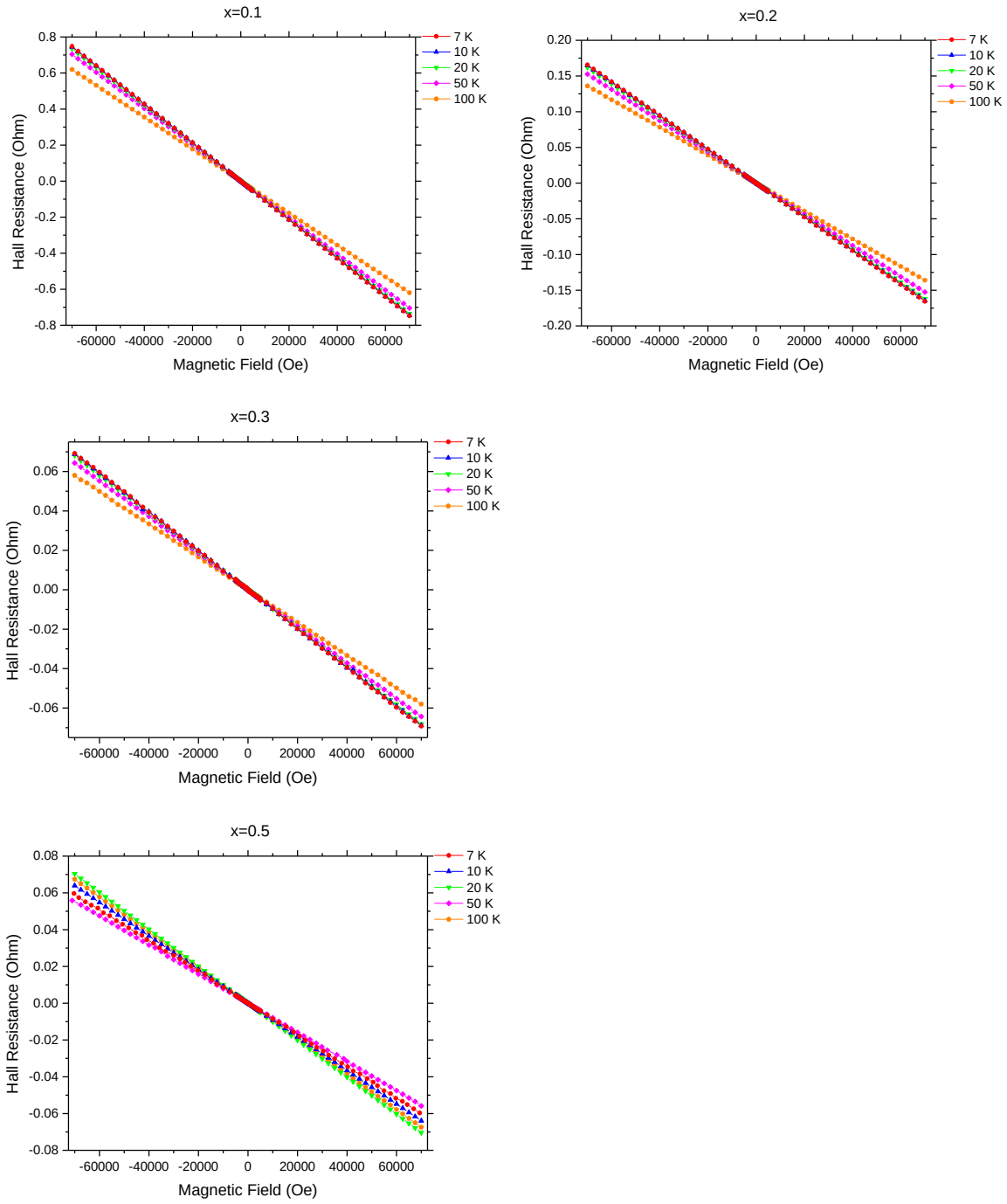

Figure 70. *Hall resistance measurements for $Bi_{1-x}Sb_x$ thin films.*

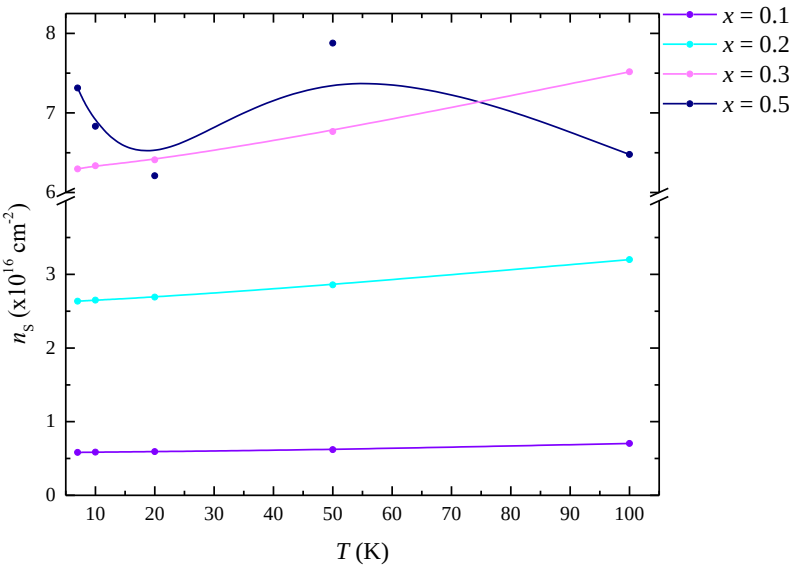

Figure 71. *Variation of the surface carrier (electrons) density with temperature for thin films of $Bi_{1-x}Sb_x$, with x = 0.1, 0.2, 0.3 and 0.5.*

Structural and magnetotransport characterization of Bi thin films grown on kapton substrates at different temperatures

A series of bismuth film were grown on kapton substrates with substrate temperature varying from room temperature to 271 ºC (melting point of bismuth). All samples had thickness of 50 nm.

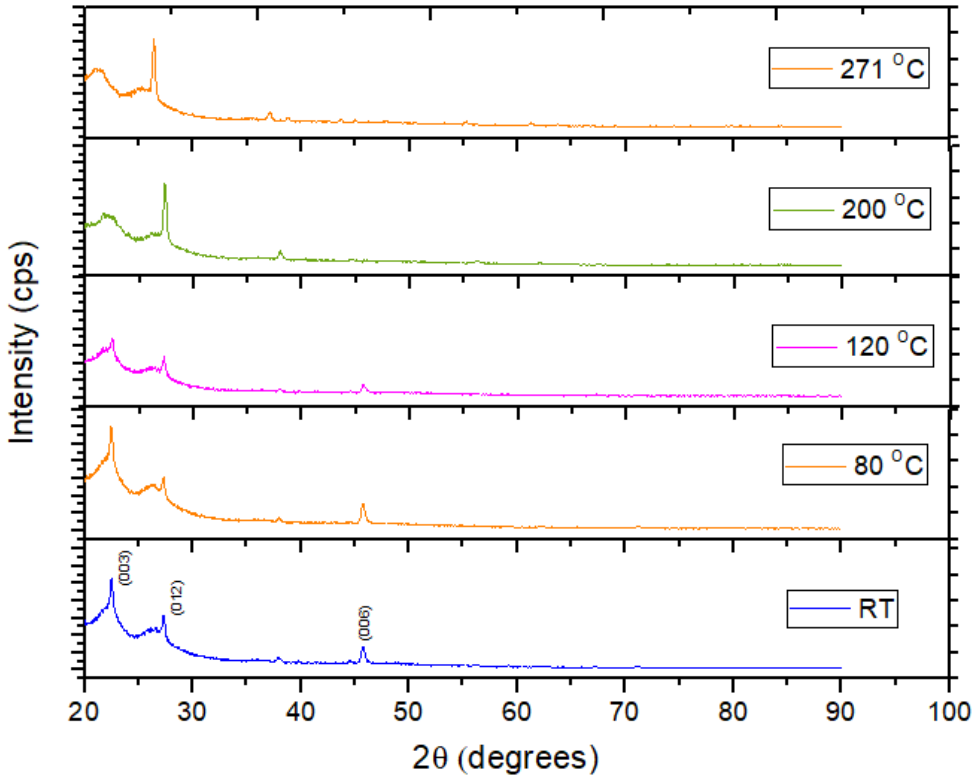

Figure 72. *XRD patterns for Bi thin films of 50 nm nominal thickness grown on kapton substrates at different temperatures.*

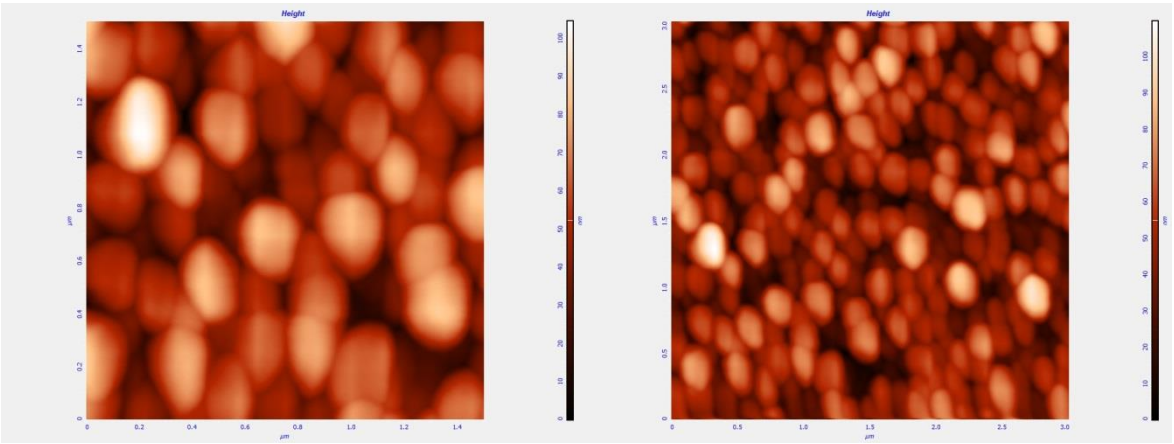

Figure 73. *AFM pictures of a Bi film (1.5 μm, 3μm) deposited at 271 °C*

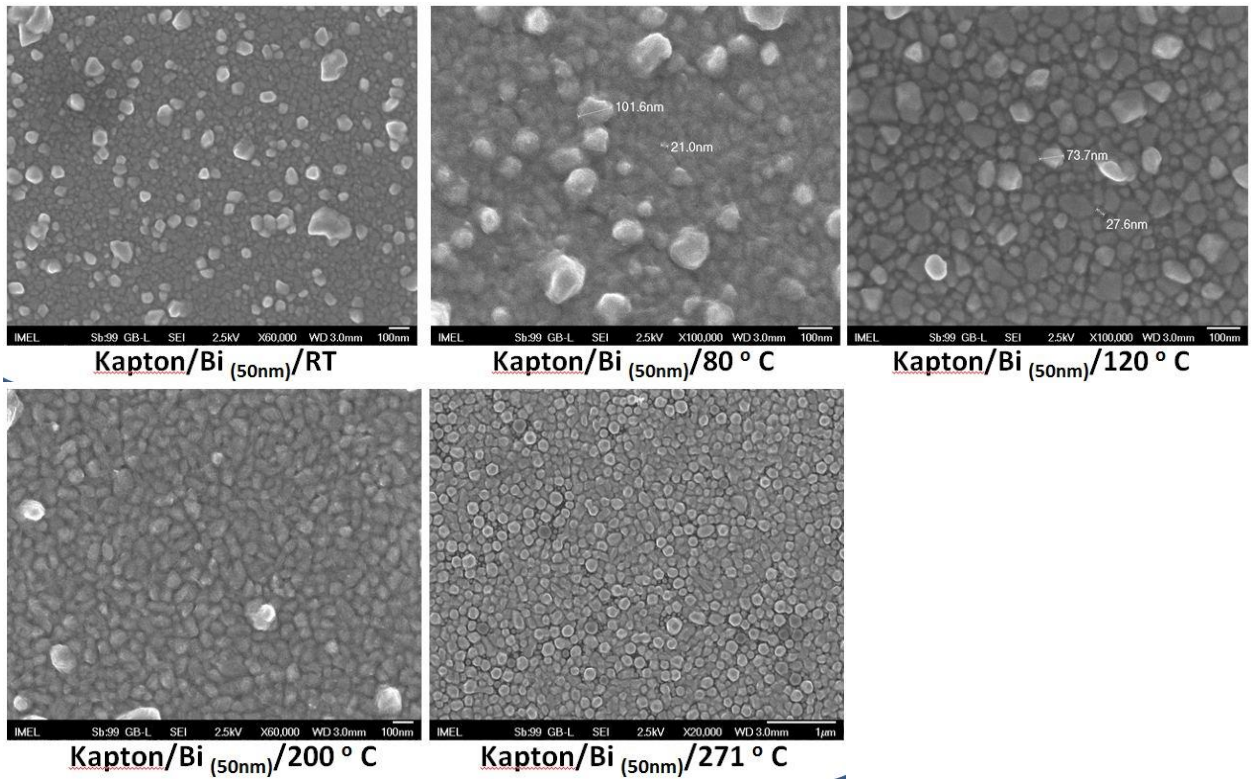

Figure 74. *FESEM scans for Bi thin films of 50 nm nominal thickness grown on kapton substrates.*

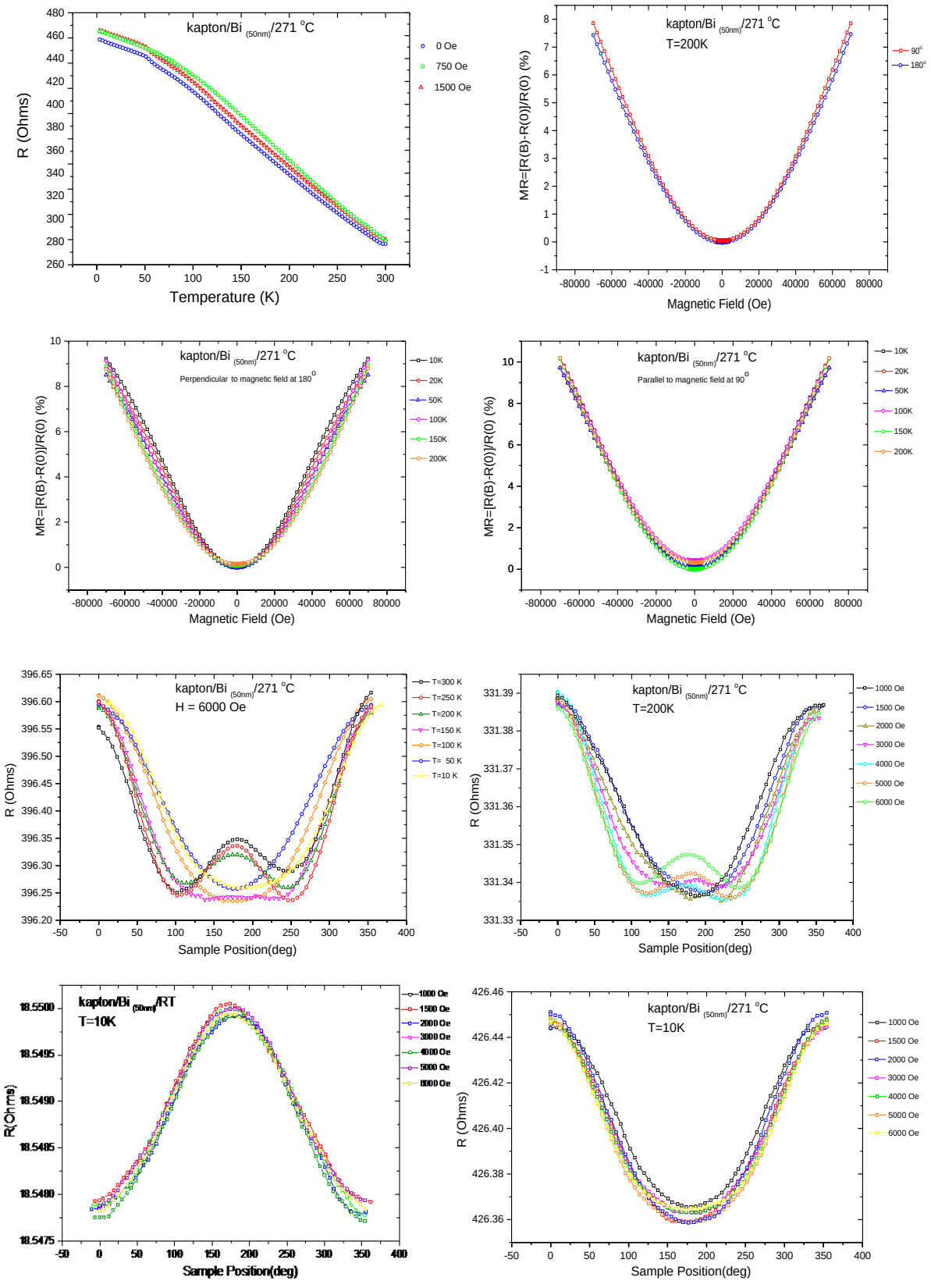

Figure 75. *Various magnetrotransport measurements of Bi thin films grown on kapton substrates.*

Structural and magnetotransport characterization of $Bi_{1-x}Mn_x$ thin films

A series of bismuth-manganese film were grown on $SrTiO_3$ substrates with substrate temperature at 80 ^oC. The films were grown by repetition of Bi/Mn bilayer ten times.

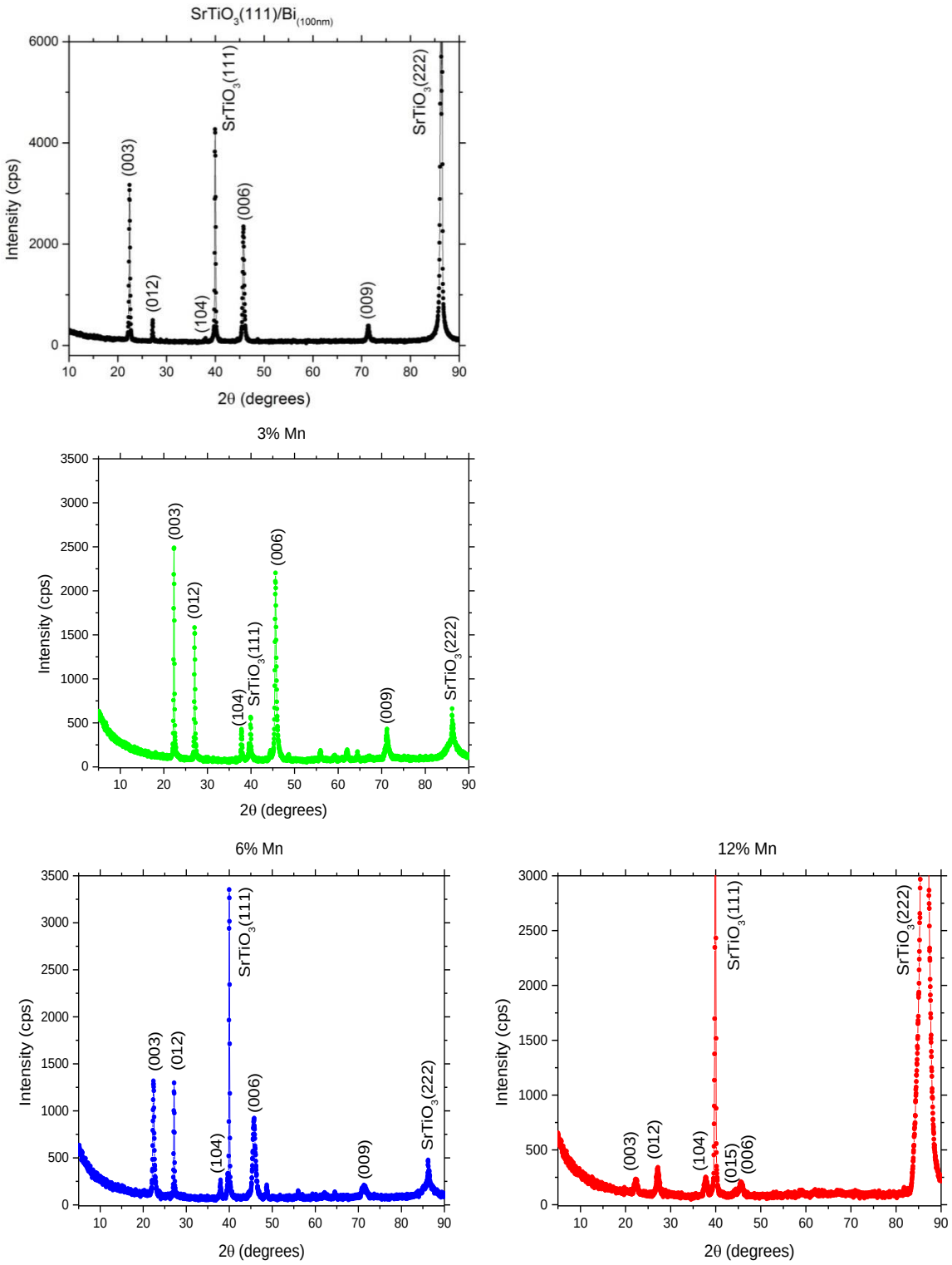

Figure 76. *XRD patterns for $SrTiO_3/B_{1-x}Mn_x$ thin films.*

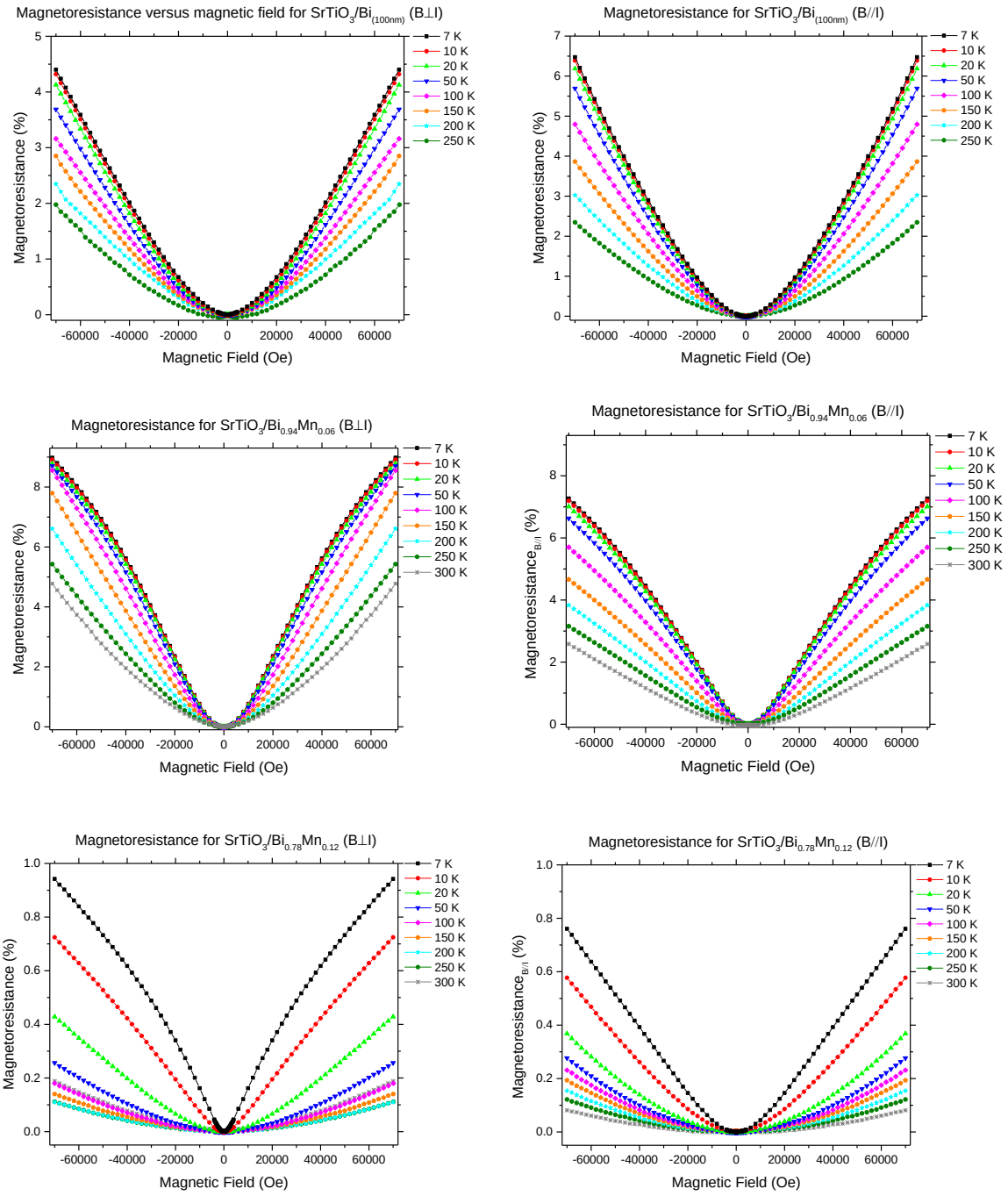

Figure 77. *MR measurements in perpendicular (left) and parallel (right) magnetic field for thin films of $SrTiO_3/Bi_{1-x}Mn_x$, with x=0, 0.06 and 0.12.*

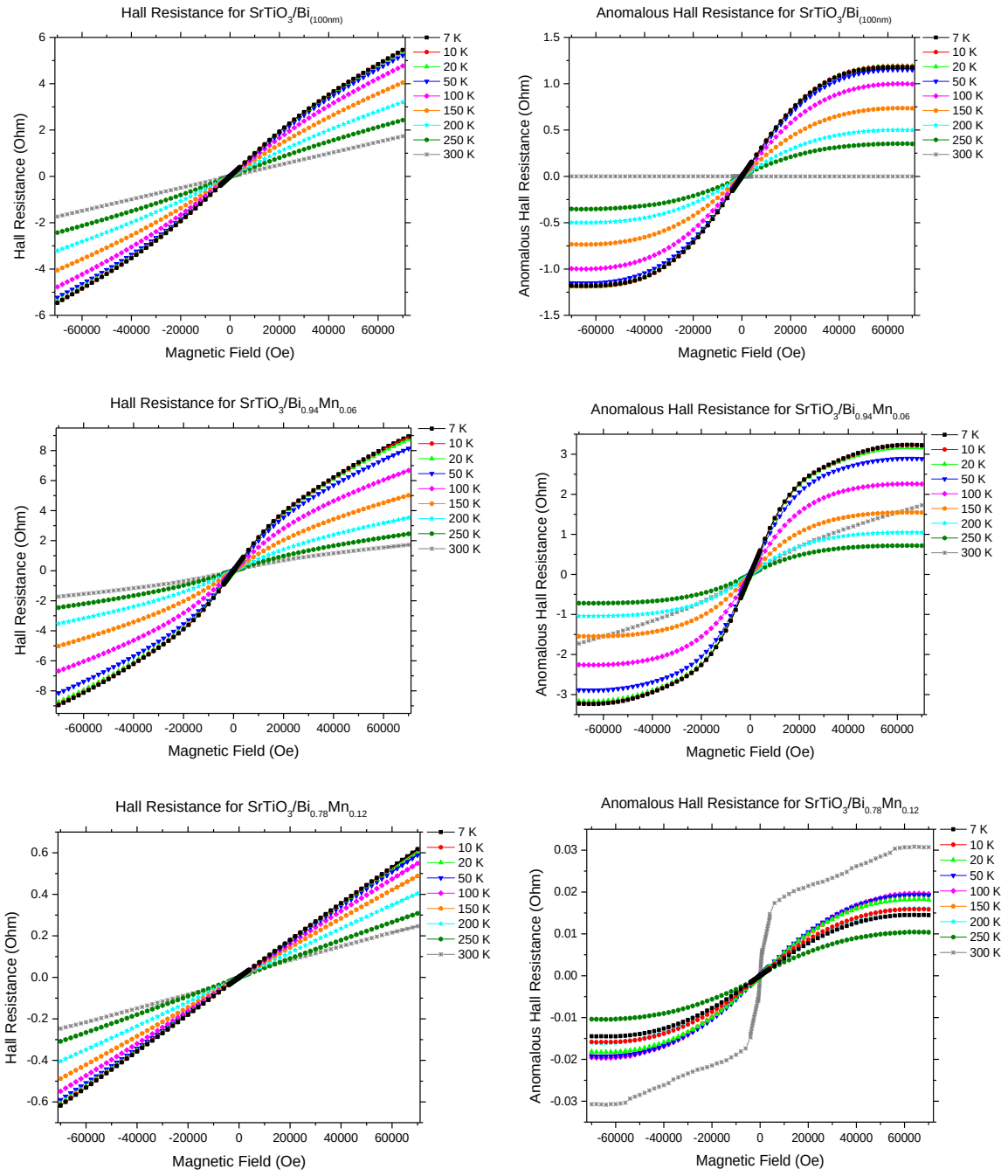

Figure 78. *Hall resistance measurements and anomalous Hall resistance contribution of $SrTiO_3/Bi_{1-x}Mn_x$ thin films, with x=0, 0.6 and 0.12.*

Villari Magnetomechanical Coupling at hcp Cobalt Thin Films on Flexible Substrates

In this work, the structural and magnetic behavior of Cobalt (Co) thin films deposited on flexible Kapton substrates by means of magnetron sputtering technique at ambient temperature are investigated. In order to reveal the impact of Co structure, the case of as-deposited and buffer-layered Co films are studied. The structural characterization was carried out by X-ray diffraction showing the HCP structure of Co. Scanning electron microscopy was conducted to reveal the morphological characteristics of the samples. The magnetic characterization has been performed by means of vibrating sample magnetometry at ambient conditions. Both systems of Co films were subjected in a wide range of applied strains using a newly constructed sample holder in order to investigate the Villari effect. Upon the progressive increase of strain, the magnetization of Co films exhibits a non-monotonic behavior with a local maximum between 2 and 3%. This non-monotonic behavior of magnetization is ascribed to the possible interplay of two main mechanisms. The first mechanism relies on the change of the interatomic distances in the crystal structure at relatively low values of the experienced strain by Co films. The second mechanism is based on the microstructural modification of Co grains as strain exceeds a certain value.

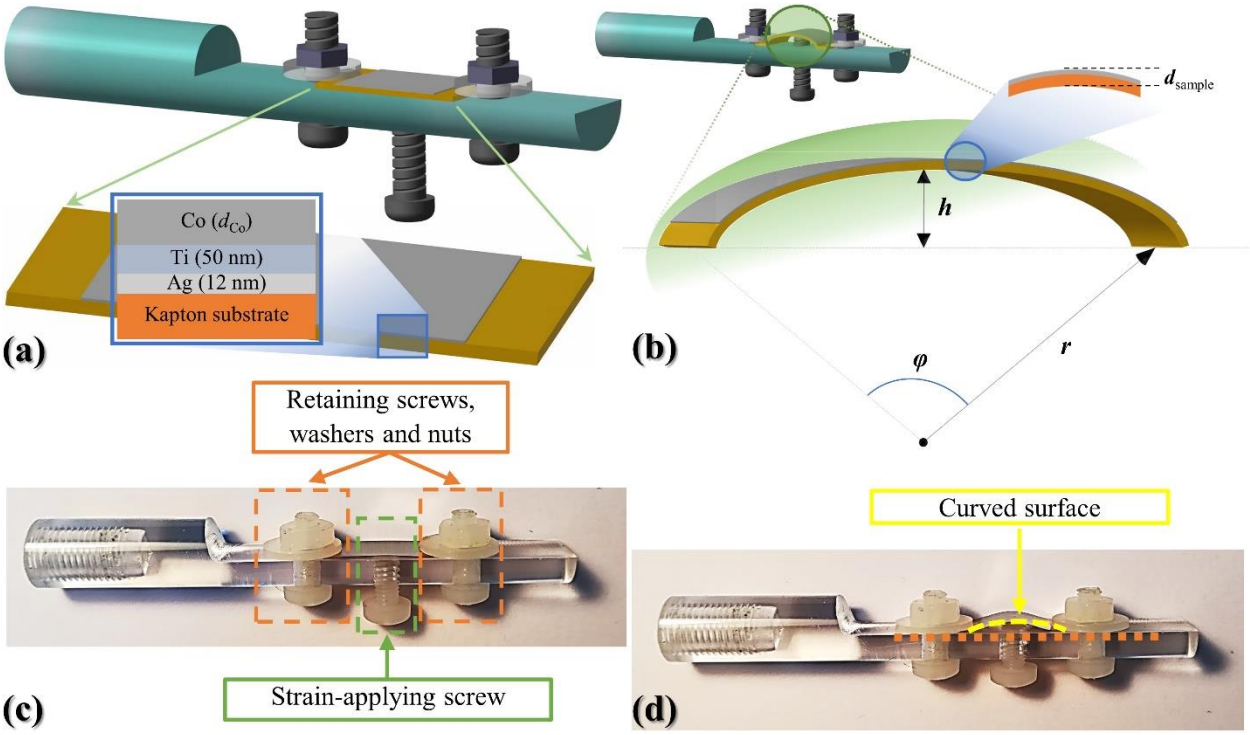

Figure 79. *Configuration of the flexible sample and the VSM holder. (a) Schematic representation of the multilayered film structure deposited on Kapton substrate without strain. The inset shows a schematic of the used growth sequence. (b) The sample under strain and the corresponding values for strain ε estimation. The inset shows the thickness of the whole film that is used for the computation of ε. Photographic images of the (c) unstrained film placed on the VSM holder and (d) the film under strain and emphasizing on the uniform curvature.*

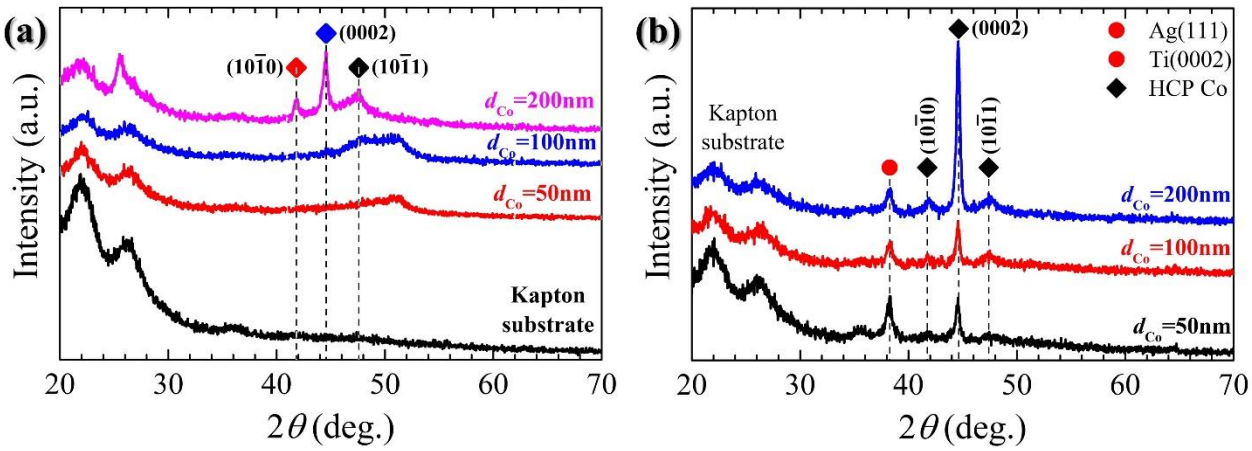

Figure 80. *XRD patterns for the (a) as-deposited Co films and (b) the buffer-layered Ag/Ti/Co films.*

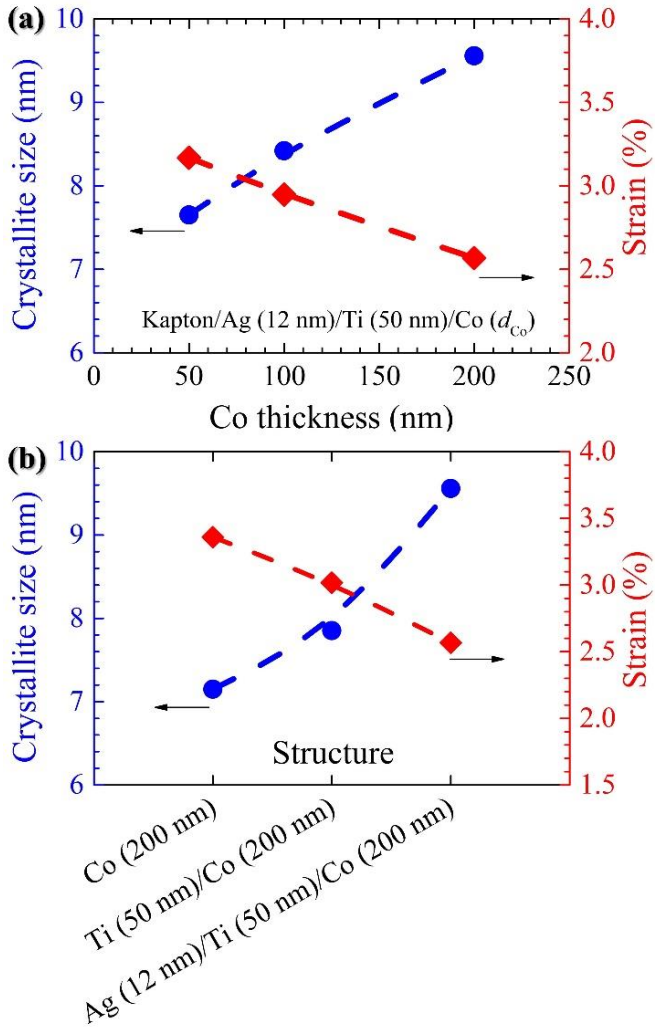

Figure 81. *(a) Evolution of the crystallite size and strain for the buffer-layered films, (b) comparison of the evolution of the crystallite size and strain for different structures of the same Co thickness, namely 200 nm.*

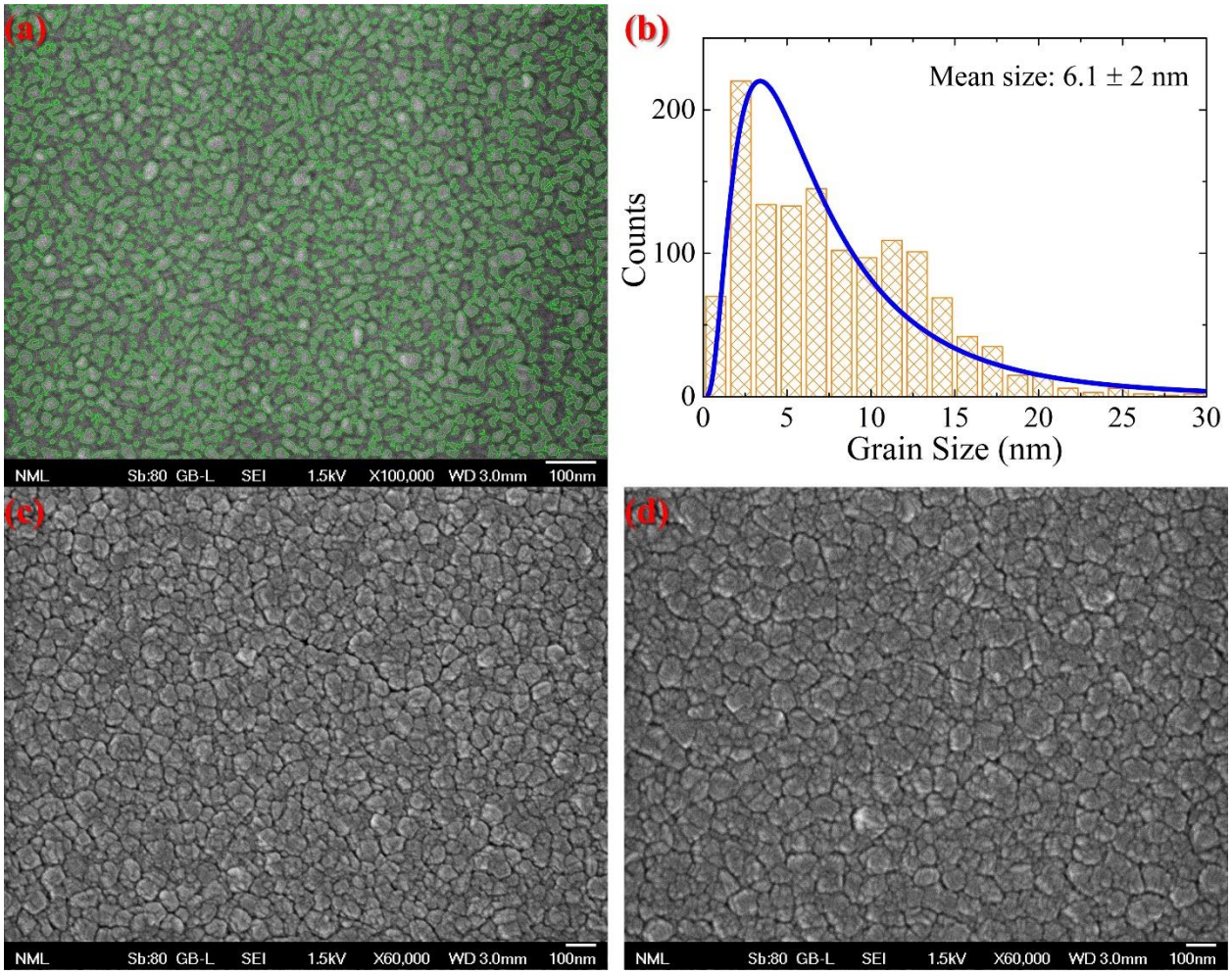

Figure 82. *(a) Surface morphology and (b) grain size distribution of the as-deposited Kapton/Co (200 nm). Surface morphology of the (c) Kapton/Ag (12 nm)/Ti (50 nm)/Co (100 nm) and (d) Kapton/Ag (12 nm)/Ti (50 nm)/Co (200 nm) films.*

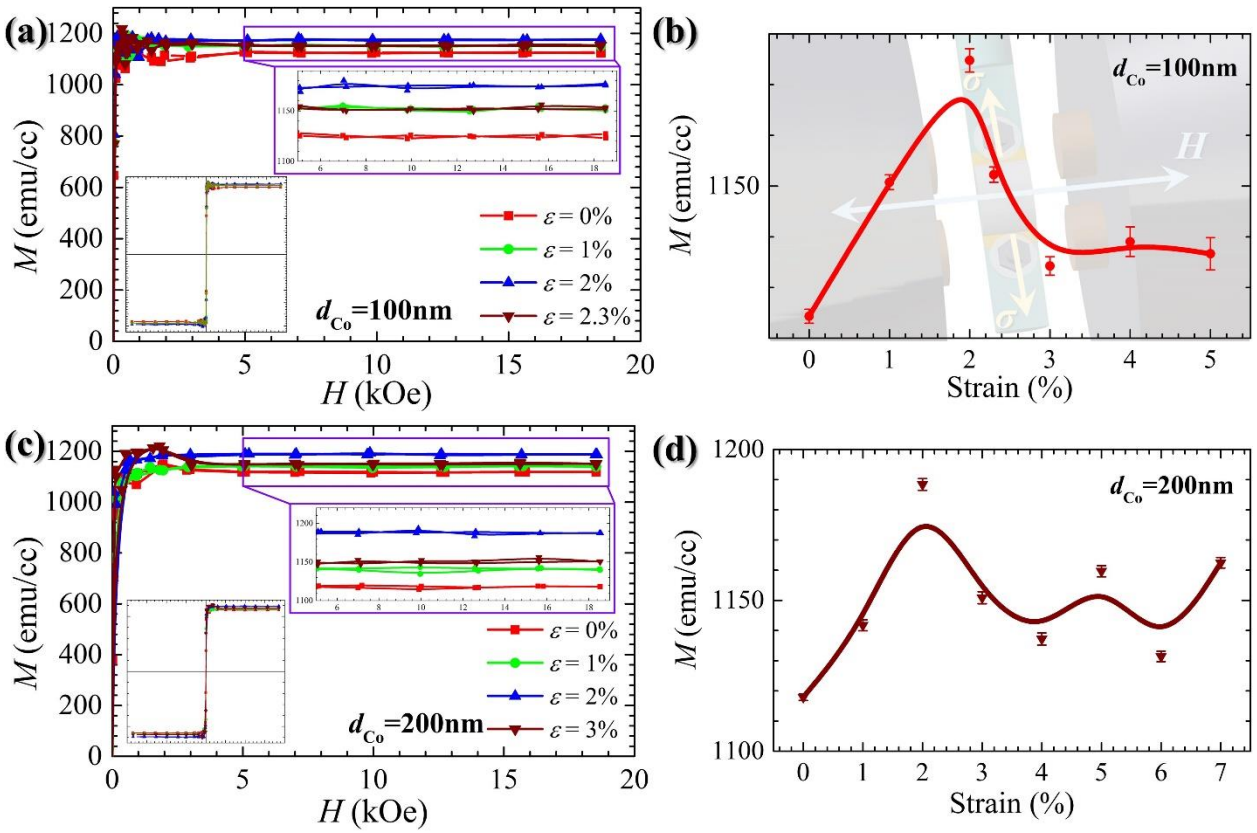

Figure 83. *VSM measurements of the as-sputtered Co films. (a) Hysteresis loop of the Kapton/Co (100 nm) (down-left inset shows the full hysteresis loop and the up-right the magnification of the 5 to 19 kOe region) and (b) the corresponding strain dependence plot of M. Inset shows direction of the applied stress which is perpendicular to the field direction. (c) Hysteresis loop of the Kapton/Co (200 nm) (down-left inset shows the full hysteresis loop and the up-right the magnification of the 5 to 19 kOe region) and (d) strain dependence of M.*

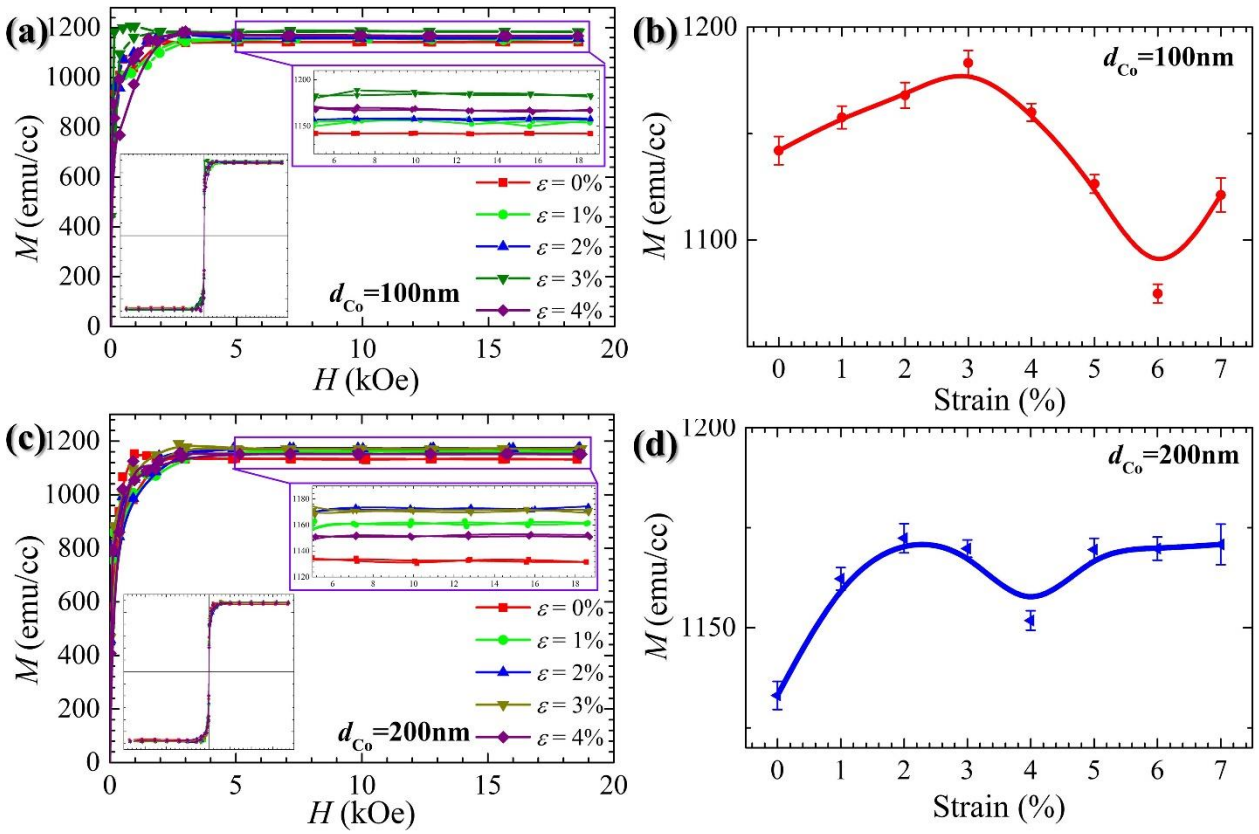

Figure 83. *VSM measurements of the as-sputtered Co films. (a) Hysteresis loop of the Kapton/Ag (12 nm)/Ti (50 nm)/Co (100 nm) (down-left inset shows the full hysteresis loop and the up-right the magnification of the 5 to 19 kOe region) and (b) the corresponding strain dependence plot of M. (c) Hysteresis loop of the Kapton/Ag (12 nm)/Ti (50 nm)/Co (200 nm) (down-left inset shows the full hysteresis loop and the up-right the magnification of the 5 to 19 kOe region) and (d) strain dependence of M.*

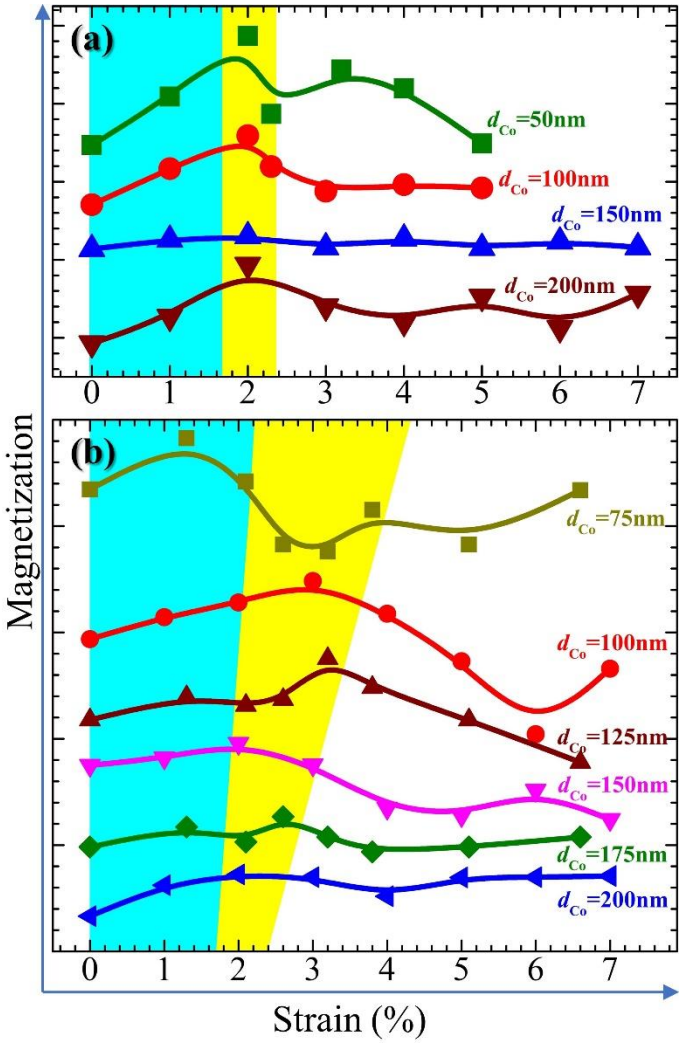

Figure 84. *Strain dependence of M for different Co thicknesses. (a) For the as-sputtered films and (b) for the Kapton/Ag (12 nm)/Ti (50 nm)/Co (d_{Co}) system.*

Micrometer thick Sm-Co films for applications on flexible systems

In the industry 4.0 eco-system, flexible electronic devices bear a huge potential for a broad range of applications due to their diverse properties, such as high stretchability, biocompatibility, portability, light weight, and low costs. In this work, Cobalt-Samarium permanent magnetic thin films on flexible polyimide substrate are studied. The influence of the sputter deposition pressure on the structural, morphological, and magnetic properties is analyzed. A method for growing flexible magnetic films is proposed by achieving a maximum coercivity of 13.86 kOe and an energy product of 16.9 MGOe. These results lay the foundations for the design and fabrication of flexible magnetic devices.

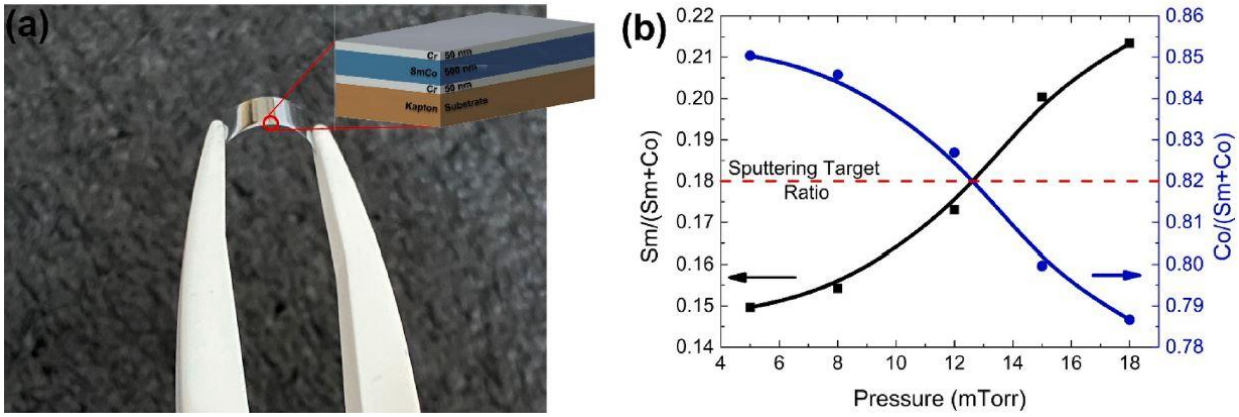

Figure 85. *(a) Image of the flexible magnetic Sm-Co film and a schematic of its cross section. (b) Film composition represented by the ratios Sm/(Sm + Co) and Co/(Sm + Co) plotted against the deposition pressure. Red dashed line marks the stoichiometry of the sputtering target.*

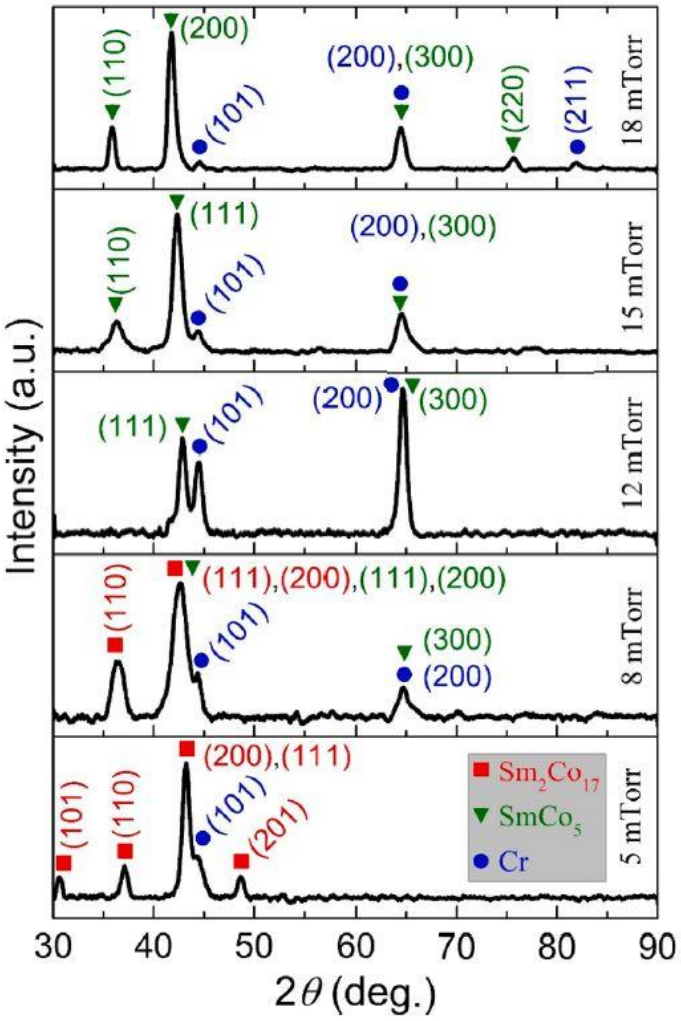

Figure 86. *XRD patterns of the Sm-Co films for the different deposition pressures.*

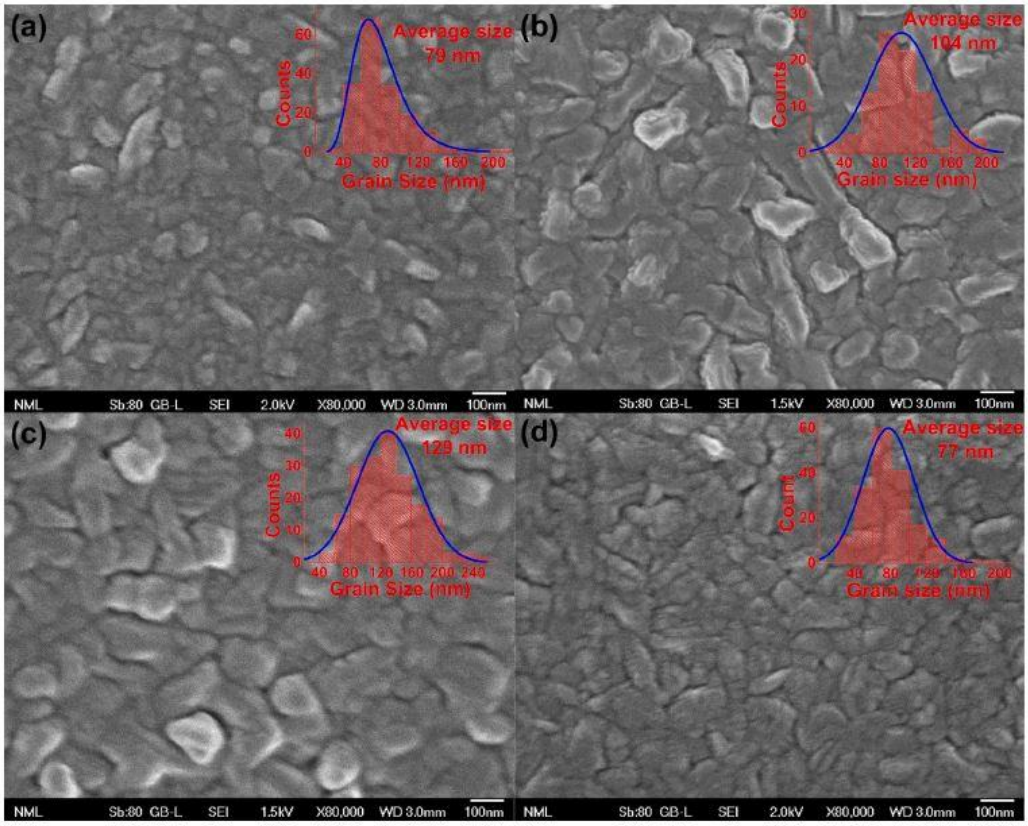

Figure 87. *FESEM micrographs of the surface morphology of the samples deposited at (a) 8, (b) 12, (c) 15 and (d) 18 mTorr, respectively. Insets show the grain size distribution.*

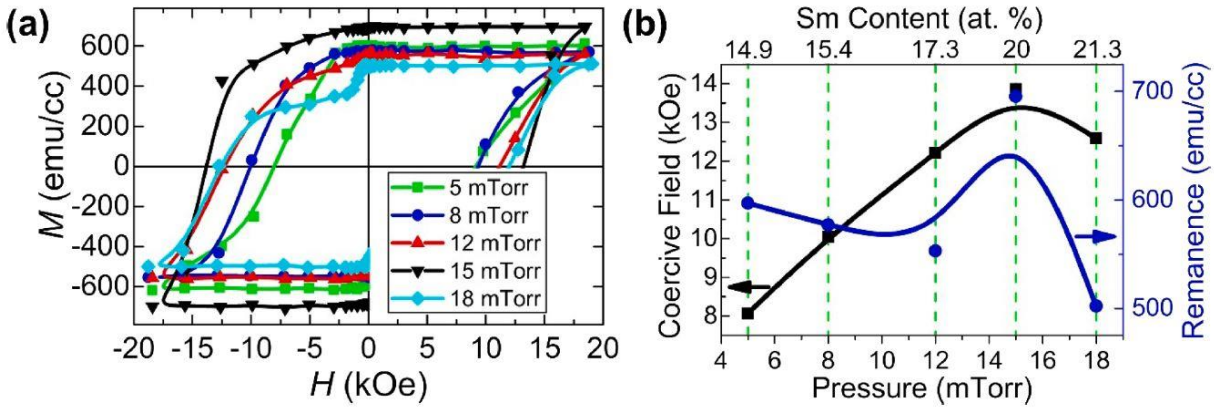

Figure 88. *(a) VSM measurements of the films deposited at various Ar pressures. (b) Coercive field and remanence depending on the deposition pressure in constant external magnetic field of 20 kOe.*

Conclusions

Below are summarized the main findings of the six research items that were listed above.

The experimental results presented above provide a complete characterization for the Bi nanometer-thick films prepared by magnetron sputtering. The structural characterization provided by X-ray diffraction shows that Bi crystallizes in the rhombohedral space group with preferential texture indicating quasi-epitaxial film growth. This is mostly evident for the deposition temperature of 80 ^{o}C. AFM scans along with FESEM observation indicate that the film growth mode is not the same for all deposition temperatures. For temperatures up to 200 ^{o}C, the growth mode is related to Stranski-Krastanov mechanism as proven from the islands forming on top of the film. In contrast, for higher temperatures, *e.g.* 271 ^{o}C, the film growth mode is similar to the Volmer-Weber mechanism with the formation of facets. For higher temperatures, the formation of island-like structures rather than continuous layers is also confirmed by Raman spectra exhibiting a Si peak for deposition temperatures of 200 ^{o}C and above. Of particular interest is the formation of equilibrium crystals at high deposition temperatures, close to the melting point of Bi. The present work presents an extensive examination along with analysis based on their Wulff shape. A close correlation between their nanoscale size and the film thickness was found: For thicker samples and larger grains, small crystals co-exist along with larger crystal structures, so that the grain diameter distribution is described by two distinct lognormal distributions. Furthermore, the magnetotransport properties of films deposited at 80 ^{o}C were studied. The temperature dependence of *MR* is consistent with semiconducting behavior. At low temperatures, evidence for WAL was observed. For 2.5 K fit to the Hikami-Larkin-Nagaoka theory yielded a value of $\alpha = 0.25$ for each coherent channel and $L_{\varphi} = 133.31$ nm. *MR* data at different tilt angles prove that the WAL phenomena at low temperatures and fields are due to surface states rather than bulk states. At higher temperatures, *MR* shows a parabolic behavior. Finally, Hall measurements at high magnetic field show a non-linear Hall resistance caused by the coexistence of electron and hole carriers. Given the above properties of Bi nanoscale films, Bi is a material with diverse capabilities. The examination of its properties may shed light on fundamental aspects of condensed matter physics and also it may pave the way to its use in modern applications such as sensorics.

In the work for Mn-Bi_2Te_3, we perform transport studies in granular magnetically doped, bismuth based topological system prepared with magnetron sputtering. The WAL was investigated by applying the HLN formula to the magnetocundactivity data and the physical parameter l_{φ}, was determined on Mn-Bi_2Te_3 samples. The magnetization in the Mn-doped Bi_2Te_3 thin films is studied here with the AHE. The sign reversal of the AHE is probably caused by the interchange between the considerably different surface and bulk magnetizations. The large magnetoresistance and the AHE, with sign reversal, of that system make it suitable candidate for technological use in many future electronics such as sensors, spintronics, memory devices and neuromorphic electronics.

In the cobalt doped Bi_2Te_3, we study the structural and galvanomagnetic properties in granular magnetically doped, bismuth based topological system prepared with magnetron sputtering. Structural and magnetotransport measurements have been carried out on Bi_2Te_3, Co and Co-doped $(Bi_{1-x}Co_x)_2Te_3$ samples. The pristine samples show metallic properties in

the temperature range from 3 K to 300 K, whereas Co doped samples show a semiconducting trend evident from ρ(T) measurements. The resistivity increases by a factor of two at 3 K and by a factor of one at 300 K in the Co doped sample (x=0.2). Both pristine and doped samples shows positive MR. The WAL was investigated by applying the HLN formula to the magnetoconductivity data and the physical parameter L_φ, was determined for the undoped Bi_2Te_3 sample. The calculated values of L_φ showed a decrease of two orders of magnitude from 3 K to 15 K as a result of the dephasing caused by electron-phonon scattering. With the absence of AHE in cobalt doped sample we conclude that there is no long range ferromagnetic order and the Co atoms behave as paramagnetic centers in the diamagnetic matrix of Bi_2Te_3. The Co atoms in the Bi_2Te_3 matrix act as electrons donors and shift the Fermi energy towards the Dirac Point, reducing the contribution to resistivity from the surface states with the opening of a band gap. At low temperatures the Co doped sample demonstrates an ambipolar transport with a change in the sign of the dominant carriers as the temperature increases.

Motivated by predictions for existence of non-trivial Majorana states in SC-TI-SC trilayers, we grew Bi_2Te_3/Nb and Nb/Bi_2Te_3/Nb sandwich structures, to study the superconducting proximity effect. We have also demonstrated that the proposed heterostructures are compatible with fabrication processes for patterning superconducting junctions. Most of the reported studies on planar SC-TI and SC-TI-SC structures employed flakes of TI exfoliated from bulk crystal that limits the fabrication method and scalability. On the other hand, the sputter deposition offers greater fabrication versatility and large wafer size, compared to MBE. The thin film heterostructures obtained in this work can be suitable platforms for future work and search for Majorana zero-modes through various approaches. Further transport measurement on these structures could provide insight into understanding the physical processes involved at the TI-SC interfaces.

DC magnetron sputtering was utilized for Co films development on flexible Kapton substrates. The Villari effect was studied and particularly the changes on magnetization of Co films when interacting with applied mechanical stress. It is shown that for all thicknesses of the as-sputtered Co films the maximum of magnetization coincides at 2% of the applied strain. On the other hand, the buffer-layered system Kapton/Ag/Ti/Co shows a decreasing strain tolerance (from 3% to 2%) with increasing Co thickness. As-sputtered Co films exhibit a more linear evolution of magnetization in respect to strain application compared to the buffer layered films. The possible mechanism for this non-monotonic behavior is attributed on the change of the interatomic distances which originates from the applied strain. The as-sputtered Kapton/Co system is proposed as a possible flexible system for technological implementation. The exploitation of the consistent linear region up to 2% strains, for Co thicknesses above 100 nm where the hcp structure is clear, can lead in future Villari-based sensors or energy harvesting devices fabrication with optimum efficiency.

Hard magnetic Sm-Co films of 500 nm thickness have been prepared by the DC magnetron sputtering technique at different deposition pressures. The effect of the deposition pressure on the structural, morphological and magnetic characteristics was investigated. It was shown from the combination of EDS and XRD data that by increasing the deposition pressure a transition from the Th_2Zn_{17}- to $CaCu_5$-type phase is achieved. However, at high pressures (18 mTorr) a second soft magnetic phase coexists as is revealed by the hysteresis loops. The maximum values for the coercivity (Hci = 13.86 kOe) and the energy product (16.9 MGOe) were achieved at 15 mTorr, attributed to higher lattice deformation and smaller

coherence length. The present research will conduce to the further development of flexible hard magnetic RE/TM alloys for the exploitation of future stretchable electronic applications.